AD-A243 913

DTIC
ELECTE
JAN 0 6 1992
S
D
D

HIGH-RESOLUTION TVD SCHEMES FOR THE ANALYSIS OF
I. INVISCID SUPERSONIC AND TRANSONIC FLOWS
II. VISCOUS FLOWS WITH SHOCK-INDUCED
SEPARATION AND HEAT TRANSFER

DISSERTATION

Mark Anthony Driver
Captain, USAF

92-00047

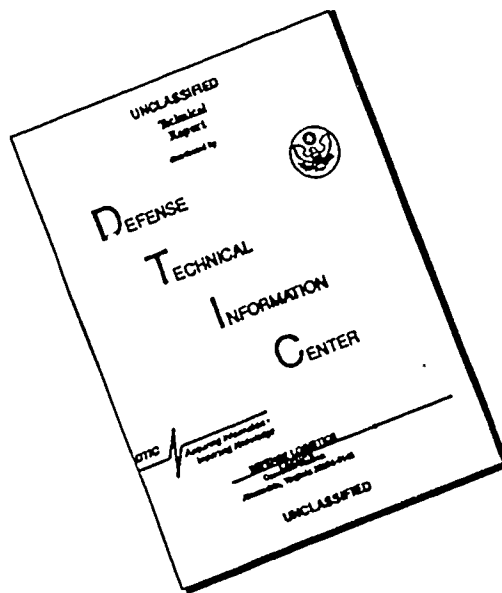92 1 2 056

DISCLAIMER NOTICE

THIS DOCUMENT IS BEST QUALITY AVAILABLE. THE COPY FURNISHED TO DTIC CONTAINED A SIGNIFICANT NUMBER OF PAGES WHICH DO NOT REPRODUCE LEGIBLY.

AFIT/DS/AA/91-2

HIGH-RESOLUTION TVD SCHEMES FOR THE ANALYSIS OF
I. INVISCID SUPERSONIC AND TRANSONIC FLOWS
II. VISCOUS FLOWS WITH SHOCK-INDUCED
SEPARATION AND HEAT TRANSFER

DISSERTATION

Presented to the Faculty of the School of Engineering

of the Air Force Institute of Technology

Air University

In Partial Fulfillment of the

Requirements for the Degree of

Doctor of Philosophy

Mark Anthony Driver. B.A.E.. M.S.

Captain. USAF

December. 1991

Accesion For		
NTIS CRA&I		☑
DTIC TAB		☐
Unannounced		☐
Justification		
By		
Distribution /		
Availability Codes		
Dist	Avail and / or Special	
A-1		

High-Resolution TVD Schemes for the Analysis of

I. Inviscid Supersonic and Transonic Flows

II. Viscous Flows with Shock-Induced

Separation and Heat Transer

Mark A. Driver, B.A.E., M.S.

Captain, USAF

Approved:

$\overline{\hspace{5cm}}$ 23 Nov 1991

$\overline{\hspace{5cm}}$ 22 Nov 1991

$\overline{\hspace{5cm}}$ 22 Nov 1991

$\overline{\hspace{5cm}}$ 22 NOV 1991

$\overline{\hspace{5cm}}$ 25 Nov 1991

$\overline{\hspace{5cm}}$ 25 Nov. 1991

J. S. Przemieniecki

Senior Dean

Acknowledgments

Many people deserve recognition for their contributions to the present effort. I wish to thank my research committee chairman, Dr. Philip Beran. Dr. Beran's guidance was key to the success of the research effort. His advice was, and always will be, appreciated. It was indeed a privilege to be his student. Thanks are due also to the members of my research commitee; Dr. Dennis Quinn, Dr. Milton Franke. Lt Col Gerald Hasen, and Capt John Doty. Comments and suggestions from each of the members greatly improved the quality of the final product. Dr. Quinn's lectures on functional analysis as applied to numerical analysis were particularly helpful. The section on unsteady shock-induced heat transfer especially benefitted from Dr. Franke's sound advice. Lt Col Hasen provided several TVD papers presented at recent conferences; the research outlined in these papers were a significant aid to my effort. A special measure of appreciation is due Capt Doty for serving as the Dean's representative. Capt Doty's comments on the present effort, and suggestions for further research, will be of continuing benefit.

Significant contributions by other AFIT personnel must also be recognized. Dr. William Elrod has been a constant source of advice and information during my time at AFIT, and his discussions of the experimental and theoretical heat transfer results are gratefully acknowledged. The effort would have been immensely more difficult without the assistance of several fellow Ph.D. students: Capt Mark Lutton. Capt Kenneth Moran, and Capt Neal Mosbarger. Mark's expertise with the Beam-Warming scheme proved invaluable. Application of the Beam-Warming scheme would have been tremendously more difficult without Mark's assistance. Ken, a fellow "TVD-aholic". provided suggestions for implementation of the variable damping terms to the TVD algorithms. and was always available for a "what if" or "how

Table of Contents

List of Figures

x

List of Tables

List of Symbols

Symbol

a	- eigenvalue
A	- Jacobian matrix
B	- Jacobian matrix
c	- speed of sound
C	- constant
C_f	- skin friction coefficient
Cx	- axial chord length
CFL	- Courant-Friedrich-Lewy condition
$\bar{D}$	- Roe averaged quantity
e	- total energy
f	- flux
$\bar{f}$	- numerical flux
F	- entropy flux; flux in x direction
$\bar{F}$	- numerical entropy flux
$\hat{F}$	- numerical flux in ξ direction
g	- flux limiter
G	- flux in y direction
$\hat{G}$	- numerical flux in η direction
h	- convective heat transfer coefficient
H	- conservative form; total enthalpy
I	- identity matrix
J	- Jacobian transformation
k	- coefficient of thermal conductivity
k_1	- constant based on metrics
k_2	- constant based on metrics

k_ξ - constant based on metrics

k_η - constant based on metrics

L - operator

$\mathcal{L}$ - Strang fractional step operator

m - x-momentum

msec - millisecond

n - y-momentum

O - order

p - pressure

Pr - Prandtl number

q - dynamic pressure; heat flux

Q - coefficient of numerical viscosity

r - recovery factor

R - eigenvector

Re - Reynolds number

R_{inv} - Riemann invariant

s - entropy

S - matrix of right eigenvectors

t - time

T - temperature

TV - total variation

u - vector of unknows; x-component of velocity

U - entropy function; vector of dependent variables

v - mesh value; y-component of velocity

V - speed; velocity in non-rotating frame of reference

w - characteristic value

W - velocity in rotating frame of reference

x - distance along the reference x-axis; dummy variable

y - distance along the reference y-axis

α - difference of characteristic variables

β - numerical dissipation; relative gas angle

δ - central difference operator; boundary layer thickness

Δ - difference

ϵ - entropy correction parameter

λ - time step divided by mesh spacing; second coefficient of viscosity

Λ - diagonal matrix of eigenvalues

μ - first coefficient of viscosity; CFL (Courant) number

θ - Beam-Warming time discretization parameter

ϕ - initial condition

Φ - artificial dissipation vector

$\dot{\psi}$ - entropy correction; viscous derivative term

Ψ - numerical viscous derivative function

ξ, η - transformed coordinates

γ - ratio of specific heats

ρ - density

τ - shear stress

ω - Beam-Warming damping coefficient

Subscripts

aw - adiabatic wall

cr - condition at a Mach number of unity

e - explicit

i - implicit

int - quantity extrapolated from domain interior

j - ξ index

k - η index

L - left

n - normal; normal derivative

R - right; relative to rotating reference frame

s - shock conditions

t - differentiation w.r.t t: stagnation condition; tangential

u - differentiation w.r.t u

v - viscous; differentiation w.r.t v

w - evaluated at wall

x - differentiation w.r.t x

y - differentiation w.r.t y

η - η direction; differentiation w.r.t η

ξ - ξ direction; differentiation w.r.t ξ

∞ - condition at upstream infinity

1 - condition at stator exit

2 - condition at rotor inlet

3 - condition at rotor exit

Superscripts

h - time step

l - vector component

n - time level

η - η direction

ξ - ξ direction

$\wedge$ - strong conservation form

Abstract

Application of Total Variation Diminishing (TVD) schemes to both inviscid and viscous flows is considered. The mathematical and physical basis of TVD schemes is discussed. First and second-order accurate TVD schemes, and a second-order accurate Lax-Wendroff scheme, are used to compute solutions to the Riemann problem in order to investigate the capability of each to resolve shocks, rarefactions, and contact surfaces. Second-order finite-volume and finite-difference TVD schemes are used to obtain solutions to inviscid supersonic and transonic cascade flow problems. TVD schemes are shown to be superior to the Lax-Wendroff family of schemes for both transient and steady-state computations.

TVD methodology is extended to the solution of viscous flow problems. A first-order time accurate, second-order space accurate algorithm is contrasted against a second-order time and space accurate algorithm for the solution of the viscous Burgers' equation. Necessity of using the fully second-order accurate algorithm at low Reynolds numbers is shown. Solutions are computed to the problems of laminar shock-boundary-layer interaction and unsteady, laminar, shock-induced heat transfer using the new algorithms. These algorithms provide the capability, for the first time, to accurately predict separation, reattachment, and pressure and skin friction profiles for shock-boundary-layer interaction. Additionally, extremely accurate comparison with theory and experiment is evident for the unsteady, shock-induced heat transfer problem. These solutions are contrasted against solutions computed with the Beam-Warming algorithm, and the TVD solutions are shown to be vastly superior.

HIGH-RESOLUTION TVD SCHEMES FOR THE ANALYSIS OF

I. INVISCID SUPERSONIC AND TRANSONIC FLOWS

II. VISCOUS FLOWS WITH SHOCK-INDUCED

SEPARATION AND HEAT TRANSFER

I. Introduction to Part I

1.1 Overview of Part I

Part I begins with a historical look at the development of what has become known as the Total Variation Diminishing (TVD) class of schemes for solving hyperbolic conservation laws. Conditions necessary for a finite-difference scheme to yield physically meaningful solutions are discussed. Development of a second-order accurate TVD scheme for scalar conservation laws is detailed, along with the means of extending it to systems such as the Euler equations of gasdynamics. A brief discussion of the Euler equations is undertaken in the context of applying TVD schemes to their solution. First-order TVD, second-order TVD, and second-order Lax-Wendroff schemes are applied to the Riemann problem to determine the ability of each to resolve the relevant features. Two second-order TVD schemes for solving systems of equations in two space dimensions are covered. These two schemes are then applied to the solution of both supersonic and transonic cas ode flow problems. TVD algorithms are shown to be vastly superior to the Lax-Wendroff fa :'y of algorithms for both transient and steady-state solutions.

1.2 The Genesis of TVD

Total Variation Diminishing (TVD) schemes, originally refered to as Total Variation Nonincreasing (TVNI). first appeared in 1983 with the publication of Harten's *High Resolution Schemes for Hyperbolic Conservation Laws* [22]. In general. TVD schemes are arrived at by applying a first-order accurate numerical method to an

1

appropriately modified flux function thus yielding a method that is second-order accurate except near points of extrema of the solution. The genesis of the TVD class of finite-difference schemes can be traced to 1976 when Harten, Hyman, and Lax authored *On Finite-Difference Approximations and Ent* *Conditions for Shocks* [23]. This work first addressed the question of whethe difference approximations to the solution of hyperbolic conservation laws the physically relevant solution. This is of interest because weak solutions to ch conservation laws are not uniquely determined by initial values, but require an entropy condition be met to converge to the particular physical solution [23].

In the mid 1970's, Harten was also working on his artificial compression method (ACM) [19] to modify standard finite-difference schemes in an effort to prevent the smearing of contact surfaces and improve shock resolution [20, 21]. Prior to this effort Harten states that the standard finite-difference schemes in use typically smeared shocks over 3–5 cells while the width of the contact surface behaved as $n^{1/(R+1)}$ where n is the total number of time steps taken and R is the scheme's order of accuracy. Harten's ACM also addressed the fact that schemes of order greater than one produced overshoots and undershoots around the discontinuity [20] and forced the approximated solution to be nonphysical [23]. Harten's ACM modifications to existing schemes provided the foundation for the new class of TVD schemes presented in his 1983 paper.

The rigorous mathematical foundation of TVD schemes is mainly confined to scalar linear and nonlinear conservation laws and is painstakingly outlined in references [23] and [22]. Computational fluid dynamicists are interested in applying TVD schemes to systems of nonlinear hyperbolic conservation laws, such as the Euler equations of gasdynamics. Therefore, Harten details the application of TVD methodology to 1-D systems using Roe's approximate Riemann solver and provides an example of its extension to 2-D using Strang's dimensional splitting [22]. The original Harten scheme was a second-order accurate explicit method but was extended to a second-order accurate implicit method by Yee and Harten [43].

The high-resolution TVD approach soon gathered favor; explicit and implicit variations were then applied to the Euler equations in general geometries by Yee and Kutler [44] and by Yee and Harten [46]. Later, Wang and Widhopf further extended Harten's TVD methodology to a finite-volume scheme for the Euler equations [48].

TVD algorithms have continued to develop over the past decade. Harten's original scheme was of the upwind variety, meaning that the modifications to the flux function are applied based on the direction of wave propagation, or characteristic direction. Symmetric algorithms have since come into use where the modifications are applied without regard to the characteristic directions. Methods are also available for partial differential equations with source terms and stiff source terms. Yee's 1989 publication, *A Class of High-Resolution Explicit and Implicit Shock-Capturing Methods* [45], provides detailed information on numerous versions of TVD algorithms and examples of their application to numerous problems.

1.3 Hyperbolic Conservation Laws and TVD Methodology

The present section provides a description of the hyperbolic conservation laws for which TVD schemes provide solutions. The requirements for uniqueness of a solution to the initial value problem are given along with the necessary conditions to guarantee convergence of a finite difference approximation to this solution. A summary is provided of the methodology behind the construction of Harten's original second-order accurate TVD scheme.

1.3.1 Finite-Difference Schemes and Oleinik's Entropy Condition. The present analysis is concerned with weak solutions of the initial value problem

$$u_t + f(u)_x = 0$$
$$-\infty < x < \infty \tag{1.1}$$
$$u(x,0) = \phi(x)$$

where $u(x,t)$ is a column vector of m unknowns, $f(u)$ is the flux vector of m components, and $\phi(x)$ is the initial data. Eq 1.1 is hyperbolic if all eigenvalues $a^1(u), \ldots a^m(u)$ of the Jacobian matrix

$$A(u) = f_u \tag{1.2}$$

are real and the set of right eigenvectors $R^1(u), \ldots R^m(u)$ is complete [22] over the domain.

Following Harten [22], consider systems of conservation laws, Eq 1.1, possessing an entropy function $U(u)$ defined such that

$$U_{uu} > 0$$
$$U_u f_u = F_u$$

(1.3)

where F is a function known as the entropy flux [22].

The class of all weak solutions to Eq 1.1 is too large in that the initial value problem is not unique [23]. An additional constraining relation is needed if the scheme is to choose the physically relevant solution. This additional constraint is known as Oleinik's entropy condition and can be expressed as [23]

$$U(u)_t + F(u)_x \leq 0$$

(1.4)

Let us now consider numerical solutions to Eq 1.1 obtained using a $(2k+1)$ point explicit scheme in conservation form [23]. A scheme is in conservation form if it can be expressed as

$$v_j^{n+1} = v_j^n - \lambda \left(\bar{f}_{j+1/2}^n - \bar{f}_{j-1/2}^n \right)$$

(1.5)

where

$$\bar{f}_{j+1/2}^n = \bar{f} \left(v_{j-k+1}^n, \ldots, v_{j+k}^n \right)$$

(1.6)

and $\lambda = \Delta t / \Delta x$. In Eqs 1.5 and 1.6, $\bar{f}$ is the "numerical", or mesh, flux function consistent with $f(u)$ in that $\bar{f}(u, \ldots, u) = f(u)$. The solution u is approximated on the mesh by $v_j^n = v(j\Delta x, n\Delta t)$. The numerical scheme given by Eq 1.5 is consistent with the entropy condition, Eq 1.4, if

$$U_j^{n+1} \leq U_j^n - \lambda \left(F_{j+1/2}^n - F_{j-1/2}^n \right)$$

(1.7)

where $U_j^n = U\left(v_j^n \right)$, $\bar{F}_{j+1/2}^n = \bar{F} \left(v_{j-k+1}^n, \ldots, v_{j+k}^n \right)$, and $\bar{F}$ is the numerical entropy flux consistent with $F(u)$ such that $\bar{F}(u, \ldots, u) = F(u)$

The question of convergence of the finite difference scheme, Eq 1.5, to the appropriate weak solution of Eq 1.1 must now be addressed. The scheme under consid-

eration is nonlinear. so stability of a consistent scheme does not imply convergence. Harten [22] outlines three conditions which. when satisfied. ensure convergence.

(1) The total variation (TV) of the finite difference scheme is uniformly bounded, where

$$TV(v) = \sum_{j=-\infty}^{\infty} |v_{j+1} - v_j| \tag{1.8}$$

(2) The scheme is consistent. as $\Delta x \to 0$. with Oleinik's entropy condition for all entropy functions of Eq 1.1.

(3) Oleinik's entropy condition implies a unique solution of the initial value problem for Eq 1.1.

The reader is referred to the references given by Harten [22] for the arguments that imply convergence given satisfaction of the above criteria. For the present work, the validity of these criteria will be assumed and the effort concentrated on demonstrating the development of a scheme that satisfies criteria (1) and (2) when given the third criterion.

1.3.2 Development of Harten's Second-Order Scalar TVD Scheme. Harten's second-order accurate TVD scheme is the product of a nonoscillatory. first-order accurate scheme applied to an appropriately modified flux function [22]. This section describes the properties of the first-order scheme and outlines the procedure used by Harten to arrive at the appropriate modified flux.

Consider the initial value problem for a scalar conservation law:

$$u_t + f(u)_x \equiv u_t + a(u)u_x = 0$$
$$a(u) = f_u \qquad\qquad -\infty < x < \infty \tag{1.9}$$
$$u(x.0) = o(x)$$

where $o(x)$ is of bounded total variation. Rigorous analysis is restricted to the scalar case because TVD schemes are not defined for systems of of non-linear conservation

laws where the spatial total variation of the solution may increase due to wave interaction [22].

A weak solution of Eq 1.9 has a monotonicity property [22], as a function of time. defined as:

(1) No new local extrema in x may be created.

(2) A local minimum is nondecreasing and a local maximum

is nonincreasing.

The monotonicity property implies that the total variation in x is nonincreasing in time, $TV(u(t_2)) \leq TV(u(t_1))$.

An explicit. $(2k+1)$, point finite-difference scheme in conservation form. as given by Eq 1.5 and applied to Eq 1.9. can be written as

$$
\begin{aligned}
v_j^{n+1} &= H\left(v_{j-k}^n, \ldots, v_{j+k}^n\right) \\
&= v_j^n - \lambda\left[\bar{f}\left(v_{j-k+1}^n, \ldots, v_{j+k}^n\right) - \bar{f}\left(v_{j-k}^n, \ldots, v_{j+k-1}^n\right)\right]
\end{aligned}
\tag{1.10}
$$

or in operator notation as

$$
v^{n+1} = L \cdot v^n
\tag{1.11}
$$

The scheme given by Eq 1.10 is TVD if. for all v of bounded total variation

$$
TV(L \cdot v) \leq TV(v)
\tag{1.12}
$$

where the total variation is defined by Eq 1.8. Eq 1.11 represents a monotonicity preserving scheme if the operator L is monotonicity preserving. That is. if v is a monotonic mesh function so is $L \cdot v$. The scheme is monotone if H is a monotonic nondecreasing function of each of its $2k+1$ arguments [23]:

$$
H_{w_i}(w_{-k}, \ldots, w_k) \geq 0
\tag{1.13}
$$

for all i such that $-k \leq i \leq k$.

An example of a scheme that is not monotone is the second-order accurate Lax-Wendroff scheme with

$$\bar{f}_{j+\frac{1}{2}} = \frac{1}{2}\left[f\left(v_j^n\right) + f\left(v_{j+1}^n\right) - a^2\lambda\Delta_{j+\frac{1}{2}}v^n \right] \tag{1.14}$$

where $\Delta_{j+\frac{1}{2}}v = v_{j+1} - v_j$. Therefore the discrete equation is

$$
\begin{aligned}
v_j^{n+1} &= v_j^n - \frac{1}{2}\lambda\left[f\left(v_{j+1}^n\right) - f\left(v_{j-1}^n\right) - a^2\lambda\left(v_{j+1}^n - 2v_j^n + v_{j-1}^n\right) \right] \\
&= H\left(v_{j-1}^n, v_j^n, v_{j+1}^n\right)
\end{aligned}
\tag{1.15}
$$

Taking the derivative of H with respect to the argument v_{j+1}^n yields

$$H_{v_{j+1}} = \frac{1}{2}\left(\nu^2 - \nu\right) \tag{1.16}$$

where $\nu = a\lambda$. Only the case $0 < \nu < 1$ need be examined since the Law-Wendroff scheme is unstable for $\nu > 1$, and Lax-Wendroff provides the exact solution for $\nu = 1$. Clearly, the Lax-Wendroff scheme is not monotone for any $\nu < 1$. Additionally, the numerical results of reference [23] show that the Lax-Wendroff scheme is not monotonicity preserving.

The first-order accurate Roe scheme provides an example of monotone behavior. The numerical flux for the Roe scheme is

$$\bar{f}_{j+\frac{1}{2}} = \frac{1}{2}\left[f\left(v_j^n\right) + f\left(v_{j+1}^n\right) - |a|\Delta_{j+\frac{1}{2}}v^n \right] \tag{1.17}$$

giving the discrete equation

$$
\begin{aligned}
v_j^{n+1} &= v_j^n - \frac{1}{2}\lambda\left[f\left(v_{j+1}^n\right) - f\left(v_{j-1}^n\right) - |a|\left(v_{j+1}^n - 2v_j^n + v_{j-1}^n\right) \right] \\
&= H\left(v_{j-1}^n, v_j^n, v_{j+1}^n\right)
\end{aligned}
\tag{1.18}
$$

Taking derivatives of H with respect to each of its arguments gives

$$H_{v_{j-1}} = \nu$$
$$H_{v_j} = 1 - \nu \qquad (1.19)$$
$$H_{v_{j+1}} = 0$$

Thus, H is a monotonic, non-decreasing function of each of its arguments showing that the Roe scheme is indeed monotonic.

Let S_M, S_{TVD}, and S_{MP} denote monotone, TVD, and monotonicity preserving schemes respectively. Theorem 2.1 of reference [22] provides the hierarchy of these properties:

$$S_M \subset S_{TVD} \subset S_{MP} \qquad (1.20)$$

Thus, the Roe scheme is also TVD and monotonicity preserving.

A scheme in the conservation form of Eq 1.10 that is monotone with v_j^n converging boundedly almost everywhere to some function $u(x,t)$ has two further desirable properties. The theorem of Lax and Wendroff as given by reference [23] states that if the scheme is in conservation form with $v(x,t)$ converging almost everwhere to $u(x,t)$, then $u(x,t)$ is a weak solution of Eq 1.9. The theorem of Harten, Hyman, and Lax [23] states that if the scheme is monotone in addition to meeting the criteria of the Lax-Wendroff theorem, then Oleinik's entropy condition is satisfied for all discontinuities of u. Thus a monotone scheme satisfies the convergence criteria for a unique solution of the initial value problem as stated in the Section 1.3.1.

Attention is now focused on how the properties of a monotone scheme are helpful in constructing Harten's second order TVD scheme. Harten states that monotone schemes provide second-order accurate solutions to the modified Eq [22]

$$u_t + f(u)_x = \lambda^{-1} [\beta(u,\lambda)u_x]_x \qquad (1.21)$$

$$\beta(u,\lambda) = \frac{1}{2\lambda^2} \left[\sum_{l=-k}^{k} l^2 H_l(u,\ldots,u) - \lambda^2 a^2(u) \right] \qquad (1.22)$$

$$\beta(u,\lambda) \geq 0$$

$$\beta(u,\lambda) \neq 0$$

8

where β is a numerical dissipation term. Since $\beta(u, \lambda) \neq 0$, monotone schemes are only first-order accurate approximations to the initial value problem of Eq 1.9.

Suppose the scheme given by Eq 1.10 is a monotone scheme and thus provides a second-order accurate numerical approximation to the modified equation, Eq 1.21, rewritten as

$$u_t + (f - (1/\lambda)g)_x = 0 \qquad (1.23)$$

where $g = \Delta x \beta(u, \lambda)u_x$. Applying this scheme to the following equation

$$u_t + (f + (1/\lambda)g)_x = 0 \qquad (1.24)$$

yields a second-order accurate approximation to its modified equation. Since $g = O[\Delta x]$ the modified equation satisfies [22]

$$u_t + f_x = O\left[(\Delta x)^2\right] \qquad (1.25)$$

Thus, application of a first-order scheme to a scalar conservation law with an appropriately modified flux function yields a second-order accurate approximation to the original equation $u_t + f_x = 0$. Note that in order to apply the scheme to the modified flux function, g must be a differentiable function of u. Harten achieves this by smoothing the point values of g [22]. This smoothing enlarges the support of the scheme such that his first-order scheme, using a three-point stencil, becomes a second-order scheme using a five-point stencil. The reader is referred to reference [22] for the details of how the three-point, first-order scheme is constructed so as to ensure its TVD property.

Let us now turn our attention to the specific scalar scheme developed by Harten. Consider a three-point, finite-difference scheme in conservation form with the following numerical flux function

$$\bar{f}(v_j, v_{j+1}) = \frac{1}{2}\left[f(v_j) + f(v_{j+1}) - (1/\lambda)Q\left(\lambda\bar{a}_{j+1/2}\right)\Delta_{j+1/2}v\right] \qquad (1.26)$$

9

where $\Delta_{j+1/2}v = v_{j+1} - v_j$ and

$$
\begin{aligned}
\bar{a} &= [f(v_{j+1}) - f(v_j)]/\Delta_{j+1/2}v \quad (\Delta_{j+1/2}v \neq 0) \\
&= a(v_j) \quad (\Delta_{j+1/2}v = 0)
\end{aligned}
\tag{1.27}
$$

Q is a function known as the coefficient of numerical viscosity. Numerical viscosity is the mechanism that allows a discontinuity to be captured as part of the numerical solution [20]. This is in contrast to shock fitting, where the discontinuity is considered as an internal boundary.

Lemma 3.1 of reference [22] states that the above scheme is TVD under the Courant-Friedrichs-Lewy (CFL) condition

$$
\lambda \max_j \left| \bar{a}^n_{j+1/2} \right| \leq \mu
\tag{1.28}
$$

given

$$
|x| \leq Q(x) \leq 1
\tag{1.29}
$$

for $0 \leq |x| \leq \mu \leq 1$.

The first-order accurate three-point scheme given by Eq 1.26 is converted to a second-order accurate scheme by applying the three-point scheme to modified flux values f_j^M [22]:

$$
\begin{aligned}
f_j^M &= f(v_j) + (1/\lambda)g_j & g_j &= g(v_{j-1}, v_j, v_{j+1}) \\
\bar{v}^M_{j+1/2} &= \bar{v}_{j+1/2} + \gamma_{j+1/2} & \gamma_{j+1/2} &= (g_{j+1} - g_j)/\Delta_{j+1/2}v
\end{aligned}
\tag{1.30}
$$

where $\bar{v} \equiv \lambda\bar{a}$. The modified numerical flux is

$$
\begin{aligned}
\bar{f}^M_{j+1/2} &= \tfrac{1}{2}\left[f_j^M + f_{j+1}^M - (1/\lambda)Q\left(\bar{v}^M_{j+1/2}\right)\Delta_{j+1/2}v \right] \\
&= \tfrac{1}{2}\left[f(v_j) + f(v_{j+1}) \right] \\
&\quad + (1/(2\lambda))\left[g_j + g_{j+1} - Q\left(\bar{v}_{j+1/2} + \gamma_{j+1/2}\right)\Delta_{j+1/2}v \right]
\end{aligned}
\tag{1.31}
$$

Lemma 3.2 of reference [22] provides that Eq 1.31 represents the numerical flux of a second-order scheme so long as $Q(x)$ is Lipschitz continuous and g_j satisfies

$$
\begin{aligned}
g_j + g_{j+1} &= \left[Q\left(\bar{\nu}_{j+1/2}\right) - \left(\bar{\nu}_{j+1/2}\right)^2 \right] \Delta_{j+1/2} v + O\left[2\right] \\
\gamma_{j+1/2}\Delta_{j+1/2}v &\equiv g_{j+1} - g_j = O\left(\Delta^2\right)
\end{aligned}
\tag{1.32}
$$

Harten [22] constructs g in the following manner so as to satisfy Eq 1.32:

$$
\begin{aligned}
g_j &= s_{j+1/2} \max\left[0, \min\left(\left|\tilde{g}_{j+1/2}\right|, \tilde{g}_{j-1/2} \cdot s_{j+1/2}\right)\right] \\[2mm]
&= s_{j+1/2} \min\left(\left|\tilde{g}_{j+1/2}\right|, \left|\tilde{g}_{j-1/2}\right|\right) \qquad\qquad \left(\tilde{g}_{j+1/2} \cdot \tilde{g}_{j-1/2} \geq 0\right) \\
&= 0 \qquad\qquad\qquad\qquad\qquad\qquad\qquad\quad \left(\tilde{g}_{j+1/2} \cdot \tilde{g}_{j-1/2} \leq 0\right)
\end{aligned}
\tag{1.33}
$$

where

$$
\begin{aligned}
\tilde{g}_{j+1/2} &= \tfrac{1}{2}\left[Q\left(\bar{\nu}_{j+1/2}\right) - \left(\bar{\nu}_{j+1/2}\right)^2 \right] \Delta_{j+1/2}v \\
s_{j+1/2} &= sgn\left(\tilde{g}_{j+1/2}\right)
\end{aligned}
\tag{1.34}
$$

Finally, Lemma 3.4 of reference [22] provides that a conservative finite difference scheme, with the numerical flux given by Eq 1.26, is TVD under the restriction of Eq 1.28 so long as $Q(x)$ satisfies Eq 1.29. Thus a second-order accurate (except near points of extrema where $s_{j+1/2}$ is discontinous), five-point scheme has been constructed for the solution of Eq 1.9. The scheme provides high resolution capturing of discontinuities and converges to a physically relevant solution.

1.3.3 Extension to Systems of Conservation Laws. We now concern ourselves with extending the scalar scheme developed in Section 1.3.2 to systems of conservation laws. Currently, TVD schemes are only defined for scalar hyperbolic conservation laws or constant coefficient hyperbolic systems. This is due to the fact that the spatial total variation of the solution to a system of nonlinear conservation laws is not necessarily a monotonically decreasing function of time [46]. Wave interactions may cause the total variation to increase. Harten extends the technique using a generalized version of Roe's approximate Riemann solver [22]. The idea is to apply the scheme in a scalar fashion to each of the systems linearized characteristic variables.

11

After Harten [22], let

$$S(u) = \left(R^1(u), \ldots, R^m(u) \right) \tag{1.35}$$

be a matrix whose columns are the right eigenvectors of the Jacobian matrix $A(u)$ in Eq 1.1. It follows that

$$S^{-1}AS = \Lambda \tag{1.36}$$

where Λ is the diagonal matrix of eigenvalues such that $\Lambda_{ij} = a^i(u)\delta_{ij}$. Therefore

$$S^{-1}u_t + S^{-1}A(u)SS^{-1}u_x = 0 \tag{1.37}$$

or

$$S^{-1}u_t + \Lambda S^{-1}u_x = 0 \tag{1.38}$$

where the characteristic variables w are defined such that

$$w = S^{-1}u \tag{1.39}$$

Eq 1.38 becomes

$$w_t + \Lambda w_x = 0 \tag{1.40}$$

which can be decoupled into m scalar characteristic equations with $1 \leq k \leq m$

$$w_t^k + a^k w_x^k = 0 \tag{1.41}$$

The most beneficial use of the characteristic variables comes to light by recognizing that they can be viewed as the components of u in the coordinate system $\{R^k\}$ such that [22]

$$u = \sum_{k=1}^{m} w^k R^k \tag{1.42}$$

Harten uses this fact to extend his scalar scheme to general nonlinear systems of hyperbolic conservation laws.

Let $\alpha_{j+1/2}^k$ be the component of $\Delta_{j+1/2}v = v_{j+1} - v_j$ in the $\{R^k\}$ coordinate system such that

$$\Delta_{j+1/2}v = \sum_{k=1}^{m} \alpha_{j+1/2}^k R_{j+1/2}^k \tag{1.43}$$

The scheme given by Eqs 1.30–1.34 is extended to general systems as

$$v_j^{n+1} = v_j^n - \lambda \left(\bar{f}_{j+1/2}^n - \bar{f}_{j-1/2}^n \right) \tag{1.44}$$

$$\bar{f}_{j+1/2} = \tfrac{1}{2}\left[f\left(v_j\right) + f\left(v_{j+1}\right)\right]$$
$$+\tfrac{1}{2\lambda}\sum_{k=1}^{m} R_{j+1/2}^k \left[g_j^k + g_{j+1}^k - Q^k\left(\bar{\nu}_{j+1/2}^k + \gamma_{j+1/2}^k\right)\alpha_{j+1/2}^k\right] \tag{1.45}$$

where $\nu_{j+1/2}^k = \lambda a_{j+1/2}^k$ and

$$g_j^k = s_{j+1/2}^k \max\left[0, \min\left(\left|\check{g}_{j+1/2}^k\right| \cdot \check{g}_{j-1/2}^k \cdot s_{j+1/2}^k\right)\right] \tag{1.46}$$

with

$$\check{g}_{j+1/2}^k = \tfrac{1}{2}\left[Q^k\left(\bar{\nu}_{j+1/2}^k\right) - \left(\bar{\nu}_{j+1/2}^k\right)^2\right]\alpha_{j+1/2}^k$$
$$s_{j+1/2}^k = sgn\left(\check{g}_{j+1/2}^k\right)$$
$$\gamma_{j+1/2}^k = \left(g_{j+1}^k - g_j^k\right)/\alpha_{j+1/2}^k \qquad \left(\alpha_{j+1/2}^k \neq 0\right)$$
$$= 0 \qquad \left(\alpha_{j+1/2}^k = 0\right) \tag{1.47}$$

1.3.4 Entropy Enforcement. As a final comment on the initial development of Harten's second-order TVD scheme, we turn now to the question of physically relevant solutions for systems of equations. As mentioned in the previous section, the total variation may not be a monotonic decreasing function of time due to wave interactions. In addition, Oleinik's entropy inequality ensures physically relevant, or admissable, solutions only in the limit as $\Delta t \to 0$. In reality we are concerned with obtaining admissable solutions on a relatively coarse mesh.

In order to arrive at a proper criterion. Harten examines the Riemann initial value problem [22] for Eq 1.1:

$$u(x,0) = \phi(x) = u_L \quad x < 0$$
$$= u_R \quad x > 0 \tag{1.48}$$

with u_L and u_R satisfying the Rankine-Hugoniot relations with wave speed s. If $u(x,t) = \varphi(x - st)$ is to satisfy Oleinik's inequality the numerical scheme must yield a steady progressing profile with a narrow transition from u_L to u_R [20, 22]. Harten refers to this property as *resolution*.

If the solution $u(x,t) = \phi(x - st)$ is inadmissable. then the solution is a fan of waves [22]. This fan of waves is a function of x/t and consists of a rarefaction, or expansion, wave in the same field as the initial discontinuity. The physical solution requires the initial discontinuity break up instantaeously, since $u(x,t) = \varphi(x/t)$.The term *entropy enforcement* refers to the requirement that the numerical scheme break up the initial discontinuity at a *fast* rate, thus imitating the physical behavior [22].

The systems of conservation laws under consideration contain two types of characteristic fields, termed nonlinear and linearly degenerate by Harten [22]. The nonlinear fields are defined such that $a_u^k R^k \neq 0$, while the linearly degenerate fields are defined by $a_u^k R^k \equiv 0$. The waves of a nonlinear field are shock waves or expansion waves while the waves of a linearly degenerate field are solely contact. or entropy. discontinuities.

To address the question of entropy enforcement. consider the scheme given by Eq 1.26. which has the effective numerical viscosity coefficient

$$\beta(u,\lambda) = \frac{1}{2}\left[Q(\nu) - \nu^2\right] \tag{1.49}$$

The least dissipative form of Q is arrived at by choosing it to be consistent with Eq 1.29 such that

$$Q(x) = |x| \tag{1.50}$$

With Q given by Eq 1.50, the scheme of Eq 1.26 can be rewritten as [22]

$$v_j^{n+1} = v_j^n - \left(\bar{\nu}_{j+1/2}\right)^- \Delta_{j+1/2}v^n - \left(\bar{\nu}_{j-1/2}\right)^+ \Delta_{j-1/2}v^n \tag{1.51}$$

14

where

$$\nu^- = \min(\nu, 0) = \tfrac{1}{2}(\nu - |\nu|) \qquad \nu^+ = \max(\nu, 0) = \tfrac{1}{2}(\nu + |\nu|) \tag{1.52}$$

Harten points out that the scheme of Eqs 1.51 and 1.52 is a generalization of the Courant, Isaacson, and Rees scheme, which has been thoroughly analyzed in the literature. The interested reader is referred to reference [22] for further details.

If the scheme given by Eqs 1.51 and 1.52 is applied to the Riemann problem with the Rankine-Hugoniot relation satisfied by letting the speed of propagation be zero, Eq 1.51 holds the initial discontinuity steady regardless of entropy considerations. In other words, the initial discontinuity is not broken up and there is no entropy enforcement in this case.

The problem is that the numerical viscosity vanishes for $\nu = 0$. Harten eliminates this problem by modifying $Q(x) = |x|$ near $x = 0$ to be positive. The modification is as follows [22] for $0 < \epsilon \le \tfrac{1}{2}$

$$\begin{aligned} Q(x) &= (x^2/(4\epsilon)) + \epsilon & |x| < 2\epsilon \\ &= |x| & |x| \ge 2\epsilon \end{aligned} \tag{1.53}$$

with the entropy correction parameter, ϵ, typically of order 0.1.

Harten summarizes the results of numerical experiments carried out with the scheme of Eqs 1.14 and 1.15 applied to the Euler equations for the Riemann problem. These experiments used $\epsilon = 0.05$, 0.1, and 0.25 for all fields, and also $\epsilon = 0$ for the linearly degenerate field. Basically, highly resolved shocks were obtained for all values of ϵ under consideration. The contact surface was better resolved than with the first-order accurate scheme of Eqs 1.51 and 1.52, but still remained rather smeared.

To prevent excessive smearing in the linearly degenerate field containing the contact surface, Harten replaces Eq 1.46 in the linearly degenerate field with [22]

$$g_j = \bar{g}_j + \theta_j \bar{\bar{g}}_j \tag{1.54}$$

where $\bar{g}_j$ is the right hand side of g_j given by Eq 1.46 and, $\bar{\bar{g}}_j$ is

$$\bar{\bar{g}}_j = S \max \left[0, \min \left(S \sigma_{j-1/2} \alpha_{j-1/2}, \sigma_{j+1/2} \left| \alpha_{j+1/2} \right| \right) \right] \tag{1.55}$$

15

with

$$S = sgn\left(\alpha_{j+1/2}\right) \tag{1.56}$$

$$\sigma_{j+1/2} = \sigma_{j+1/2}\left(\nu_{j+1/2}\right) = \frac{1}{2}\left[1 - Q\left(\nu_{j+1/2}\right)\right] \tag{1.57}$$

$$\theta_j = \left|\alpha_{j+1/2} - \alpha_{j-1/2}\right| / \left(\left|\alpha_{j+1/2}\right| + \left|\alpha_{j-1/2}\right|\right) \tag{1.58}$$

II. Inviscid Analysis

2.1 Euler Equations

The Euler equations are statements of the conservation laws for mass, momentum, and energy assuming an inviscid, nonconducting gas. When the Euler equations are arranged such that ρ, ρu, ρv, and e are the dependent variables the conservative or divergence form is obtained. Lax showed that the conservative form of the Euler equations satisfies the weak solution of the Rankine-Hugoniot relations and thus correctly predicts the jump conditions across the shock discontinuity [1, 35]. In fact, use of the conservative form is necessary for the discontinuity to represent a physical wave when shock capturing schemes are applied [1]. The conservative form is often referred to as the divergence form because the equations identify the divergence of physical quantities. The governing equations may be writ.. in the following vector form:

$$\frac{\partial U}{\partial t} + \frac{\partial F(U)}{\partial x} + \frac{\partial G(U)}{\partial y} = 0 \tag{2.1}$$

where U contains the dependent variables which are the density, ρ; x-momentum, ρu; y-momentum, ρv; and total energy per unit volume, e. F contains the flux terms differentiated with respect to x, and G contains the flux terms differentiated with respect to y. The elements of U, F, and G are:

$$U = \begin{bmatrix} \rho \\ m \\ n \\ e \end{bmatrix} \quad F = \begin{bmatrix} m \\ m^2/\rho + p \\ mv \\ (e+p)m/\rho \end{bmatrix} \quad G = \begin{bmatrix} n \\ nu \\ n^2/\rho + p \\ (e+p)n/\rho \end{bmatrix} \tag{2.2}$$

where $m = \rho u$ and $n = \rho v$. The pressure, p, is given as

$$p = (\gamma - 1)\left[e - \frac{(m^2 + n^2)}{2\rho}\right] \tag{2.3}$$

for a thermally and calorically perfect gas.

A general spatial transformation of the form $\xi = \xi(x, y)$ and $\eta = \eta(x, y)$ is used to transform Eq 2.1 from the physical domain (x, y) to the computational domain

(ξ, η). The strong conservation law form of the Euler equations is now given by [45]

$$\frac{\partial \hat{U}}{\partial t} + \frac{\partial \hat{F}(\hat{U})}{\partial \xi} + \frac{\partial \hat{G}(\hat{U})}{\partial \eta} = 0 \tag{2.4}$$

$$\hat{U} = U/J \tag{2.5}$$

$$\hat{F} = (\xi_x F + \xi_y G)/J \tag{2.6}$$

$$\hat{G} = (\eta_x F + \eta_y G)/J \tag{2.7}$$

$$J = \xi_x \eta_y - \xi_y \eta_x \tag{2.8}$$

where J is the Jacobian of the transformation.

Since the TVD method used herein utilizes the local-characteristic approach. which is a generalization of Roe's approximate Riemann solver[36], the Jacobians $\hat{A}$ and $\hat{B}$ of $\hat{F}$ and $\hat{G}$ are required and can be written as

$$\hat{A} = (\xi_x A + \xi_y B) \tag{2.9}$$

$$\hat{B} = (\eta_x A + \eta_y B) \tag{2.10}$$

where

$$A = F_U = \begin{bmatrix} 0 & 1 & 0 & 0 \\ \frac{1}{2}(\gamma-1)(u^2+v^2) - u^2 & (3-\gamma)u & (1-\gamma)v & \gamma-1 \\ -uv & v & u & 0 \\ \left[\frac{1}{2}(\gamma-1)(u^2+v^2) - H\right]u & H-(\gamma-1)u^2 & (1-\gamma)uv & \gamma u \end{bmatrix}$$

$$B = G_U = \begin{bmatrix} 0 & 0 & 1 & 0 \\ -uv & v & u & 0 \\ \frac{1}{2}(\gamma-1)(u^2+v^2) - v^2 & (1-\gamma)u & (3-\gamma)v & \gamma-1 \\ \left[(\frac{1}{2}\gamma-1)(u^2+v^2) - H\right]v & (1-\gamma)uv & H-(\gamma-1)v^2 & \gamma v \end{bmatrix}$$

with the total enthalpy, H, given by

$$H = \frac{\gamma p}{(\gamma - 1)\rho} + \frac{1}{2}\left(u^2 + v^2\right)$$
(2.11)

The eigenvalues of $\hat{A}$, denoted $\left(a_\xi^1, a_\xi^2, a_\xi^3, a_\xi^4\right)$, are

$$a_\xi = \begin{pmatrix} \xi_x u + \xi_y v - k_\xi c \\ \xi_x u + \xi_y v \\ \xi_x u + \xi_y v + k_\xi c \\ \xi_x u + \xi_y v \end{pmatrix}$$
(2.12)

where

$$k_\xi = \sqrt{\xi_x^2 + \xi_y^2}$$
(2.13)

The right eigenvectors of $\hat{A}$, $\left(R_\xi^1, R_\xi^2, R_\xi^3, R_\xi^4\right)$, are

$$R_\xi^1 = \begin{bmatrix} 1 \\ u - k_1 c \\ v - k_2 c \\ H - k_1 u c - k_2 v c \end{bmatrix} \quad R_\xi^2 = \begin{bmatrix} 1 \\ u \\ v \\ \frac{1}{2}(u^2 + v^2) \end{bmatrix}$$

(2.14)

$$R_\xi^3 = \begin{bmatrix} 1 \\ u + k_1 c \\ v + k_2 c \\ H + k_1 u c + k_2 v c \end{bmatrix} \quad R_\xi^4 = \begin{bmatrix} 0 \\ -k_2 \\ k_1 \\ k_1 v - k_2 u \end{bmatrix}$$

where

$$k_1 = \left[\frac{\xi_x}{J} \bigg/ \sqrt{\left(\frac{\xi_x}{J}\right)^2 + \left(\frac{\xi_y}{J}\right)^2} \right]$$
(2.15)

19

and

$$k_2 = \left[\frac{\xi_y}{J} \bigg/ \sqrt{\left(\frac{\xi_x}{J}\right)^2 + \left(\frac{\xi_y}{J}\right)^2} \right] \qquad (2.16)$$

The eigenvalues and eigenvectors of $\hat{B}$ are obtained by replacing ξ in Eqs 2.12 through 2.16 with η:

$$a_\eta = \begin{pmatrix} \eta_x u + \eta_y v - k_\eta c \\ \eta_x u + \eta_y v \\ \eta_x u + \eta_y v + k_\eta c \\ \eta_x u + \eta_y v \end{pmatrix} \qquad (2.17)$$

$$k_\eta = \sqrt{\eta_x^2 + \eta_y^2} \qquad (2.18)$$

$$R_\eta^1 = \begin{bmatrix} 1.0 \\ u - k_1 c \\ v - k_2 c \\ H - k_1 uc - k_2 vc \end{bmatrix} \qquad R_\eta^2 = \begin{bmatrix} 1.0 \\ u \\ v \\ \frac{1}{2}(u^2 + v^2) \end{bmatrix}$$

$$(2.19)$$

$$R_\eta^3 = \begin{bmatrix} 1.0 \\ u + k_1 c \\ v + k_2 c \\ H + k_1 uc + k_2 vc \end{bmatrix} \qquad R_\eta^4 = \begin{bmatrix} 0.0 \\ -k_2 \\ k_1 \\ k_1 v - k_2 u \end{bmatrix}$$

$$k_1 = \left[\frac{\eta_x}{J} \bigg/ \sqrt{\left(\frac{\eta_x}{J}\right)^2 + \left(\frac{\eta_y}{J}\right)^2} \right] \qquad (2.20)$$

$$k_2 = \left[\frac{\eta_y}{J} \bigg/ \sqrt{\left(\frac{\eta_x}{J}\right)^2 + \left(\frac{\eta_y}{J}\right)^2} \right] \qquad (2.21)$$

2.2 Numerical Procedure

2.2.1 1-D Roe, Lax-Wendroff, and TVD Algorithms.

The 1-D schemes under consideration are the first order accurate Godunov-type [22] scheme of Roe, referred to as the ROE scheme; the second-order accurate Lax-Wendroff-type scheme, referred

Table 2.1. Dissipation Terms for ROE. LW and ULTIC Schemes

Scheme	Description	Dissipation (β)
ROE	1st Order TVD	$\beta^k_{j+1/2} = \left\|\nu^k_{j+1/2}\right\| \alpha^k_{j+1/2}$
LW	2nd Order non-TVD	$\beta^k_{j+1/2} = \left(\nu^k_{j+1/2}\right)^2 \alpha^k_{j+1/2}$
ULTIC	2nd Order TVD	$\beta^k_{j+1/2} = Q^k\left(\nu^k_{j+1/2} + \gamma^k_{j+1/2}\right)\alpha^k_{j+1/2} - \left(g^k_j + g^k_{j-1}\right)$ with Eqs 1.54 through 1.58 applied to the linearly degenerate field

to as the LW scheme: and the second-order accurate TVD scheme of Harten, referred to as ULTIC. All three schemes can be written in the form

$$v^{n+1}_j = v^n_j - \lambda\left(\bar{f}_{j+1/2} - \bar{f}_{j-1/2}\right)$$

$$\bar{f}_{j+1/2} = \tfrac{1}{2}\left[f(v_j) + f(v_{j+1}) - \tfrac{1}{\lambda}\sum_{k=1}^m \beta^k_{j+1/2}R^k_{j+1/2}\right] \tag{2.22}$$

with the appropriate dissipation term. β. from Table 2.1.

2.2.2 2-D Harten-Yee Finite-Volume Algorithm. An upwind TVD scheme in finite-volume form [45] is used in the present study. The grid spacing is denoted by $\Delta\xi$ and $\Delta\eta$. such that $\xi = j\Delta\xi$ and $\eta = k\Delta\eta$. Utilizing the Strang-type fractional step method allows the scheme to be implemented in a local-characteristic approach and ensures second-order accuracy:

$$\hat{U}^{n+2}_{j,k} = \mathcal{L}^{h/2}_\xi \mathcal{L}^h_\eta \mathcal{L}^h_\xi \mathcal{L}^h_\eta \mathcal{L}^{h/2}_\xi \hat{U}^n_{j,k} \tag{2.23}$$

where

$$\mathcal{L}^h_\xi \hat{U}^n_{j,k} = \hat{U}^*_{j,k} = \hat{U}^n_{j,k} - \frac{\Delta t}{\Delta\xi}\left(\hat{F}^n_{j+\frac{1}{2},k} - \hat{F}^n_{j-\frac{1}{2},k}\right) \tag{2.24}$$

$$\mathcal{L}_\eta^h \hat{U}_{j,k} = \hat{U}_{j,k} - \frac{\Delta t}{\Delta \eta} \left(\tilde{G}_{j,k+\frac{1}{2}} - \tilde{G}_{j,k-\frac{1}{2}} \right) \tag{2.25}$$

with $h = \Delta t$. Application of the entire sequence of operators (one iteration) advances the solution two time levels. The functions $\tilde{F}_{j+\frac{1}{2},k}$ and $\tilde{G}_{j,k+\frac{1}{2}}$ are the numerical fluxes in the ξ and η directions evaluated at cell interfaces. For instance. $\tilde{F}_{j+\frac{1}{2},k}$ in Yee's finite-volume formulation is expressed as

$$\tilde{F}_{j+\frac{1}{2},k} = \frac{1}{2} \left[\left(\frac{\xi_x}{J} \right)_{j+\frac{1}{2}} (F_{j,k} + F_{j+1,k}) + \left(\frac{\xi_y}{J} \right)_{j+\frac{1}{2}} (G_{j,k} + G_{j+1,k}) \right.$$
$$\left. + \frac{\Delta \xi}{\Delta t} R_{\xi_{j+\frac{1}{2}}} \Phi_{j+\frac{1}{2}} / J_{j+\frac{1}{2}} \right] \tag{2.26}$$

where the subscript $j + \frac{1}{2}$ is a simplified notation for $j + \frac{1}{2}, k$. The numerical flux function in the η direction is defined similarly:

$$\tilde{G}_{j,k+\frac{1}{2}} = \frac{1}{2} \left[\left(\frac{\eta_x}{J} \right)_{k+\frac{1}{2}} (F_{j,k} + F_{j,k+1}) + \left(\frac{\eta_y}{J} \right)_{k+\frac{1}{2}} (G_{j,k} + G_{j,k+1}) \right.$$
$$\left. + \frac{\Delta \eta}{\Delta t} R_{\eta_{k+\frac{1}{2}}} \Phi_{k+\frac{1}{2}} / J_{k+\frac{1}{2}} \right] \tag{2.27}$$

The eigenvalues and eigenvectors are evaluated at cell interfaces using symmetric averages of $U_{j,k}$ and $U_{j+1,k}$. $U_{j,k}$ and $U_{j,k+1}$. respectively. Roe's averaging technique for a perfect gas is used herein and takes the form [36]

$$u_{j+\frac{1}{2},k} = \frac{\bar{D} u_{j+1,k} + u_{j,k}}{\bar{D} + 1} \tag{2.28}$$

$$v_{j+\frac{1}{2},k} = \frac{\bar{D} v_{j+1,k} + v_{j,k}}{\bar{D} + 1} \tag{2.29}$$

$$H_{j+\frac{1}{2},k} = \frac{\bar{D} H_{j+1,k} + H_{j,k}}{\bar{D} + 1} \tag{2.30}$$

$$c_{j+\frac{1}{2},k}^2 = (\gamma - 1) \left[H_{j+\frac{1}{2},k} - \frac{1}{2} \left(u_{j+\frac{1}{2},k}^2 + v_{j+\frac{1}{2},k}^2 \right) \right] \tag{2.31}$$

where

$$\bar{D} = \sqrt{\rho_{j+1,k} / \rho_{j,k}} \tag{2.32}$$

Roe's averaging technique is used because it has the computational advantage of perfectly resolving stationary [46], but not necessarily moving. discontinuities.

The quantities $\left(\frac{\xi_x}{J}\right)_{j+\frac{1}{2}}$ and $1/J_{j+\frac{1}{2}}$ are defined as follows for the finite-volume formulation

$$\left(\frac{\xi_x}{J}\right)_{j+\frac{1}{2}} = \frac{1}{2}\left[\left(\frac{\xi_x}{J}\right)_{j,k} + \left(\frac{\xi_x}{J}\right)_{j+1,k}\right] \qquad (2.33)$$

$$\frac{1}{J_{j+\frac{1}{2}}} = \frac{1}{2}\left(\frac{1}{J_{j+1,k}} + \frac{1}{J_{j,k}}\right) \qquad (2.34)$$

The constants $(k_1)_{j+\frac{1}{2}}$ and $(k_2)_{j+\frac{1}{2}}$ necessary in determining $R_{\xi_{j+\frac{1}{2}}}$, Eq 2.15, are defined as

$$(k_1)_{j+\frac{1}{2}} = \frac{\left(\frac{\xi_x}{J}\right)_{j+\frac{1}{2}}}{\sqrt{\left(\frac{\xi_x}{J}\right)^2_{j+\frac{1}{2}} + \left(\frac{\xi_y}{J}\right)^2_{j+\frac{1}{2}}}} \qquad (2.35)$$

and

$$(k_2)_{j+\frac{1}{2}} = \frac{\left(\frac{\xi_y}{J}\right)_{j+\frac{1}{2}}}{\sqrt{\left(\frac{\xi_x}{J}\right)^2_{j+\frac{1}{2}} + \left(\frac{\xi_y}{J}\right)^2_{j+\frac{1}{2}}}} \qquad (2.36)$$

The vector function $\Phi_{j+\frac{1}{2}}$ is composed of elements denoted as $\left(\phi^l_{j+\frac{1}{2}}\right)^U$ for a second-order upwind TVD scheme. The elements are given by

$$\phi^l_{j+\frac{1}{2}} = \sigma\left(\nu^l_{j+\frac{1}{2}}\right)\left(g^l_{j+1} + g^l_j\right) - Q\left(\nu^l_{j+\frac{1}{2}} + \gamma^l_{j+\frac{1}{2}}\right)\alpha^l_{j+\frac{1}{2}} \qquad (2.37)$$

where. with $\lambda = \Delta t / \Delta \xi$

$$\nu^l_{j+\frac{1}{2}} = \lambda a^l_{j+\frac{1}{2}} \qquad (2.38)$$

$\alpha_{j+\frac{1}{2}}$ is the difference of the characteristic variables in the ξ direction.

$$\alpha_{j+\frac{1}{2}} = R^{-1}_{j+\frac{1}{2}}\left(U_{j+1,k} - U_{j,k}\right) \qquad (2.39)$$

or

$$\begin{bmatrix} \alpha^1_{j+\frac{1}{2}} \\ \alpha^2_{j+\frac{1}{2}} \\ \alpha^3_{j+\frac{1}{2}} \\ \alpha^4_{j+\frac{1}{2}} \end{bmatrix} = \begin{bmatrix} (aa - bb)/2 \\ \Delta_{j+\frac{1}{2}}\rho - aa \\ (aa + bb)/2 \\ cc \end{bmatrix} \qquad (2.40)$$

23

where

$$aa = \frac{\gamma - 1}{c_{j+\frac{1}{2}}^2} \left[\Delta_{j+\frac{1}{2}}e + \frac{u_{j+\frac{1}{2}}^2 + v_{j+\frac{1}{2}}^2}{2} \Delta_{j+\frac{1}{2}}\rho - u_{j+\frac{1}{2}}\Delta_{j+\frac{1}{2}}m - v_{j+\frac{1}{2}}\Delta_{j+\frac{1}{2}}n \right] \quad (2.41)$$

$$bb = \frac{1}{c_{j+\frac{1}{2}}} \left[k_1 \Delta_{j+\frac{1}{2}}m - \left(k_1 u_{j+\frac{1}{2}} + k_2 v_{j+\frac{1}{2}} \right) \Delta_{j+\frac{1}{2}}\rho + k_2 \Delta_{j+\frac{1}{2}}n \right] \quad (2.42)$$

$$cc = k_1 \Delta_{j+\frac{1}{2}}n + \left(k_2 u_{j+\frac{1}{2}} - k_1 v_{j+\frac{1}{2}} \right) \Delta_{j+\frac{1}{2}}\rho - k_2 \Delta_{j+\frac{1}{2}}m \quad (2.43)$$

$$\Delta_{j+\frac{1}{2}}z = z_{j+1,k} - z_{j,k} \quad (2.44)$$

The difference of the local characteristic variables in the η direction is obtained in similar fashion:

$$\alpha_{k+\frac{1}{2}} = R_{k+\frac{1}{2}}^{-1} \left(U_{j,k+1} - U_{j,k} \right) \quad (2.45)$$

$$\begin{bmatrix} \alpha_{k+\frac{1}{2}}^1 \\ \alpha_{k+\frac{1}{2}}^2 \\ \alpha_{k+\frac{1}{2}}^3 \\ \alpha_{k+\frac{1}{2}}^4 \end{bmatrix} = \begin{bmatrix} (dd - ee)/2 \\ \Delta_{k+\frac{1}{2}}\rho - aa \\ (dd + ee)/2 \\ ff \end{bmatrix} \quad (2.46)$$

where

$$dd = \frac{\gamma - 1}{c_{k+\frac{1}{2}}^2} \left[\Delta_{k+\frac{1}{2}}e + \frac{u_{k+\frac{1}{2}}^2 + v_{k+\frac{1}{2}}^2}{2} \Delta_{k+\frac{1}{2}}\rho - u_{k+\frac{1}{2}}\Delta_{k+\frac{1}{2}}m - v_{k+\frac{1}{2}}\Delta_{k+\frac{1}{2}}n \right] \quad (2.47)$$

$$ee = \frac{1}{c_{k+\frac{1}{2}}} \left[k_1 \Delta_{k+\frac{1}{2}}m - \left(k_1 u_{k+\frac{1}{2}} + k_2 v_{k+\frac{1}{2}} \right) \Delta_{k+\frac{1}{2}}\rho + k_2 \Delta_{k+\frac{1}{2}}n \right] \quad (2.48)$$

$$ff = k_1 \Delta_{k+\frac{1}{2}}n + \left(k_2 u_{k+\frac{1}{2}} - k_1 v_{k+\frac{1}{2}} \right) \Delta_{k+\frac{1}{2}}\rho - k_2 \Delta_{k+\frac{1}{2}}m \quad (2.49)$$

with

$$(k_1)_{k+\frac{1}{2}} = \frac{\left(\frac{\eta_x}{J} \right)_{k+\frac{1}{2}}}{\sqrt{\left(\frac{\eta_x}{J} \right)_{k+\frac{1}{2}}^2 + \left(\frac{\eta_y}{J} \right)_{k+\frac{1}{2}}^2}} \quad (2.50)$$

$$(k_2)_{k+\frac{1}{2}} = \frac{\left(\frac{\eta_y}{J}\right)_{k+\frac{1}{2}}}{\sqrt{\left(\frac{\eta_x}{J}\right)^2_{k+\frac{1}{2}} + \left(\frac{\eta_y}{J}\right)^2_{k+\frac{1}{2}}}} \qquad (2.51)$$

$$\Delta_{k+\frac{1}{2}}z = z_{j,k+1} - z_{j,k} \qquad (2.52)$$

The function $\gamma^l_{j+\frac{1}{2}}$ is given by

$$\gamma^l_{j+\frac{1}{2}} = \begin{cases} \sigma\left(\lambda a^l_{j+\frac{1}{2}}\right)\frac{(g^l_{j+1}-g^l_j)}{a^l_{j+\frac{1}{2}}} & \left(a^l_{j+\frac{1}{2}} \neq 0\right) \\ 0 & \left(a^l_{j+\frac{1}{2}} = 0\right) \end{cases} \qquad (2.53)$$

where

$$\sigma(x) = \frac{1}{2}\left[Q(x) - x^2\right] \qquad (2.54)$$

and

$$Q(x) = \begin{cases} |x| & (|x| \geq 2\epsilon) \\ (x^2/(4\epsilon)) + \epsilon & (|x| < 2\epsilon) \end{cases} \qquad (2.55)$$

The entropy correction parameter, ϵ, is generally fixed during computations, but can vary between 0 and 0.5.

The function g^l_j in Eq 2.37, initially referred to in Section 1.3.2, is termed the 'limiter' function and can be expressed in a variety of ways [45]. The present study bases the choice of the limiter on the type of characteristic field under consideration. For the nonlinear fields, $a^l R^l \neq 0$, Eq 4.34d of Yee [45] is used:

$$g^l_j = \left(a^l_{j+\frac{1}{2}}a^l_{j-\frac{1}{2}} + \left|a^l_{j+\frac{1}{2}}a^l_{j-\frac{1}{2}}\right|\right)/\left(a^l_{j+\frac{1}{2}} + a^l_{j-\frac{1}{2}}\right) \qquad (2.56)$$

For the linearly degenerate fields. $a^l R^l \equiv 0$. Eq 4.34g of Yee [45] is applied:

$$g^l_j = S \cdot \max\left[0, \min\left(2\left|a^l_{j+\frac{1}{2}}\right|, S \cdot a^l_{j-\frac{1}{2}}\right) \cdot \min\left(\left|a^l_{j+\frac{1}{2}}\right|, 2S \cdot a^l_{j-\frac{1}{2}}\right)\right] \qquad (2.57)$$

where

$$S = sgn\left(a^l_{j+\frac{1}{2}}\right) \qquad (2.58)$$

The nonlinear fields correspond to $l = 1$ and $l = 3$ while the linearly degenerate fields correspond to $l = 2$ and $l = 4$. It should again be noted that the waves of a

nonlinear field are either shocks or rarefaction waves while the waves of a linearly degenerate field are uniquely contact discontinuities [22]. Since this is a five-point scheme, the values of g_j^l are needed at cell centers just outside the computational domain. Zeroth-order extrapolation is used to obtain the necessary values, following the example of Harten [22].

2.2.3 2-D Harten-Yee Chain-Rule Algorithm.

In addition to the finite-volume formulation of Yee, a finite-difference form based on the chain-rule conservation form of the governing equations was utilized [40]:

$$\frac{\partial U}{\partial t} + \xi_x \frac{\partial F(U)}{\partial \xi} + \xi_y \frac{\partial G(U)}{\partial \xi} + \eta_x \frac{\partial F(U)}{\partial \eta} + \eta_y \frac{\partial G(U)}{\partial \eta} = 0 \qquad (2.59)$$

Previous researchers report that the governing equations in this form are more computationally efficient than the strong conservation form used in the finite-volume approach [40]. This was found not to be the case for the current TVD algorithms, with both formulations performing approximately the same in terms of computational efficiency.

The local characteristic approach given by Eq 2.23 is now applied to U instead of $\hat{U}$:

$$U_{j,k}^{n+2} = \mathcal{L}_\xi^{h/2} \mathcal{L}_\eta^h \mathcal{L}_\xi^h \mathcal{L}_\eta^h \mathcal{L}_\xi^{h/2} U_{j,k}^n \qquad (2.60)$$

where

$$\mathcal{L}_\xi^h U_{j,k}^n = U_{j,k}^* = U_{j,k}^n - \frac{\Delta t}{\Delta \xi} \left(\tilde{F}_{j+\frac{1}{2},k}^n - \tilde{F}_{j-\frac{1}{2},k}^n \right) \qquad (2.61)$$

$$\mathcal{L}_\eta^h U_{j,k}^* = U_{j,k}^{**} - \frac{\Delta t}{\Delta \eta} \left(\tilde{G}_{j,k+\frac{1}{2}}^* - \tilde{G}_{j,k-\frac{1}{2}}^* \right) \qquad (2.62)$$

The numerical fluxes, $\tilde{F}_{j+\frac{1}{2},k}$ and $\tilde{G}_{j,k+\frac{1}{2}}$, for the chain rule conservation form are

$$\tilde{F}_{j+\frac{1}{2},k} = \frac{1}{2} \left[(\xi_x)_{j,k} \left(F_{j,k} + F_{j+1,k} \right) + (\xi_y)_{j,k} \left(G_{j,k} + G_{j+1,k} \right) + \frac{\Delta \xi}{\Delta t} R_{\xi_{j+\frac{1}{2}}} \Phi_{j+\frac{1}{2}} \right] \qquad (2.63)$$

and

$$\hat{G}_{j,k+\frac{1}{2}} = \frac{1}{2}\left[(\eta_x)_{j,k}\left(F_{j,k} + F_{j,k+1}\right) + (\eta_y)_{j,k}\left(G_{j,k} + G_{j,k+1}\right) + \frac{\Delta\eta}{\Delta t}R_{\eta_{k+\frac{1}{2}}}\Phi_{k+\frac{1}{2}}\right] \quad (2.64)$$

The quantities $(\xi_x)_{j+\frac{1}{2}}$, $(k_1)_{j+\frac{1}{2}}$, and $(k_2)_{j+\frac{1}{2}}$ are defined as follows for the chain rule formulation:

$$(\xi_x)_{j+\frac{1}{2}} = \frac{1}{2}\left[(\xi_x)_{j,k} + (\xi_x)_{j+1,k}\right] \quad (2.65)$$

$$(k_1)_{j+\frac{1}{2}} = \frac{(\xi_x)_{j+\frac{1}{2}}}{\sqrt{(\xi_x)_{j+\frac{1}{2}}^2 + (\xi_y)_{j+\frac{1}{2}}^2}} \quad (2.66)$$

$$(k_2)_{j+\frac{1}{2}} = \frac{(\xi_y)_{j+\frac{1}{2}}}{\sqrt{(\xi_x)_{j+\frac{1}{2}}^2 + (\xi_y)_{j+\frac{1}{2}}^2}} \quad (2.67)$$

III. Inviscid Results and Conclusions

Chapter III details application of the Harten-Yee TVD algorithms to three different classes of problems. Riemann's problem of gas dynamics is covered first. A shock wave, rarefaction wave, and contact surface are present to test the capability of the TVD algorithm to resolve the features of both linear and linearly degenerate fields. Both Harten-Yee algorithms degenerate to Harten's ULTIC scheme for this case since there are no metric variations. In addition to the ULTIC scheme, solutions from the Roe and Lax-Wendroff schemes are presented to provide the reader with a performance comparison.

Steady-state flow through a supersonic cascade of wedges is then examined using the Harten-Yee finite-volume scheme. Both shock and expansion waves are present in this test case. Finally, flow through a typical transonic turbine rotor is considered. This test case is used to demonstrate the capability of both the finite-volume and chain-rule algorithms to deal with transient start-up phenomena in route to a steady-state solution. Boundary and initial conditions utilized for these solutions are discussed at length to provide an appreciation of how they complement the physical nature of the TVD schemes.

3.1 Riemann's Problem

Solution of Riemann's problem [9] provides a means for evaluating the ability of a scheme to resolve the waves present in both nonlinear and linearly degenerate fields. The Roe (ROE), Lax-Wendroff (LW), and ULTIC schemes are applied to Riemann's problem in order to compare their performance. Solutions are compared with those of Harten, who utilized the same schemes [22], as a check for correct implementation of the algorithms.

Riemann's problem is now solved for:

$$U(x.0) = \begin{cases} U_L & x < 0 \\ U_R & x > 0 \end{cases} \tag{3.1}$$

where

$$U_L = \begin{bmatrix} 0.445 \\ 0.311 \\ 0.8928 \end{bmatrix} \quad U_R = \begin{bmatrix} 0.5 \\ 0 \\ 1.4275 \end{bmatrix} \tag{3.2}$$

These conditions establish a leftward moving rarefaction wave, rightward moving contact surface. and rightward moving shock wave. Figures 3.1-3.9 show the results obtained when the ROE, LW, and ULT1C schemes are applied to this problem. It should again be noted that ULT1C is the degenerate form of the Harten-Yee scheme for the 1-D problem with no metric variations. The circles are the computed values while the solid line delineates the exact solution. The calculations are consistent with those of Harten [22] in that they were carried out to 100 time steps with a CFL restriction of 0.95 using 140 cells. In addition. a value of $\epsilon = 0$ was used for the TVD schemes with Roe averaging used only in the ULT1C scheme. For the one-dimensional case. Roe averaging seems to be of benefit only when accurate resolution of the contact surface is desired, and then changes the result only slightly by bringing the density at the leading edge of the contact surface to its correct value one grid point sooner. Values of ϵ between 0 and 0.25 seem to produce almost identical results except that $\epsilon = 0$ seems to enhance the resolution of the contact surface in the ULT1C solution. This is consistent with Harten's observations. Overall. the results of this investigation seem to be almost identical with those of Harten.

Figures 3.1-3.3 show that the first-order ROE scheme provides a fair resolution of the shock. but does rather poorly in resolving both the rarefaction wave and the contact discontinuity. Note, however. that the ROE scheme is TVD and that its monotonicity preserving property prevents oscillation of the solution at the
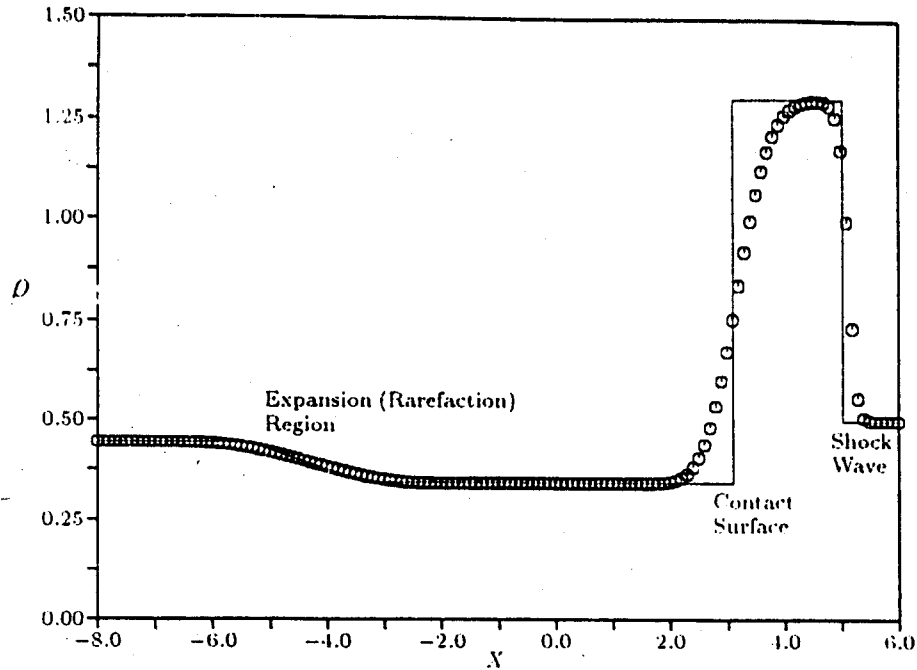
Figure 3.1. Density from ROE Scheme Applied to Riemann's Problem

discontinuities.

Figures 3.4-3.6 show that the performance of the non-TVD LW scheme leaves much to be desired. Not only does the non-monotonicity of the scheme cause severe oscillations at the contact and shock discontinuities, but oscillations are also occurring at the trailing edge of the rarefaction wave. Harten, Hyman, and Lax [23] point out that Lax-Wendroff schemes can produce non-physical solutions, even when attempts are made to construct a physically correct entropy function.

Figures 3.7-3.9 clearly display the improvements of the second-order ULTIC scheme over the first-order ROE scheme. The resolution of the shock, rarefaction waves and contact surface is quite good. It should again be noted that a value of $\epsilon = 0$ and the use of Roe averaging are important for resolving the contact surface as accurately as possible.

Figures 3.10-3.12 show the results obtained when ULTIC is applied to a different set of data for Riemann's problem, the solid line again representing the exact

THIS

PAGE

IS

MISSING

IN

ORIGINAL

DOCUMENT
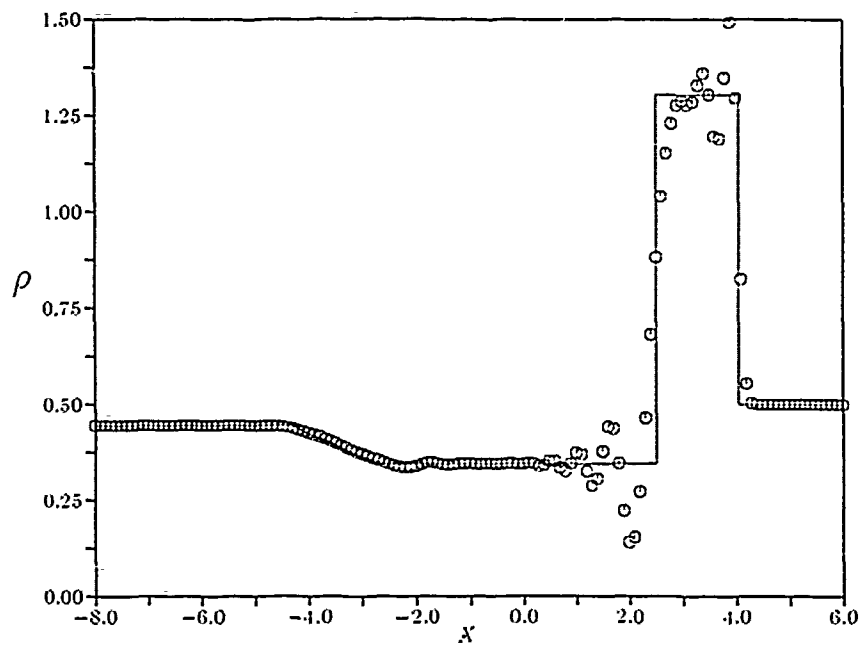
Figure 3.4. Density from LW Scheme Applied to Riemann's Problem
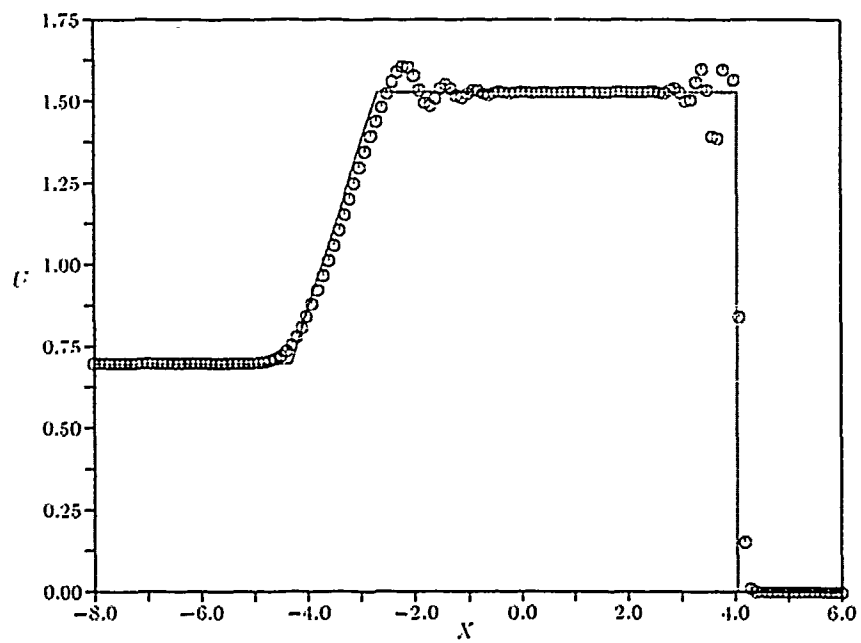
Figure 3.5. Velocity from LW Scheme Applied to Riemann's Problem

32
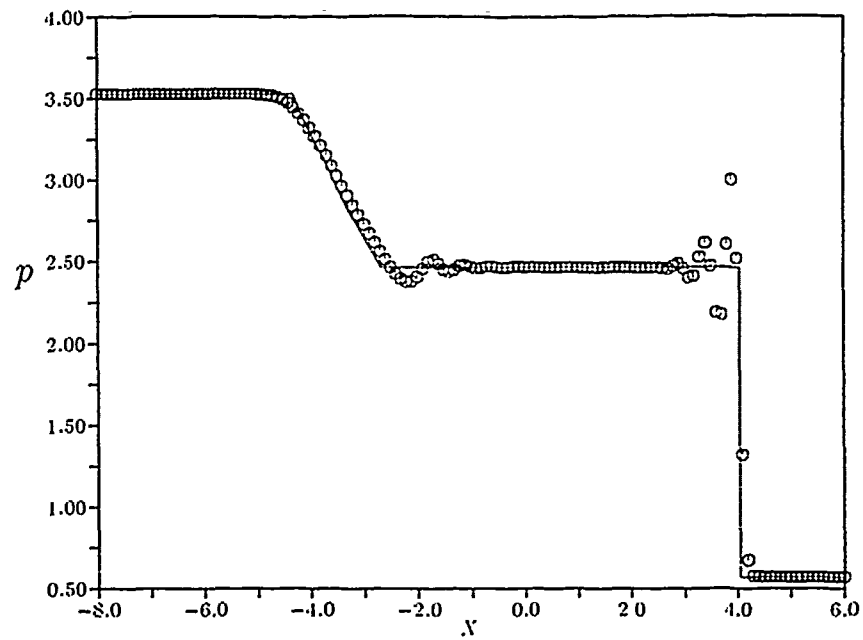
Figure 3.6. Pressure from LW Scheme Applied to Riemann's Problem
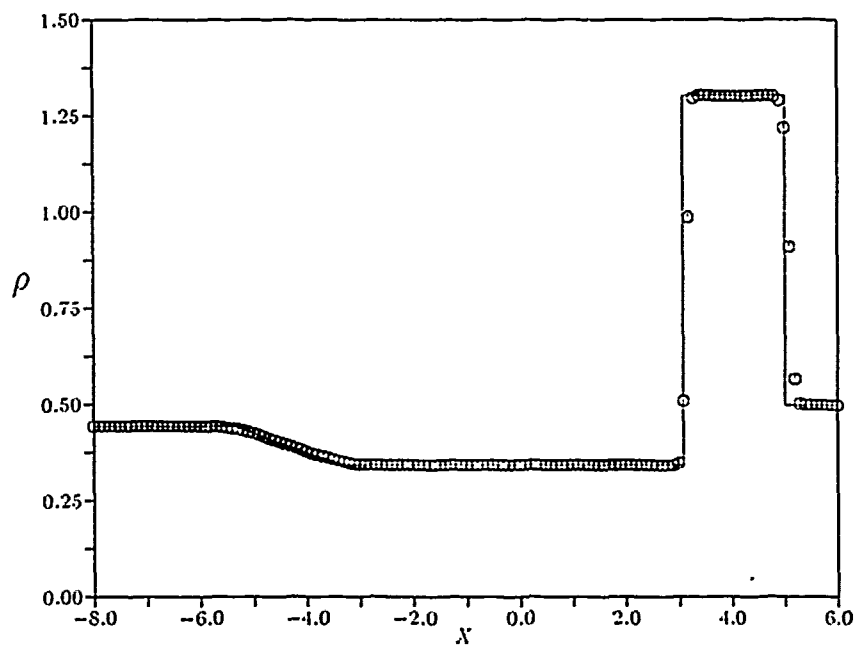
Figure 3.7. Density from ULTIC Scheme Applied to Riemann's Problem

33
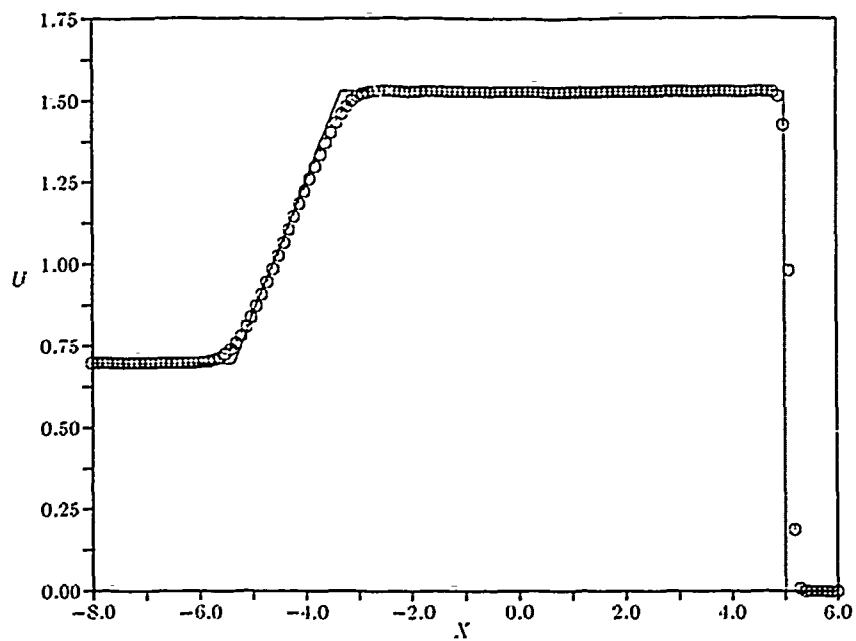
Figure 3.8. Velocity from ULT1C Scheme Applied to Riemann's Problem
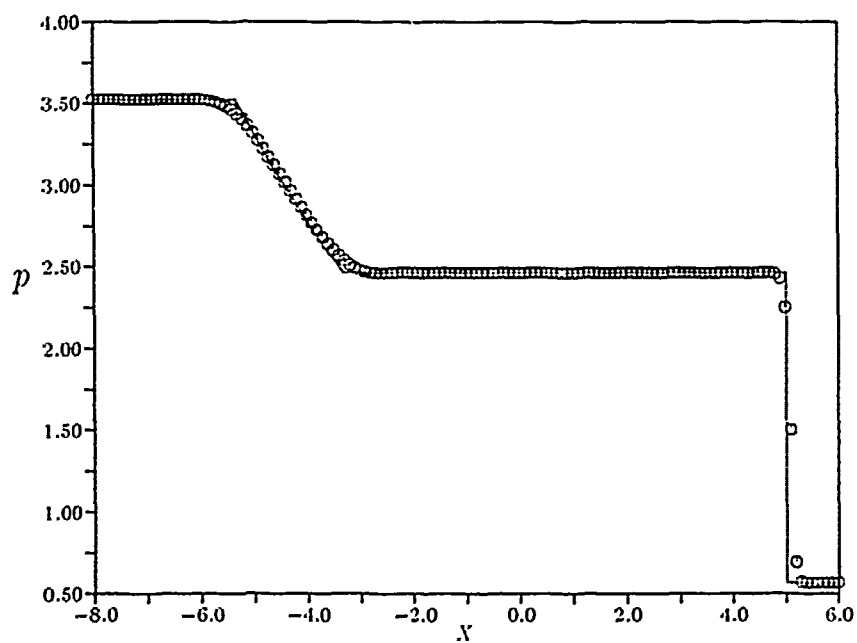
Figure 3.9. Pressure from ULT1C Scheme Applied to Riemann's Problem

34
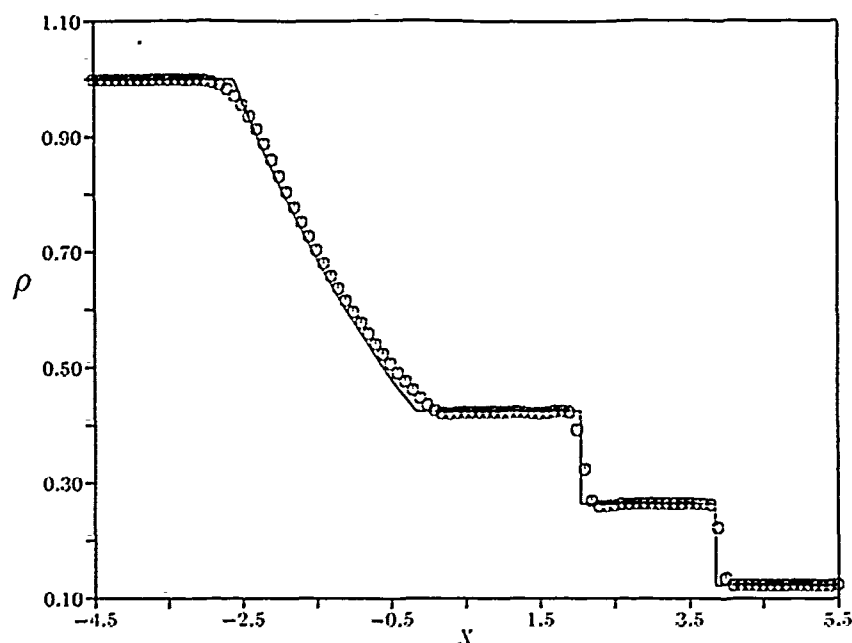
Figure 3.10. Density from ULT1C Applied to the Riemann Shock Tube

solution. This data is physically representative of a shock tube with

$$
U_L = \begin{bmatrix} 1 \\ 0 \\ 2.5 \end{bmatrix} \quad U_R = \begin{bmatrix} 0.125 \\ 0 \\ 0.250 \end{bmatrix} \tag{3.3}
$$

The calculations in this case were carried out to 50 time steps under the CFL restriction of 0.95 with 100 cells. consistent with Harten [22]. The results show excellent resolution of the contact discontinuity as well as the rarefaction and shock waves. The results appear to be identical with those of Harten.

3.2 Boundary Conditions for the Inviscid Studies

Appropriate boundary conditions. in conjunction with initial conditions and flow parameters such as Mach number. are necessary to arrive at the particular solution of interest. Boundary conditions for both the supersonic and transonic

35
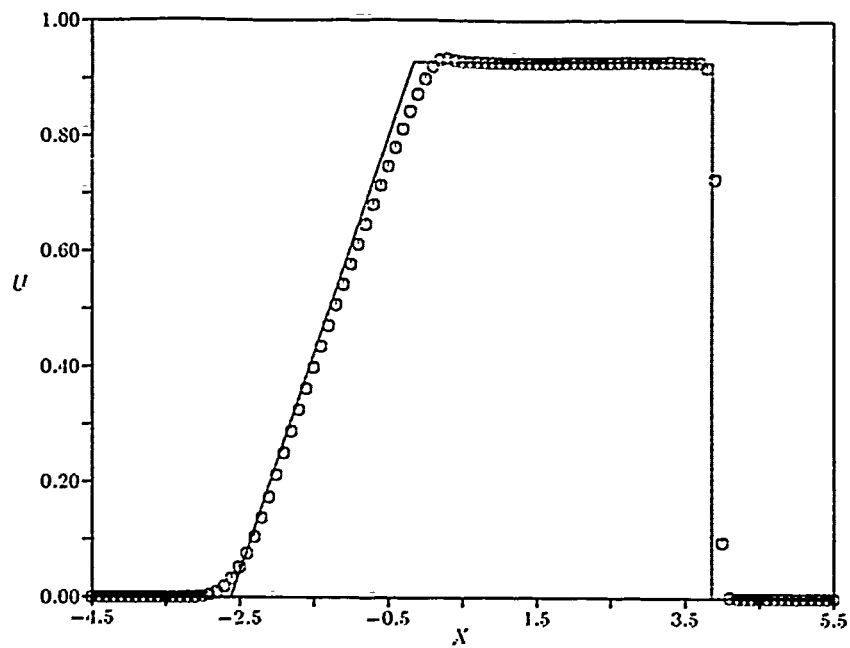
Figure 3.11. Velocity from ULT1C Applied to the Riemann Shock Tube
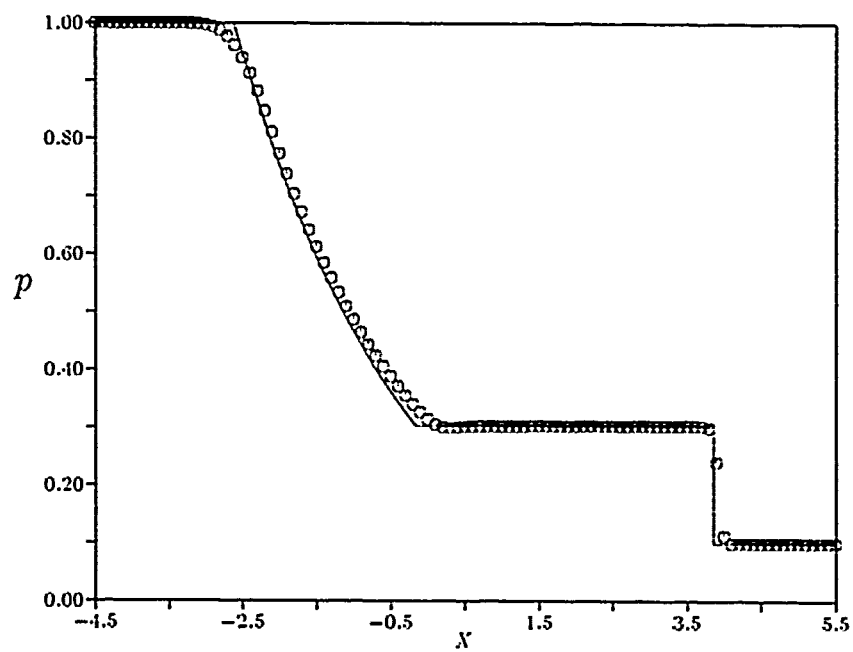
Figure 3.12. Pressure from ULT1C Applied to th: Riemann Shock Tube

cascade flows, to be discussed in forthcoming sections, are now described in detail.

3.2.1 Inlet and Exit Boundary Conditions. If the inlet velocity is supersonic, all characteristics originate upstream of the computational boundary so the four necessary flow quantities may be specified. Likewise, if the outflow velocity is supersonic all characteristics originate inside the computational domain and the four necessary exit quantities must be extrapolated from the interior. Second-order accurate extrapolation is utilized in the schemes under consideration.

Subsonic inflow and/or outflow presents a more complicated situation. In applying the boundary conditions at the inlet and exit of the domain, it is assumed that these boundaries are sufficiently distant from the cascade so that planar wave disturbances propagate collinearly with the stream function. The disturbances are required to leave the computational domain without reflection, except for the reflection of pressure disturbances at the exit. For subsonic inlet velocities, the inlet boundary conditions are arrived at by first assuming that the inlet is part of an imaginary duct extending infinitely far upstream of the cascade. All waves radiating from the computational domain should pass the inlet, without reflection, and continue travelling upstream for all time. Specification of a constant thermodynamic state at upstream infinity requires the expansion disturbance travelling upstream to behave as a simple wave. This behavior allows the application of one-dimensional characteristic theory at the inlet [16].

For subsonic inflow, only one characteristic runs from the interior of the domain towards the computational boundary. Therefore, three quantities must be specified while one may be extrapolated from the domain interior. Far upstream, the total pressure, p_{t_∞}, and total temperature, T_{t_∞}, are specified, while only the inlet flow angle, β_2, is specified at the computational boundary. The speed of sound at the inlet, c_2, is extrapolated from the domain interior. The Riemann invariant along the

37

characteristic spanning the expansion wave from leading to trailing edge is given by

$$V_\infty + \frac{2}{\gamma - 1} c_\infty = V_2 + \frac{2}{\gamma - 1} c_2$$

where V is the magnitude of the velocity vector. As the velocity vanishes far upstream, the inlet velocity is obtained from

$$V_2 = \frac{2}{\gamma - 1} \left(c_\infty - c_2 \right) \tag{3.5}$$

which, along with the inlet flow angle, determines u and v. The inlet pressure is determined from the isentropic relation

$$p_2 = p_\infty \left(\frac{c_2}{c_\infty} \right)^{2\gamma/(\gamma - 1)} \tag{3.6}$$

The speed of sound and pressure fix the state point, uniquely determining the density and internal energy.

For subsonic axial Mach numbers, simple-wave theory is also applied at the exit. The exit is treated as an open-end duct that exhausts into a plenum, requiring the exit pressure to match the plenum pressure. Thus, all pressure disturbances are reflected back into the computational domain from the exit. Two characteristics extend from the interior of the computational domain to the exit, while one originates outside the domain. Thus only one quantity, in this case pressure, can be specified at the exit. All other quantities must be extrapolated from the interior of the domain. The quantities chosen for extrapolation are entropy, tangential velocity, and the Riemann invariant, R_{inv}. The density is obtained from the isentropic relation

$$\rho_3 = \left(p_3 / s_{int} \right)^{1/\gamma} \tag{3.7}$$

where s_{int} is the entropy extrapolated from the interior. The pressure and density fix the state point, uniquely determining the speed of sound and internal energy. With

the tangential velocity extrapolated from the interior, the axial velocity is obtained by applying the Riemann invariant in the axial direction:

$$u_3 = R_{inv} - \frac{2}{\gamma - 1}c_3 \tag{3.8}$$

where

$$R_{inv} = u_{int} + \frac{2}{\gamma - 1}c_{int} \tag{3.9}$$

and u_{int} and c_{int} are the axial velocity and speed of sound at the point inside the domain where the Riemann invariant is evaluated.

3.2.2 Periodicity and Blade Boundary Conditions. Only one blade passage of an infinite cascade is analyzed. Therefore, periodicity conditions are applied at cell centers, or ghost points, located outside the computational domain. These points are located along the outer boundary and also along the wake cut when a C-type grid is utilized. For an H-type grid, ghost points are located along the upper and lower boundaries upstream and downstream of the blade. At the blade surface, the only condition that can be specified is the requirement for surface tangency. Since the blade surface is mapped to a constant η coordinate, the normal component of velocity is given by

$$V_n = \frac{\eta_x u + \eta_y v}{\sqrt{\eta_x^2 + \eta_y^2}} \tag{3.10}$$

while the tangential component is

$$V_t = \frac{\eta_y u - \eta_x v}{\sqrt{\eta_x^2 + \eta_y^2}} \tag{3.11}$$

The requirement for surface tangency is met by setting

$$V_{t_{j,0}} = V_{t_{j,1}} \tag{3.12}$$

and

$$V_{n_{j,0}} = -V_{n_{j,1}}$$
(3.13)

where j is the ξ index, 0 represents a ghost point just inside the body, and 1 is the index of the first cell center above the body. Cell centers and ghost points are used to place the blade surface along the interface of the grid cell and ghost cell. This mesh system helps ensure both consistent and conservative boundary conditions [35]. The inverse relation between the Cartesian velocities and Eqs 3.11 and 3.10 then gives

$$
\begin{bmatrix} u_{j,0} \\ v_{j,0} \end{bmatrix} = \frac{1}{\sqrt{\eta_x^2 + \eta_y^2}} \begin{bmatrix} \eta_y & \eta_x \\ -\eta_x & \eta_y \end{bmatrix} \begin{bmatrix} V_{t_{j,0}} \\ V_{n_{j,0}} \end{bmatrix}
$$
(3.14)

The pressure at the ghost points is obtained by applying the normal-momentum equation at the first line of cell centers above the body [33]:

$$
\begin{aligned}
-\rho \left(\xi_x u + \xi_y v \right) \left(\eta_x u_\xi + \eta_y v_\xi \right)' &= \left(\eta_x \xi_x + \xi_y \eta_y \right) p_\xi + \left(\eta_x^2 + \eta_y^2 \right) p_\eta \\
&= p_\eta \sqrt{\eta_x^2 + \eta_y^2}
\end{aligned}
$$
(3.15)

Central differences are used for both the ξ and η derivatives.

One additional property is needed to fix the state of the ghost points. In the present study, an adiabatic wall condition is chosen to provide this final property:

$$T_n = 0$$
(3.16)

Although it is inconsistent with the Euler equations to specify either the temperature or its gradient at the blade surface [35], an adiabatic wall condition has been used by others [33] and yields results that agree well with theory and experiment.
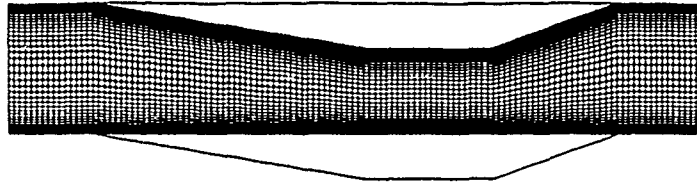
Figure 3.13. Grid for Cascade of Wedges

3.3 Cascade of Wedges

The cascade of wedges, previously examined by Denton [12] using his opposed difference scheme, is used to demonstrate the ability of the finite-volume TVD scheme to capture well defined oblique shocks. This cascade is shown in Figure 3.13. The cascade has an inlet Mach number of 2.0 and is designed such that the leading-edge shock is exactly cancelled upon reflection to the upstream corner, resulting in uniform flow between the two parallel surfaces. The grid used consists of 124 points in the axial direction and 40 points in the tangential direction. Grid points are clustered near the blade surface in order in improve the accuracy of the solution to the normal momentum equation, used to determine the pressure at the wall [33]. Results were obtained using $c_1 = 0.2$ for the nonlinear fields and 0 for the linearly degenerate fields. The computed pressure contours are shown in Figure 3.14. The shock that forms at the leading edge is well defined as is the reflected shock from the lower surface. Cancellation is achieved at the upstream corner resulting in the desired uniform flow between the parallel surfaces. This is in sharp contrast to the authors' experience with the MacCormack scheme which, due to shock smearing, places the reflected shock upstream of the corner allowing a weak shock to be reflected back across the passage [15]. Figure 3.14 also shows the well defined oblique shocks occuring at the trailing edge as a result of the periodicity condition. This shock structure is similar to the tramline shock structure [12] that can occur in a transonic turbine rotor.

41

Figure 3.15 contrasts the exact and computed solutions in terms of Mach number versus the non-dimensional chord length. Circles and squares denote the numerical solutions along the lower and upper blade surfaces, respectively. The solid line represents the exact solution. Unlike most second-order shock capturing methods, the TVD sheme does not display the dispersive errors, manifested through oscillations of the solution, that typically occur near points where shock and expansion waves are generated or reflected [15]. An exact solution for the expansion along the lower surface was not presented by Denton, but was computed by the author. Denton [12] attributes the exact solution to Brown Boveri & Co. of Baden, Switzerland.

3.4 High-Work Low-Aspect-Ratio Turbine

The finite-volume and chain-rule schemes were also applied to a transonic rotor cascade designed by NASA [42]. The experimental turbine is a 0.767 scale model of the first stage of a two-stage, high-pressure turbine designed for use in a high-bypass ratio engine. This model was tested in the NASA Lewis Research Center's Warm Core Turbine Test Facility [42].

Figure 3.16 shows the mean-line velocity diagram obtained from the NASA experiment. In the figure, V is the velocity in a stationary frame of reference, W is the velocity in a frame of reference moving with the rotor, and cr is a condition corresponding to a Mach number of unity. Subscripts 1, 2, and 3 correspond to the stator exit, rotor inlet and rotor exit respectively. Using the mean-line blade coordinates from reference [42], and the relative gas angles from Figure 3.16. the C-type grid shown in Figure 3.17 is constructed. The grid is made up of 177×20 points. again with points clustered near the surface for improved accuracy in applying the boundary conditions. The rounded trailing edge is replaced by a cusp to prevent the severe expansion around the blunt configuration. This was found not to be a necessary requirement on the trailing edge geometry, and solutions were obtained for a grid where the rounded trailing edge was left intact. Points are also clustered
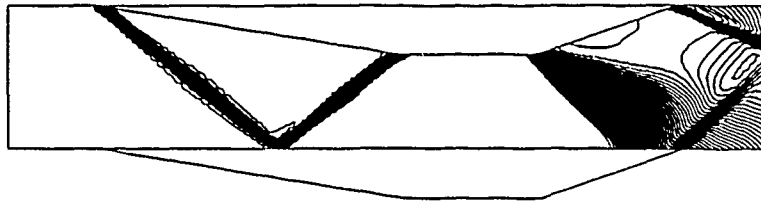
Figure 3.14. Wedge Pressure Contours
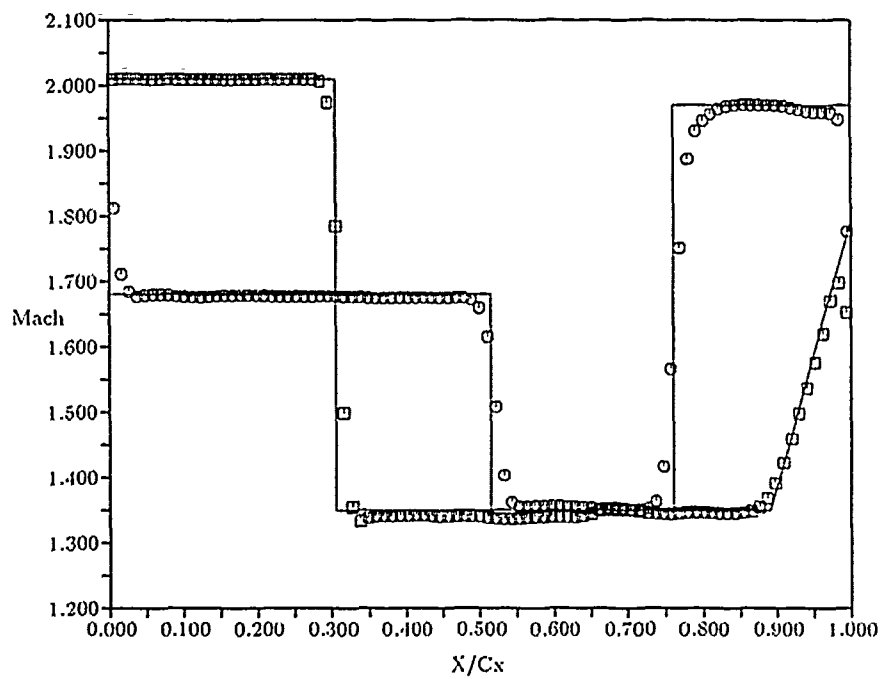
Figure 3.15. Blade Loading Diagram

43

$(V/V_{cr})_1 = 0.155$

$(V/V_{cr})_2 = 0.888$

$75.0°$

$49.2°$

$(W/W_{cr})_2 = 0.381$

$(U/V_{cr})_2 = 0.589$

$(W/W_{cr})_3 = 0.841$

$-66.5°$

$-23.2°$

$(V/V_{cr})_3 = 0.384$

$(U/V_{cr})_3 = 0.638$
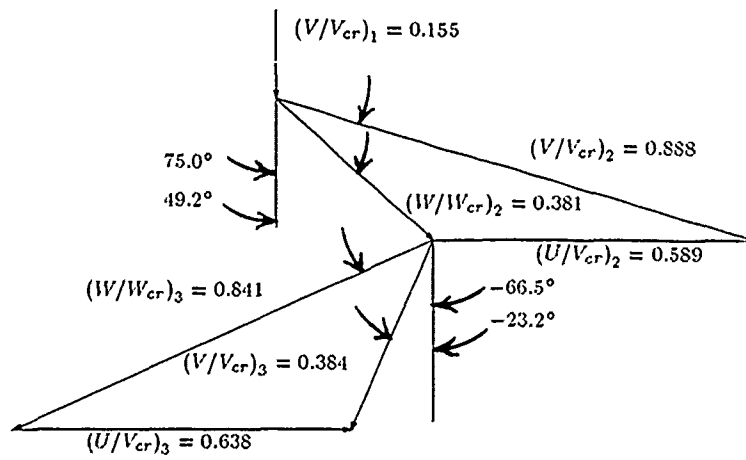
Figure 3.16. Mean-line Velocity Diagram
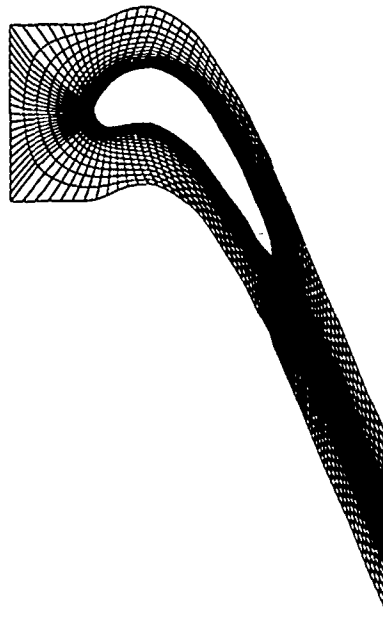
Figure 3.17. C-type Grid Used in the Present Analysis

at the leading and trailing edges for improved resolution. 21 points are placed along the portion of the C-type grid representing the inlet.

The inlet and exit condions necessary for input to the code are derived from the NASA test data [42] given in Table 3.1. In the table, t identifies total properties and R denotes a frame of reference moving with the rotor. Conditions at station 1, the stator exit, are taken to be the conditions also existing at station 2, the rotor inlet.

Consistent with subsonic inflow at the computational inlet, the total pressure and total temperature in the quiescent region infinitely far upstream of the cascade are required as boundary conditions. The values used are $p_{t_\infty} = 29.32 \times 10^4 N/m^2$ and $T_{t_\infty} = 420.2K$. The static pressure at station 3, the rotor exit, is input as the exit pressure. In particular, $p_3 = 12.05 \times 10^4 N/m^2$.

3.4.1 Numerical Solution. The initial conditions applied for the present study are referred to as "cascade tunnel start" conditions because of the analogy to the starting of a blow-down cascade tunnel. The domain is initialized at zero velocity, the pressure and temperature corresponding to that in the quiescent region upstream of the inlet. This is analogous to placing a diaphragm at the exit of the computational domain. At time t_0, the solution is started and a centered expansion wave propagates upstream. It is also possible to place the diaphragm anywhere in the computational domain, but placing it at the exit avoids the formation of a contact surface that must pass through the domain. While the present TVD scheme has demonstrated the ability to resolve such a contact surface in very fine detail, convergence is slowed due to the fact that the contact surface progresses through the domain at the convective velocity.

When the cascade tunnel start is used and the diaphragm is placed at the exit of the computational domain, a centered expansion wave propagates upsteam through the blade passage and towards the inlet. As the leading edge of the expansion

Table 3.1. NASA Turbine Test Data

$\gamma = 1.4$	Ratio of Specific Heats
$T_{t_1} = 422.2$ K	Inlet Total Temperature (Absolute)
$p_{t_1} = 31.03 \times 10^4 N/m^2$	Inlet Total Pressure (Absolute)
$p_{t_1}/p_2 = 1.704$	Inlet Total to Static Pressure Ratio (Absolute)
$p_{t_{2R}}/p_3 = 1.652$	Inlet Total to Exit Static Pressure Ratio (Relative)
$p_{t_1}/p_{t_3} = 2.360$	Inlet Total to Exit Total Pressure Ratio (Absolute)
$(V/V_{cr})_2 = 0.888$	Inlet Critical Velocity Ratio (Absolute)
$(V/V_{cr})_3 = 0.384$	Exit Critical Velocity Ratio (Absolute)
$(W/W_{cr})_2 = 0.381$	Inlet Critical Velocity Ratio (Relative)
$(W/W_{cr})_3 = 0.841$	Exit Critical Velocity Ratio (Relative)

wave reaches the leading edge of the airfoil, circulation is established around the blade through the shedding of a starting vortex from the airfoil. Since vorticity is related to the entopy gradient per Crocco's equation, entropy contours can be used to highlight regions of vorticity. Figure 3.18, a plot of the entropy contours after 1000 time steps, clearly shows the starting vortex that has been shed by the airfoil. The vortex is convected downstream and eventually exits the computational domain without being reflected. Figure 3.18 also provides a graphic representation of the periodic behavior in a cascade flow.

Steady-state solutions obtained with the finite-volume TVD formulation compares extremely well against the experimental mean-line data. Computational data is given in Table 3.2 for a C-type grid with 357×40 points. Grid spacing is roughly half that of the grid shown in Figure 6.42 and is utilized in an effort to verify the location of the stagnation point at the leading edge. Since the stagnation point is determined by the circulation around the airfoil, the entire grid was refined rather than just the area in the vicinity of the stagnation region. Computed values are compared against experimental values through the percent difference:

$$\%Diff = \left(\frac{X_{comp}}{X_{exp}} - 1 \right) \times 100 \qquad (3.17)$$

When the solution process was performed using the chain-rule formulation no noticeable difference in the computed quantities was observed. This level of agreement provides an excellent argument for the use of TVD schemes in computing transonic cascade flows.

3.5 Conclusions Based on Inviscid Investigations

TVD schemes, because of their foundation in the mathematics and physics of hyperbolic conservation laws, are clearly superior to the widely used Lax-Wendroff family of schemes that solve the partial differential equations without regard to
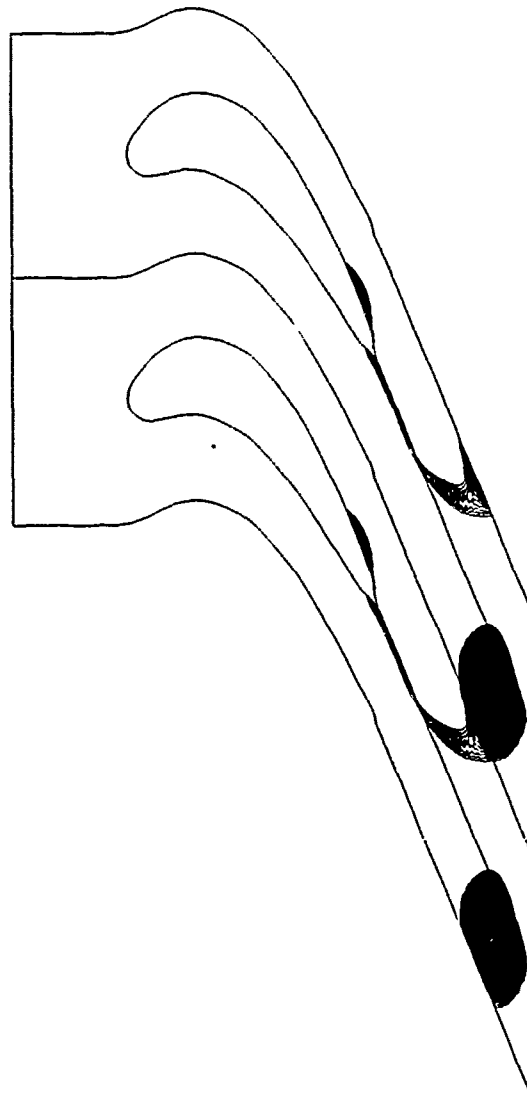
Figure 3.18. Entropy Contours Showing Starting Vortex

Table 3.2. Computed Versus Experimental Data

. Quantity	Experiment	Computed	% Difference
$P_{t_{2R}}/P_3$	1.652	1.643	−0.54
$P_{t_{3R}}$	$18.64 \times 10^4 N/m^2$	$18.98 \times 10^4 N/m^2$	1.82
$(W/W_{cr})_2$	0.381	0.383	0.52
$(W/W_{cr})_3$	0.841	0.853	1.43
Exit Angle, β_3	−66.50°	−66.75°	0.38

selecting the physically meaningful particular solution. The superior performance of TVD schemes in resolving rarefaction waves, contact discontinuities, and shock waves was demonstrated using Riemann's problem. Solutions for both supersonic and transonic flows exhibit greatly improved resolution over second-order Lax-Wendroff type schemes used previously [15, 16]. Solutions also compare favorably with the available experimental and analytical data.

One important improvement not mentioned previously is that the downstream periodic boundaries for the turbine analysis do not have to be treated as solid walls at any point during the solution process. Previous experience of the author and others [15, 16, 38] showed that numerical difficulties are encountered with the Mac-Cormack scheme if the cascade tunnel start is used. The downstream boundaries had to be treated as solid walls until the solution evolved to a point where the flow became aligned with the channel. No such difficulty has been observed with either the finite-volume or finite-difference TVD schemes described in Sections 2.2.2 and 2.2.3.

One observation should be made regarding grid cell skewness. While no adverse effects due to varying aspect ratio were observed for either the finite-volume or finite-difference formulations, excessive cell skewness in the turbine cascade grid led to a rather high degree of entropy production. This appears to be unrelated to boundary conditions since the production was most noticeable in the interior of the domain above the suction surface, where the grid tended to be most skewed. Reducing ϵ to 0 tended to alleviate the problem, suggesting that increased ϵ values tend to magnify the effect of numerical viscosity generated by cell skewness. The problem was observed with both the finite-volume and finite-difference formulations, although the finite-volume formulation tended to enhance the production of entropy. When the skewness was reduced, no noticeable differences in the solutions using either formulation were observed. No significant variation in the solutions is observed for ϵ values ranging from 0 to 0.4 in the nonlinear fields, so long as skewness is kept to a minimum. A value of $\epsilon = 0$ was consistently used for the linearly degenerate fields.

CFL numbers as high as 0.95 were consistently used to obtain steady-state results. In fact, the CFL number was dropped to 0.5 only if a contact surface was in the vicinity of the rounded trailing edge of the blade. At all other times the CFL number was maintained at 0.95. This is in contrast to CFL numbers as low as 0.2 required during startup and only as high as 0.8 to maintain stability when using the MacCormack scheme [15, 16].

The data processing rate is 1.2425×10^{-5} seconds per grid point per time level for the chain-rule formulation, and 1.2271×10^{-5} seconds per grid point per time level for the finite-volume formulation; the processing rate refers to the CRAY X-MP/216 computer. The solution is monitored until calculations consistently show less than a 0.02% change in the total energy. The time dependent solution is then considered to have asymptoted to the steady-state solution. A typical, time-accurate calculation requires approximately 4000 operator sweeps to achieve steady state convergence. This translates to approximately 5.8 minutes of CRAY X-MP/216 CPU time for the

177×20 grid. When a local time stepping procedure is used, approximately 2000 time steps are required to achieve the same level of convergence. Thus the CPU time is reduced by a factor of two. A description of the ATEC routines is presented in Appendix B. Appendix B also summarizes the results of the CRAY FLOWTRACE option used to obtain a relative performance evaluation of the routines.

IV. Introduction to Part II

4.1 TVD Schemes and the Navier-Stokes Equations

Soon after the introduction of the TVD methodology by Harten [22] the scheme began to be applied to the Navier-Stokes equations. The earliest application known to the author was by Chakravarthy et al. [7] in 1985, followed by Müller [32] in 1989, Riedelbauch and Brenner [34] in 1990, and Lin and Chieng [25], Seider and Hänel [39], and Josyula, Gaitonde, and Shang [24] all in 1991. All these investigations dealt exclusively with the steady-state problem. Numerous other researchers have undoubtedly applied the TVD methodology to the Navier-Stokes equations, but the author is mainly aware of the above efforts. Most of the effort has been directed toward the investigation of hypersonic flows, but Lin and Chieng and Seider and Hänel have investigated the transonic regime through solutions of the thin-layer Navier-Stokes equations.

The present effort is an attempt to extend the application of the TVD methodology in two directions. The first direction is the calculation of unsteady flows, where the time accuracy of the scheme is important. The second direction concerns flows where complex wave pheomena are present, but are relatively weak compared to those of previous investigations. A primary assumption of previous investigations is that the flows are dominated by inviscid effects: moderate or strong shock waves are present in the flowfield. This assumption allowed investigators to conclude that solutions far away from the boundary-layer are accurate, even though the effect of the TVD dissipation terms on the true viscosity in the boundary layer remained unknown [45]. Seider and Hänel were the first to investigate the effect of this dissipation on the boundary layer and the present work attemps to extend this knowledge.

4.2 Overview of Part II

The present effort is primarily concerned with the development of an algorithm capable of analyzing laminar flows with boundary-layer separation and heat transfer induced by both steady and unsteady shock waves. Several algorithms have been developed that are reasonably accurate in predicting pressure distributions for the laminar shock-boundary-layer interaction problem. To the author's knowledge no algorithms, other than those developed herein, currently exist that accurately predict skin friction coefficients in the interaction region or the correct separation and reattachment locations. Similarly, no algorithm is available that accurately computes local heat flux for even the simplest geometries when shock waves impinge upon the boundary layer.

To accurately compute the complex flow structure of shock-induced boundary-layer separation, or compute accurate heat flux levels, the algorithm must provide for high resolution of the complex wave systems and maintain the proper physical behavior of the problem under consideration. TVD schemes, which lend themselves to limited, but extremely rigorous, analysis provide the best foundation to build upon. Although developed for the solution of scalar hyperbolic conservation laws. TVD schemes perform well on systems of hyperbolic equations, such as the Riemann problem analyzed in Part I. The TVD methodology is adapted herein to provide accurate solutions to the parabolic Navier-Stokes equations.

Part II begins with the casting of the Navier-Stokes equations in conservative form, after which the system is linearized. Two versions of TVD algorithms. the 1st-Order AFIT TVD Navier-Stokes Code (ATNSC1) and the 2nd-Order AFIT TVD Navier-Stokes Code (ATNSC2). are then developed. Both algorithms are extensions of the Harten-Yee inviscid algorithm outlined in Section 2.2.3. ATNSC1 is formally first-order accurate in time. second-order accurate in space. ATNSC2 is formally second-order accurate in time and space. ATNSC1 and ATNSC2 are first applied, along with a Lax-Wendroff algorithm. to the viscous Burgers' equation as a test case.

This test case illustrates the superior performance of the ATNSC schemes, as well as the necessity of utilizing the fully second-order ATNSC2 algorithm for low Reynolds number flows. The ATNSC algorithms are then applied to the solution of the shock-boundary-layer interaction problem. Computed solutions are compared with the experimental data of Hakkinen et al., and with solutions obtained from Visbal's Beam-Warming algorithm [47], in order to illustrate the superior performance of the TVD based algorithms.

The ATNSC algorithms are next applied to the problem of unsteady shock-induced heat transfer. Solutions are compared with those obtained from Visbal's Beam-Warming algorithm, the theory of Mirels [30], and the experimental data of Smith [41]. ATNSC solutions are shown to behave in a physically correct manner, providing extremely accurate solutions. The Beam-Warming algorithm allows the formation of nonphysical waves, including expansion shocks, for this test case.

Finally, conclusions arrived at from the current investigation are summarized. Suggestions are also given for further research involving use of the ATNSC algorithms.

V. Viscous Analysis

5.1 Navier-Stokes Equations

The conservative form of the Navier-Stokes equations is written as

$$\frac{\partial U}{\partial t} + \frac{\partial F(U)}{\partial x} + \frac{\partial G(U)}{\partial y} = \frac{\partial F_v(U, U_x, U_y)}{\partial x} + \frac{\partial G_v(U, U_x, U_y)}{\partial y} \qquad (5.1)$$

where U, F, and G are the same as for the Euler equations, Eq 2.1. F_v and G_v are the viscous flux terms, given as

$$F_v = \begin{bmatrix} 0 \\ \tau_{xx} \\ \tau_{xy} \\ u\tau_{xx} + v\tau_{xy} - q_x \end{bmatrix} \quad G_v = \begin{bmatrix} 0 \\ \tau_{xy} \\ \tau_{yy} \\ u\tau_{xy} + v\tau_{yy} - q_y \end{bmatrix} \qquad (5.2)$$

τ_{xx}, τ_{xy}, and τ_{yy} are the viscous stresses:

$$\tau_{xx} = (2\mu + \lambda)u_x + \lambda v_y$$
$$\tau_{xy} = \mu\left(u_y + v_x\right) \qquad (5.3)$$
$$\tau_{yy} = (2\mu + \lambda)v_y + \lambda u_x$$

where μ and λ are the first and second coefficients of viscosity respectively. The first coefficient of viscosity is determined using Sutherland's formula [1];

$$\mu = C_1 \frac{T^{3/2}}{T + C_2} \qquad (5.4)$$

where $C_1 = 1.458 \times 10^{-6} \ kg/\left(m \cdot s \cdot \sqrt{K}\right)$ and $C_2 = 110.4 \ K$. The second coefficient of viscosity is given by

$$B = 2 + \frac{\lambda}{\mu} \qquad (5.5)$$

where $B = 4/3$ yields Stoke's hypothesis, $\lambda = -2/3\mu$. Solutions were also arrived at using $B = 2$, based on Sherman's work as reported by White [49]. No difference was observed in the numerical solutions using $B = 4/3$ or $B = 2$.

The quantities q_x and q_y are components of the heat flux vector, $q = -k\nabla T$. The coefficient of thermal conductivity, k, is determined from the Prandtl number, Pr:

$$Pr = \frac{\mu C_p}{k} \tag{5.6}$$

with $Pr = 0.72$ for air.

The equations may be written in linearized form as

$$U_t + AU_x + BU_y = A_1 U_x + B_1 U_y + A_2 U_{xx} + B_2 U_{yy} + (A_3 + B_3) U_{xy} \tag{5.7}$$

where the viscous Jacobian matrices are

$$
\begin{aligned}
A_1 &= \partial F_v/\partial U & A_2 &= \partial F_v/\partial U_x & A_3 &= \partial F_v/\partial U_y \\
B_1 &= \partial G_v/\partial U & B_2 &= \partial G_v/\partial U_y & B_3 &= \partial G_v/\partial U_x
\end{aligned}
\tag{5.8}
$$

with the individual terms given in Appendix A.

A general spatial transformation of the form $\xi = \xi(x,y)$ and $\eta = \eta(x,y)$ is used to transform Eq 5.7 from the physical domain (x,y) to the computational domain (ξ,η):

$$U_t + \hat{A}U_\xi + \hat{B}U_\eta = \hat{A}_1 U_\xi + \hat{B}_1 U_\eta + \hat{A}_2 U_{\xi\xi} + \hat{B}_2 U_{\eta\eta} + \left(\hat{A}_3 + \hat{B}_3\right) U_{\xi\eta} \tag{5.9}$$

where

$$
\begin{aligned}
\hat{A} &= \xi_x A + \xi_y B \\
\hat{A}_1 &= \xi_x A_1 + \xi_y B_1 \\
\hat{A}_2 &= \xi_x^2 A_2 + \xi_y^2 B_2 + \xi_x \xi_y (A_3 + B_3) \\
\hat{A}_3 &= \xi_x \eta_y A_3 + \xi_y \eta_x B_3 + \xi_x \eta_x A_2 + \xi_y \eta_y B_2
\end{aligned}
\tag{5.10}
$$

56

and

$$
\begin{aligned}
\hat{B} &= \eta_x A + \eta_y B \\
\hat{B}_1 &= \eta_x A_1 + \eta_y B_1 \\
\hat{B}_2 &= \eta_x^2 A_2 + \eta_y^2 B_2 + \eta_x \eta_y \left(A_3 + B_3 \right) \\
\hat{B}_3 &= \xi_x \eta_y B_3 + \xi_y \eta_x A_3 + \xi_x \eta_x A_2 + \xi_y \eta_y B_2
\end{aligned}
\tag{5.11}
$$

5.2 Numerical Procedure

5.2.1 1st-Order Time, 2nd-Order Space Algorithm.

A first-order time, second-order space, upwind TVD scheme is now presented for the Navier-Stokes equations. Based upon the excellent results achieved in the inviscid case, a chain-rule formulation is utilized. The scheme for the Euler equations, described in Section 2.2.3, is second-order accurate in space and time. Taylor series expansion shows the scheme is a representation of

$$
\begin{aligned}
U_t + \xi_x F_\xi + \eta_x F_\eta + \xi_y G_\xi + \eta_y G_\eta &= \tfrac{\Delta t}{2} \left[-U_{tt} + \hat{A}^2 U_{\xi\xi} + \left(\hat{A}\hat{B} + \hat{B}\hat{A} \right) U_{\xi\eta} \right. \\
&\left. + \hat{B}^2 U_{\eta\eta} \right] + O\left[\Delta t^2, \Delta \xi^2, \Delta \eta^2 \right]
\end{aligned}
\tag{5.12}
$$

and is second-order accurate for the Euler equations, since

$$
U_{tt} = \hat{A}^2 U_{\xi\xi} + \left(\hat{A}\hat{B} + B\hat{A} \right) U_{\xi\eta} + \hat{B}^2 U_{\eta\eta}
\tag{5.13}
$$

Viscous terms are added to the Euler scheme, Eqs 2.61 and 2.62, using second-order accurate, central-difference approximations:

$$
\mathcal{L}_\xi^h U_{j,k}^n = U_{j,k}^* = U_{j,k}^n - \frac{\Delta t}{\Delta \xi} \left(\tilde{F}_{j+\frac{1}{2},k}^n - \tilde{F}_{j-\frac{1}{2},k}^n \right) - \Delta t \Psi_\xi^n
\tag{5.14}
$$

$$
\mathcal{L}_\eta^h U_{j,k}^* = U_{j,k}^* - \frac{\Delta t}{\Delta \eta} \left(\tilde{G}_{j,k+\frac{1}{2}}^* - \tilde{G}_{j,k-\frac{1}{2}}^* \right) + \Delta t \Psi_\eta^*
\tag{5.15}
$$

57

where $\tilde{F}$ and $\tilde{G}$ are given by Eqs 2.63 and 2.64. The viscous terms, Ψ_ξ and Ψ_η, are

$$\Psi_\xi = \frac{1}{2\Delta\xi} \left[(\xi_x)_{j,k} \left(F_{v_{j+1,k}} - F_{v_{j-1,k}} \right) + (\xi_y)_{j,k} \left(G_{v_{j+1,k}} - G_{v_{j-1,k}} \right) \right] \quad (5.16)$$

and

$$\Psi_\eta = \frac{1}{2\Delta\eta} \left[(\eta_x)_{j,k} \left(F_{v_{j,k+1}} - F_{v_{j,k-1}} \right) + (\eta_y)_{j,k} \left(G_{v_{j,k+1}} - G_{v_{j,k-1}} \right) \right] \quad (5.17)$$

The scheme given by Eqs 5.14 through 5.17 is a representation of

$$
\begin{aligned}
U_t + \xi_x F_\xi + \eta_x F_\eta + \xi_y G_\xi + \eta_y G_\eta &= \xi_x F_{v_\xi} + \eta_x F_{v_\eta} + \xi_y G_{v_\xi} + \eta_y G_{v_\eta} \\
&\quad + \frac{\Delta t}{2} \left[-U_{tt} + \hat{A}^2 U_{\xi\xi} + \left(\hat{A}\hat{B} + \hat{B}\hat{A} \right) U_{\xi\eta} \right. \\
&\quad \left. + \hat{B}^2 U_{\eta\eta} \right] + O\left[\Delta t^2, \Delta\xi^2, \Delta\eta^2 \right]
\end{aligned}
$$
$$(5.18)$$

Examination of Eq 5.9 reveals

$$
\begin{aligned}
U_{tt} &= \left(\hat{B}^2 + \hat{B}_1^2 - \hat{B}\hat{B}_1 - \hat{B}_1\hat{B} \right) U_{\eta\eta} \\
&\quad + \left(\hat{A}_1\hat{B}_1 + \hat{B}_1\hat{A}_1 - \hat{A}_1\hat{B} - \hat{B}\hat{A}_1 - \hat{A}\hat{B}_1 - \hat{B}_1\hat{A} + \hat{A}\hat{B} + \hat{B}\hat{A} \right) U_{\xi\eta} \\
&\quad + \left(\hat{B}_1\hat{B}_2 + \hat{B}_2\hat{B}_1 - \hat{B}\hat{B}_2 - \hat{B}_2\hat{B} \right) U_{\eta\eta\eta} + \hat{B}_2^2 U_{\eta\eta\eta\eta} \\
&\quad + \left(\hat{B}_3\hat{B}_1 + \hat{B}_1\hat{B}_3 - \hat{B}_3\hat{B} - \hat{B}\hat{B}_3 + \hat{B}_1\hat{A}_3 + \hat{A}_3\hat{B}_1 \right. \\
&\quad \left. -\hat{B}\hat{A}_3 - \hat{A}_3\hat{B} + \hat{B}_2\hat{A}_1 + \hat{A}_1\hat{B}_2 - \hat{B}_2\hat{A} - \hat{A}\hat{B}_2 \right) U_{\xi\eta\eta} \\
&\quad + \left(\hat{B}_2\hat{B}_3 + \hat{B}_3\hat{B}_2 + \hat{B}_2\hat{A}_3 + \hat{A}_3\hat{B}_2 \right) U_{\xi\eta\eta\eta} \\
&\quad + \left(\hat{B}_3^2 + \hat{A}_3^2 + \hat{A}_2\hat{B}_2 + \hat{B}_2\hat{A}_2 + \hat{A}_3\hat{B}_3 + \hat{B}_3\hat{A}_3 \right) U_{\xi\xi\eta\eta} \\
&\quad + \left(\hat{A}_3\hat{A}_1 + \hat{A}_1\hat{A}_3 - \hat{A}_3\hat{A} - \hat{A}\hat{A}_3 + \hat{A}_1\hat{B}_3 + \hat{B}_3\hat{A}_1 \right. \\
&\quad \left. -\hat{A}\hat{B}_3 - \hat{B}_3\hat{A} + \hat{A}_2\hat{B}_1 + \hat{B}_1\hat{A}_2 - \hat{A}_2\hat{B} - \hat{B}\hat{A}_2 \right) U_{\xi\xi\eta} \\
&\quad + \left(\hat{A}_2\hat{A}_3 + \hat{A}_3\hat{A}_2 + \hat{A}_2\hat{B}_3 + \hat{B}_3\hat{A}_2 \right) U_{\xi\xi\xi\eta} \\
&\quad + \left(\hat{A}^2 + \hat{A}_1^2 - \hat{A}\hat{A}_1 - \hat{A}_1\hat{A} \right) U_{\xi\xi} \\
&\quad + \left(\hat{A}_1\hat{A}_2 + \hat{A}_2\hat{A}_1 - \hat{A}\hat{A}_2 - \hat{A}_2\hat{A} \right) U_{\xi\xi\xi} + \hat{A}_2^2 U_{\xi\xi\xi\xi} \quad (5.19)
\end{aligned}
$$

58

Since the term of $O[\Delta t]$ in the truncation error of Eq 5.18 does not vanish upon substitution of Eq 5.19, the scheme obtained by adding central-difference representations of the viscous terms to the Euler scheme, Eqs 5.14 through 5.17, is first-order accurate in time and second-order accurate in space. This new scheme represents

$$U_t + \xi_x F_\xi + \eta_x F_\eta + \xi_y G_\xi + \eta_y G_\eta = \xi_x F_{v_\xi} + \eta_x F_{v_\eta} + \xi_y G_{v_\xi} + \eta_y G_{v_\eta} \\ + O\left[\Delta t, \Delta \xi^2, \Delta \eta^2\right] \tag{5.20}$$

This first-order time, second-order space scheme is hereafter referred to as ATNSC1 which is shorthand for 1st-Order AFIT TVD Navier-Stokes Code. A description of the ATNSC1 routines is contained in Appendix C. Also included is a relative performance evaluation of the routines, obtained using the CRAY FLOWTRACE option.

5.2.2 2nd-Order Time, 2nd-Order Space Algorithm. All known TVD solutions to the Navier-Stokes equations, prior to the present effort, have implemented the viscous terms in a manner analogous to that of Section 5.2.1. A second-order accurate, upwind TVD scheme is now developed for the Navier-Stokes equations. As previously mentioned, the scheme for the Euler equations is second-order accurate in space and time and is a representation of Eq 5.12. Utilizing the fractional step method, consider a scheme of the following form for solution of the Navier-Stokes equations:

$$U_{j,k}^{n+2} = \mathcal{L}_\eta^h \mathcal{L}_\xi^h \mathcal{L}_\xi^h \mathcal{L}_\eta^h U_{j,k}^n \tag{5.21}$$

where

$$\begin{aligned} \mathcal{L}_\xi^h U_{j,k}^n = U_{j,k}^* &= U_{j,k}^n - \frac{\Delta t}{\Delta \xi} \left(\tilde{F}_{j+\frac{1}{2},k}^n - \tilde{F}_{j-\frac{1}{2},k}^n \right) + \Delta t \Psi_\xi^n \\ &= \left(1 - \Delta t \hat{A} \delta_\xi + \frac{\Delta t^2}{2} \hat{A}^2 \delta_\xi^2 \right) U_{j,k}^n + \Delta t \Psi_\xi^n \end{aligned} \tag{5.22}$$

59

and

$$\mathcal{L}_\eta^h U_{j,k}^n = U_{j,k}^* - \frac{\Delta t}{\Delta \eta} \left(\tilde{G}_{j,k+\frac{1}{2}}^n - \tilde{G}_{j,k-\frac{1}{2}}^* \right) + \Delta t \Psi_\eta^*$$

$$= \left(1 - \Delta t \hat{B} \delta_\eta + \frac{\Delta t^2}{2} \hat{B}^2 \delta_\eta^2 \right) U_{j,k}^* + \Delta t \Psi_\eta^* \qquad (5.23)$$

where $h = \Delta t$. The numerical viscous flux derivative, Ψ, is the representation of the viscous derivatives terms plus terms necessary to cancel any first-order truncation error. Above, δ_l^k represents a second-order accurate (centered) difference approximation of the kth derivative with respect to l. The functions $\tilde{F}_{j+\frac{1}{2},k}$ and $\tilde{G}_{j,k+\frac{1}{2}}$ are the same numerical fluxes as for the Euler equations, Eqs 2.63 and 2.64.

$\mathcal{L}_\xi^h U$ provides a second-order accurate solution to the one-dimensional equation

$$U_t + \hat{A} U_\xi = \psi_\xi - \frac{\Delta t}{2} U_{tt} + \frac{\Delta t}{2} \hat{A}^2 U_{\xi\xi} + O \left[\Delta t^2, \Delta \xi^2 \right] \qquad (5.24)$$

while $\mathcal{L}_\eta^h U$ provides a second-order accurate solution to

$$U_t + \hat{B} U_\eta = \psi_\eta - \frac{\Delta t}{2} U_{tt} + \frac{\Delta t}{2} \hat{B}^2 U_{\eta\eta} + O \left[\Delta t^2, \Delta \eta^2 \right] \qquad (5.25)$$

In the two equations above, ψ is the exact representation of the viscous flux derivatives plus terms necessary to cancel any first-order truncation error.

Subtracting selected viscous terms from the two equations above gives quasi-one-dimensional forms of the Navier-Stokes equations on the left-hand sides:

$$\begin{aligned} U_t + \hat{A} U_\xi - \hat{A}_1 U_\xi - \hat{A}_2 U_{\xi\xi} - \hat{A}_3 U_{\xi\eta} &= \psi_\xi - \frac{\Delta t}{2} U_{tt} + \frac{\Delta t}{2} \hat{A}^2 U_{\xi\xi} \\ &\quad - \hat{A}_1 U_\xi - \hat{A}_2 U_{\xi\xi} - \hat{A}_3 U_{\xi\eta} \end{aligned} \qquad (5.26)$$

$$\begin{aligned} U_t + \hat{B} U_\eta - \hat{B}_1 U_\eta - \hat{B}_2 U_{\eta\eta} - \hat{B}_3 U_{\xi\eta} &= \psi_\eta - \frac{\Delta t}{2} U_{tt} + \frac{\Delta t}{2} \hat{B}^2 U_{\eta\eta} \\ &\quad - \hat{B}_1 U_\eta - \hat{B}_2 U_{\eta\eta} - \hat{B}_3 U_{\xi\eta} \end{aligned} \qquad (5.27)$$

60

The objective is to select ψ such that the right-hand sides of Eqs 5.26 and 5.27 equal zero, yielding the quasi-one-dimensional Navier-Stokes equations:

$$U_t + \hat{A}U_\xi - \hat{A}_1 U_\xi - \hat{A}_2 U_{\xi\xi} - \hat{A}_3 U_{\xi\eta} = 0 \tag{5.28}$$

$$U_t + \hat{B}U_\eta - \hat{B}_1 U_\eta - \hat{B}_2 U_{\eta\eta} - \hat{B}_3 U_{\xi\eta} = 0 \tag{5.29}$$

Examining the quasi-one-dimensional Navier-Stokes equation in the ξ-direction gives

$$
\begin{aligned}
U_{tt} &= \left(\hat{A}^2 - \hat{A}\hat{A}_1 - \hat{A}_1\hat{A} + \hat{A}_1^2\right)U_{\xi\xi} \\
&\quad + \left(\hat{A}_1\hat{A}_2 + \hat{A}_2\hat{A}_1 - \hat{A}\hat{A}_2 - \hat{A}_2\hat{A}\right)U_{\xi\xi\xi} + \hat{A}_2^2 U_{\xi\xi\xi\xi} \\
&\quad + \left(\hat{A}_1\hat{A}_3 + \hat{A}_3\hat{A}_1 - \hat{A}\hat{A}_3 - \hat{A}_3\hat{A}\right)U_{\xi\xi\eta} \\
&\quad + \left(\hat{A}_2\hat{A}_3 + \hat{A}_3\hat{A}_2\right)U_{\xi\xi\xi\eta} + \hat{A}_3^2 U_{\xi\xi\eta\eta} \quad \cdot
\end{aligned} \tag{5.30}
$$

Substitution of U_{tt} into Eq 5.26, and setting the left-hand side equal to zero, yields

$$
\begin{aligned}
\psi_\xi &= \frac{\partial F_v}{\partial \xi} + \frac{\Delta t}{2}\left[\left(\hat{A}_1^2 - \hat{A}\hat{A}_1 - \hat{A}_1\hat{A}\right)U_{\xi\xi}\right. \\
&\quad + \left(\hat{A}_1\hat{A}_2 + \hat{A}_2\hat{A}_1 - \hat{A}\hat{A}_2 - \hat{A}_2\hat{A}\right)U_{\xi\xi\xi} + \hat{A}_2^2 U_{\xi\xi\xi\xi} \\
&\quad + \left(\hat{A}_1\hat{A}_3 + \hat{A}_3\hat{A}_1 - \hat{A}\hat{A}_3 - \hat{A}_3\hat{A}\right)U_{\xi\xi\eta} \\
&\quad \left. + \left(\hat{A}_2\hat{A}_3 + \hat{A}_3\hat{A}_2\right)U_{\xi\xi\xi\eta} + \hat{A}_3^2 U_{\xi\xi\eta\eta}\right]
\end{aligned} \tag{5.31}
$$

Similar manipulation of the η-direction equation gives

$$
\begin{aligned}
\psi_\eta &= \frac{\partial G_v}{\partial \eta} + \frac{\Delta t}{2}\left[\left(\hat{B}_1^2 - \hat{B}\hat{B}_1 - \hat{B}_1\hat{B}\right)U_{\eta\eta}\right. \\
&\quad + \left(\hat{B}_1\hat{B}_2 + \hat{B}_2\hat{B}_1 - \hat{B}\hat{B}_2 - \hat{B}_2\hat{B}\right)U_{\eta\eta\eta} + \hat{B}_2^2 U_{\eta\eta\eta\eta} \\
&\quad + \left(\hat{B}_1\hat{B}_3 + \hat{B}_3\hat{B}_1 - \hat{B}\hat{B}_3 - \hat{B}_3\hat{B}\right)U_{\xi\eta\eta} \\
&\quad \left. + \left(\hat{B}_2\hat{B}_3 + \hat{B}_3\hat{B}_2\right)U_{\xi\eta\eta\eta} + \hat{B}_3^2 U_{\xi\xi\eta\eta}\right]
\end{aligned} \tag{5.32}
$$

61

Applying the fractional step operators, as in Eq 5.21, with the numerical viscous flux derivatives given by

$$
\begin{aligned}
\Psi_\xi \;=\; & \delta_\xi F_v + \frac{\Delta t}{2}\left[\left(\hat{A}_1^2 - \hat{A}\hat{A}_1 - \hat{A}_1\hat{A}\right)\delta_\xi^2 \right.\\
& + \left(\hat{A}_1\hat{A}_2 + \hat{A}_2\hat{A}_1 - \hat{A}\hat{A}_2 - \hat{A}_2\hat{A}\right)\delta_\xi^3 + \hat{A}_2^2\delta_\xi^4 \\
& + \left(\hat{A}_1\hat{A}_3 + \hat{A}_3\hat{A}_1 - \hat{A}\hat{A}_3 - \hat{A}_3\hat{A}\right)\delta_{\xi\xi\eta}^3 \\
& \left. + \left(\hat{A}_2\hat{A}_3 + \hat{A}_3\hat{A}_2\right)\delta_{\xi\xi\xi\eta}^4 + \hat{A}_3^2\delta_{\xi\xi\eta\eta}^4\right]U
\end{aligned}
\tag{5.33}
$$

and

$$
\begin{aligned}
\Psi_\eta \;=\; & \delta_\eta G_v + \frac{\Delta t}{2}\left[\left(\hat{B}_1^2 - \hat{B}\hat{B}_1 - \hat{B}_1\hat{B}\right)\delta_\eta^2 \right.\\
& + \left(\hat{B}_1\hat{B}_2 + \hat{B}_2\hat{B}_1 - \hat{B}\hat{B}_2 - \hat{B}_2\hat{B}\right)\delta_\eta^3 + \hat{B}_2^2\delta_\eta^4 \\
& + \left(\hat{B}_1\hat{B}_3 + \hat{B}_3\hat{B}_1 - \hat{B}\hat{B}_3 - \hat{B}_3\hat{B}\right)\delta_{\xi\eta\eta}^3 \\
& \left. + \left(\hat{B}_2\hat{B}_3 + \hat{B}_3\hat{B}_2\right)\delta_{\xi\eta\eta\eta}^4 + \hat{B}_3^2\delta_{\xi\xi\eta\eta}^4\right]U
\end{aligned}
\tag{5.34}
$$

results in

$$
\begin{aligned}
U_{j,k}^{n+2} \;=\; & \mathcal{L}_\eta^h \mathcal{L}_\xi^h \mathcal{L}_\xi^h \mathcal{L}_\eta^h U_{j,k}^n \\
=\; & \Big\{ 1 + 2\Delta t\,\big\{\ \left(\hat{B}_1 - \hat{B}\right)\delta_\eta + \left[\left(\hat{B}^2 + \hat{B}_1^2 - \hat{B}\hat{B}_1 - \hat{B}_1\hat{B}\right)\Delta t + \hat{B}_2\right]\delta_\eta^2 \\
& + \left[\hat{B}_3 + \hat{A}_3 + \left(\hat{A}_1\hat{B}_1 + \hat{B}_1\hat{A}_1 - \hat{A}_1\hat{B} - \hat{B}\hat{A}_1 - \hat{A}\hat{B}_1 - \hat{B}_1\hat{A} + \hat{A}\hat{B} + \hat{B}\hat{A}\right)\Delta t\right]\delta_{\xi\eta}^2 \\
& + \left(\hat{B}_1\hat{B}_2 + \hat{B}_2\hat{B}_1 - \hat{B}\hat{B}_2 - \hat{B}_2\hat{B}\right)\Delta t\delta_\eta^3 + \hat{B}_2^2\Delta t\delta_\eta^4 \\
& + \left(\hat{B}_3\hat{B}_1 + \hat{B}_1\hat{B}_3 - \hat{B}_3\hat{B} - \hat{B}\hat{B}_3 + \hat{B}_1\hat{A}_3 + \hat{A}_3\hat{B}_1 \right.\\
& \left. - \hat{B}\hat{A}_3 - \hat{A}_3\hat{B} + \hat{B}_2\hat{A}_1 + \hat{A}_1\hat{B}_2 - \hat{B}_2\hat{A} - \hat{A}\hat{B}_2\right)\Delta t\delta_{\xi\eta\eta}^3 \\
& + \left(\hat{B}_2\hat{B}_3 + \hat{B}_3\hat{B}_2 + \hat{B}_2\hat{A}_3 + \hat{A}_3\hat{B}_2\right)\Delta t\delta_{\xi\eta\eta\eta}^4 \\
& + \left(\hat{B}_3^2 + \hat{A}_3^2 + \hat{A}_2\hat{B}_2 + \hat{B}_2\hat{A}_2 + \hat{A}_3\hat{B}_3 + \hat{B}_3\hat{A}_3\right)\Delta t\delta_{\xi\xi\eta\eta}^4 \\
& + \left(\hat{A}_3\hat{A}_1 + \hat{A}_1\hat{A}_3 - \hat{A}_3\hat{A} - \hat{A}\hat{A}_3 + \hat{A}_1\hat{B}_3 + \hat{B}_3\hat{A}_1 \right.\\
& \left. - \hat{A}\hat{B}_3 - \hat{B}_3\hat{A} + \hat{A}_2\hat{B}_1 + \hat{B}_1\hat{A}_2 - \hat{A}_2\hat{B} - \hat{B}\hat{A}_2\right)\Delta t\delta_{\xi\xi\eta}^3
\end{aligned}
$$

$$+ \left(\hat{A}_2 \hat{A}_3 + \hat{A}_3 \hat{A}_2 + \hat{A}_2 \hat{B}_3 + \hat{B}_3 \hat{A}_2 \right) \Delta t \delta_{\xi\xi\xi\eta}^4$$

$$+ \left(\hat{A}_1 - \hat{A} \right) \delta_\xi + \left[\left(\hat{A}^2 + \hat{A}_1^2 - \hat{A}\hat{A}_1 - \hat{A}_1\hat{A} \right) \Delta t + \hat{A}_2 \right] \delta_\xi^2$$

$$+ \left(\hat{A}_1 \hat{A}_2 + \hat{A}_2 \hat{A}_1 - \hat{A}\hat{A}_2 - \hat{A}_2\hat{A} \right) \Delta t \delta_\xi^3 + \hat{A}_2^2 \Delta t \delta_\xi^4 \Big\} \Big\} U_{j,k}^n$$

$$+ O \left(\Delta t^3, \Delta \xi^2, \Delta \eta^2 \right) \tag{5.35}$$

The above scheme is a second-order accurate representation of

$$U_t + \hat{A} U_\xi + \hat{B} U_\eta - \hat{A}_1 U_\xi - \hat{B}_1 U_\eta - \hat{A}_2 U_{\xi\xi} - \hat{B}_2 U_{\eta\eta} - \left(\hat{A}_3 + \hat{B}_3 \right) U_{\xi\eta}$$

$$= \Delta t \Big[-U_{tt} + \left(\hat{B}^2 + \hat{B}_1^2 - \hat{B}\hat{B}_1 - \hat{B}_1\hat{B} \right) U_{\eta\eta}$$

$$+ \left(\hat{A}_1 \hat{B}_1 + \hat{B}_1 \hat{A}_1 - \hat{A}_1 \hat{B} - \hat{B}\hat{A}_1 - \hat{A}\hat{B}_1 - \hat{B}_1\hat{A} + \hat{A}\hat{B} + \hat{B}\hat{A} \right) U_{\xi\eta}$$

$$+ \left(\hat{B}_1 \hat{B}_2 + \hat{B}_2 \hat{B}_1 - \hat{B}\hat{B}_2 - \hat{B}_2\hat{B} \right) U_{\eta\eta\eta} + \hat{B}_2^2 U_{\eta\eta\eta\eta}$$

$$+ \left(\hat{B}_3 \hat{B}_1 + \hat{B}_1 \hat{B}_3 - \hat{B}_3 \hat{B} - \hat{B}\hat{B}_3 + \hat{B}_1 \hat{A}_3 + \hat{A}_3 \hat{B}_1 \right.$$

$$\left. - \hat{B}\hat{A}_3 - \hat{A}_3\hat{B} + \hat{B}_2 \hat{A}_1 + \hat{A}_1 \hat{B}_2 - \hat{B}_2\hat{A} - \hat{A}\hat{B}_2 \right) U_{\xi\eta\eta}$$

$$+ \left(\hat{B}_2 \hat{B}_3 + \hat{B}_3 \hat{B}_2 + \hat{B}_2 \hat{A}_3 + \hat{A}_3 \hat{B}_2 \right) U_{\xi\eta\eta\eta}$$

$$+ \left(\hat{B}_3^2 + \hat{A}_3^2 + \hat{A}_2 \hat{B}_2 + \hat{B}_2 \hat{A}_2 + \hat{A}_3 \hat{B}_3 + \hat{B}_3 \hat{A}_3 \right) U_{\xi\xi\eta\eta}$$

$$+ \left(\hat{A}_3 \hat{A}_1 + \hat{A}_1 \hat{A}_3 - \hat{A}_3 \hat{A} - \hat{A}\hat{A}_3 + \hat{A}_1 \hat{B}_3 + \hat{B}_3 \hat{A}_1 \right.$$

$$\left. - \hat{A}\hat{B}_3 - \hat{B}_3\hat{A} + \hat{A}_2 \hat{B}_1 + \hat{B}_1 \hat{A}_2 - \hat{A}_2\hat{B} - \hat{B}\hat{A}_2 \right) U_{\xi\xi\eta}$$

$$+ \left(\hat{A}_2 \hat{A}_3 + \hat{A}_3 \hat{A}_2 + \hat{A}_2 \hat{B}_3 + \hat{B}_3 \hat{A}_2 \right) U_{\xi\xi\xi\eta}$$

$$+ \left(\hat{A}^2 + \hat{A}_1^2 - \hat{A}\hat{A}_1 - \hat{A}_1\hat{A} \right) U_{\xi\xi}$$

$$+ \left(\hat{A}_1 \hat{A}_2 + \hat{A}_2 \hat{A}_1 - \hat{A}\hat{A}_2 - \hat{A}_2\hat{A} \right) U_{\xi\xi\xi} + \hat{A}_2^2 U_{\xi\xi\xi\xi} \Big] \tag{5.36}$$

Examination of Eq 5.9 reveals

$$U_{tt} = \left(\hat{B}^2 + \hat{B}_1^2 - \hat{B}\hat{B}_1 - \hat{B}_1\hat{B} \right) U_{\eta\eta}$$

$$+ \left(\hat{A}_1 \hat{B}_1 + \hat{B}_1 \hat{A}_1 - \hat{A}_1 \hat{B} - \hat{B}\hat{A}_1 - \hat{A}\hat{B}_1 - \hat{B}_1\hat{A} + \hat{A}\hat{B} + \hat{B}\hat{A} \right) U_{\xi\eta}$$

$$+ \left(\hat{B}_1 \hat{B}_2 + \hat{B}_2 \hat{B}_1 - \hat{B}\hat{B}_2 - \hat{B}_2\hat{B} \right) U_{\eta\eta\eta} + \hat{B}_2^2 U_{\eta\eta\eta\eta}$$

63

$$+ \left(\hat{B}_3 \hat{B}_1 + \hat{B}_1 \hat{B}_3 - \hat{B}_3 \hat{B} - \hat{B} \hat{B}_3 + \hat{B}_1 \hat{A}_3 + \hat{A}_3 \hat{B}_1 \right.$$
$$\left. - \hat{B} \hat{A}_3 - \hat{A}_3 \hat{B} + \hat{B}_2 \hat{A}_1 + \hat{A}_1 \hat{B}_2 - \hat{B}_2 \hat{A} - \hat{A} \hat{B}_2 \right) U_{\xi \eta \eta}$$
$$+ \left(\hat{B}_2 \hat{B}_3 + \hat{B}_3 \hat{B}_2 + \hat{B}_2 \hat{A}_3 + \hat{A}_3 \hat{B}_2 \right) U_{\xi \eta \eta \eta}$$
$$+ \left(\hat{B}_3^2 + \hat{A}_3^2 + \hat{A}_2 \hat{B}_2 + \hat{B}_2 \hat{A}_2 + \hat{A}_3 \hat{B}_3 + \hat{B}_3 \hat{A}_3 \right) U_{\xi \xi \eta \eta}$$
$$+ \left(\hat{A}_3 \hat{A}_1 + \hat{A}_1 \hat{A}_3 - \hat{A}_3 \hat{A} - \hat{A} \hat{A}_3 + \hat{A}_1 \hat{B}_3 + \hat{B}_3 \hat{A}_1 \right.$$
$$\left. - \hat{A} \hat{B}_3 - \hat{B}_3 \hat{A} + \hat{A}_2 \hat{B}_1 + \hat{B}_1 \hat{A}_2 - \hat{A}_2 \hat{B} - \hat{B} \hat{A}_2 \right) U_{\xi \xi \eta}$$
$$+ \left(\hat{A}_2 \hat{A}_3 + \hat{A}_3 \hat{A}_2 + \hat{A}_2 \hat{B}_3 + \hat{B}_3 \hat{A}_2 \right) U_{\xi \xi \xi \eta}$$
$$+ \left(A^2 + \hat{A}_1^2 - \hat{A} \hat{A}_1 - \hat{A}_1 \hat{A} \right) U_{\xi \xi}$$
$$+ \left(\hat{A}_1 \hat{A}_2 + \hat{A}_2 \hat{A}_1 - \hat{A} \hat{A}_2 - \hat{A}_2 \hat{A} \right) U_{\xi \xi \xi} + \hat{A}_2^2 U_{\xi \xi \xi \xi} \tag{5.37}$$

Upon substitution of Eq 5.37 into Eq 5.36, the right-hand side of Eq 5.36 becomes $O\left[\Delta t^2, \Delta \xi^2, \Delta \eta^2 \right]$ and a second-order accurate algorithm is assured. Thus, the scheme given by Eqs 5.21-5.23, 5.33, and 5.34 is a representation of

$$U_t + \xi_x F_\xi + \eta_x F_\eta + \xi_y G_\xi + \eta_y G_\eta = \xi_x F_{v_\xi} + \eta_x F_{v_\eta} + \xi_y G_{v_\xi} + \eta_y G_{v_\eta}$$
$$+ O\left[\Delta t^2, \Delta \xi^2, \Delta \eta^2 \right] \tag{5.38}$$

This scheme is hereafter referred to as ATNSC2, which is shorthand for 2nd-Order AFIT TVD Navier-Stokes Code. A description of the ATNSC2 routines is contained in Appendix C. Also included is a relative performance evaluation of the routines, obtained using the CRAY FLOWTRACE option.

5.2.3 Beam-Warming Algorithm. The implicit Beam-Warming algorithm as implemented by Visbal [47] is used herein as a comparison against the solutions provided by ATNSC. The scheme solves the strong conservation form of the Navier-Stokes equations. The scheme is written in delta form as

$$\left\{ I + \frac{\theta_1 \Delta t}{1+\theta_2} \left[\frac{\partial \hat{A}}{\partial \xi} - \frac{\partial^2 \hat{A}_v}{\partial \xi^2} \right]^n \right\} \left\{ I + \frac{\theta_1 \Delta t}{1+\theta_2} \left[\frac{\partial \hat{B}}{\partial \eta} - \frac{\partial^2 \hat{B}_v}{\partial \eta^2} \right]^n \right\} \Delta^n \hat{U} =$$
$$- \frac{\Delta t}{1+\theta_2} \left[\frac{\partial}{\partial \xi} \left(\hat{F} - \hat{F}_v \right)^n + \frac{\partial}{\partial \eta} \left(\hat{G} - \hat{G}_v \right)^n \right] + \frac{\theta_1 \Delta t}{1+\theta_2} \left(\frac{\partial}{\partial \xi} \Delta^{n-1} \hat{F}_{v_2} + \frac{\partial}{\partial \eta} \Delta^{n-1} \hat{G}_{v_1} \right) \tag{5.39}$$

where

$$\Delta^n \hat{U} = \hat{U}^{n+1} - \hat{U}^n \tag{5.40}$$

and

$$\hat{F}_v = (\xi_x F_v + \xi_y G_v)/J \qquad \hat{G}_v = (\eta_x F_v + \eta_y G_v)/J$$
$$\hat{A}_v = \partial \hat{F}_v/\partial \hat{U}_\xi \qquad \hat{B}_v = \partial \hat{G}_v/\partial \hat{U}_\eta \tag{5.41}$$

$\hat{F}_{v_2}$ and $\hat{G}_{v_1}$ are evaluated from

$$\hat{F}_v(U, U_\xi, U_\eta) = \hat{F}_{v_1}(U, U_\xi) + \hat{F}_{v_2}(U, U_\eta)$$
$$\hat{G}_v(U, U_\xi, U_\eta) = \hat{G}_{v_1}(U, U_\xi) + \hat{G}_{v_2}(U, U_\eta) \tag{5.42}$$

For steady-state calculations, first-order accurate Euler-implicit time differencing is utilized by setting $\theta_1 = 1$ and $\theta_2 = 0$. Second-order time accuracy is achieved by setting $\theta_1 = 1/2$ and $\theta_2 = 0$ to obtain a trapezoidal time differencing. Trapezoidal differencing is used for all computations where the a time-dependent solution is of interest. Eq 5.39 is implemented using second-order approximations for the spatial derivatives.

To maintain numerical stability and provide smooth solutions, explicit fourth-order damping is added to the right-hand side of Eq 5.39 as

$$-\omega_e^\xi \Delta t J_{i,j}^{-1} \delta_\xi^4 U_{i,j}^n \tag{5.43}$$

and

$$-\omega_e^\eta \Delta t J_{i,j}^{-1} \delta_\eta^4 U_{i,j}^n \tag{5.44}$$

Implicit second-order damping is inserted with respect to the implicit operators as

$$-\omega_i^\xi \Delta t J_{i,j}^{-1} \delta_\xi^2 J_{i,j} I \tag{5.45}$$

and

$$-\omega_i^\eta \Delta t J_{i,j}^{-1} \delta_\eta^2 J_{i,j} I \tag{5.46}$$

In Eqs 5.43 through 5.46, δ_l^k is a second-order accurate, central-difference operator used to approximate the kth derivative with respect to l. The nominal values of the damping coefficients are [27]

$$\begin{aligned} \omega_e^\xi &= 0.02 & \omega_e^\eta &= 0.04 \\ \omega_i^\eta &= 0.25 & \omega_i^\xi &= 0.25 \end{aligned} \qquad (5.47)$$

VI. Viscous Results and Conclusions

6.1 Burgers' Equation

To provide a performance comparison, the Lax-Wendroff and ATNSC schemes are applied to the linearized version of the viscous Burgers' equation

$$u_t + cu_x = \mu u_{xx} \tag{6.1}$$

with periodic boundary conditions

$$u(0,t) = u(2\pi,t) \tag{6.2}$$

and the initial condition

$$u(x,0) = c\sin(kx) \tag{6.3}$$

Eq 6.1 has the time-dependent solution

$$U(x,t) = ce^{-k^2\mu t}\sin[k(x - ct)] \tag{6.4}$$

The equations can be non-dimensionalized using

$$\begin{aligned}
\underline{x} &= kx \\
\underline{u} &= u/c \\
\underline{t} &= tkc
\end{aligned} \tag{6.5}$$

to obtain

$$\begin{aligned}
\underline{u}_{\underline{t}} + \underline{u}_{\underline{x}} &= (1/Re)\underline{u}_{\underline{x}\underline{x}} \\
\underline{u}(\underline{x},0) &= \sin\underline{x} \tag{6.6} \\
\underline{U}(\underline{x},t) &= e^{-(1/Re)\underline{t}}\sin(\underline{x} - \underline{t})
\end{aligned}$$

67

where

$$Re = c/(\mu k) \tag{6.7}$$

Rather than perform a stability analysis for the ATNSC scheme with the viscous term added, the exact stability condition for the Lax-Wendroff method is used [1]. In non-dimensional form this limitation becomes

$$\Delta \underline{t} \leq -(1/Re) + \sqrt{\left[(1/Re)^2 + CFL(\Delta \underline{x})^2\right]} \tag{6.8}$$

Figures 6.1 and 6.2 show the results obtained using first-order time accurate, $\Psi_x^n = (1/Re)\underline{u}_{xx}$, versions of the Lax-Wendroff and ATNSC schemes. This is similar to the method used in the implicit application of TVD algorithms to viscous equations and is utilized herein to demonstrate the necessity for second-order accuracy at low Reynolds numbers.

Solutions are initially computed under a CFL restriction of 0.80 with Re = 10000 using 49 (Case I), 99 (Case II), and 199 (Case III) cells respectively. The solution was carried out to $\underline{t} = 56.665$. Figure 6.3 shows the same schemes under a CFL restriction of 0.95 and Re = 10000 using 49 cells only. The norm given with each plot is defined as

$$\|\underline{u} - \underline{U}\| = \left(\Delta \underline{x} \sum_i |\underline{u} - \underline{U}|^2\right)^{1/2} \tag{6.9}$$

$\underline{U}$ is the exact solution of Eq 6.6 shown as the solid curve in the figures.

Figure 6.1 shows that the Lax-Wendroff scheme exhibits a phase shift for Case I. which diminishes as the number of cells is increased. Given the smooth initial data of Eq 6.6, the overall performance of the Lax-Wendroff scheme is rather good. However. the phase shift associated with the Lax-Wendroff scheme does not appear with the ATNSC schemes.

Figure 6.2 shows the results obtained using the first-order ATNSC scheme. The

majority of the error is concentrated in the areas of rapidly changing gradients. Note, however, that the ATNSC norms are smaller in every case than the Lax-Wendroff norms.

Figure 6.3 shows the effect of increasing the CFL restriction to 0.95 for the two schemes. The increase in the CFL (or Courant) number tends to lessen the phase shift associated with the Lax-Wendroff scheme, while allowing the computed solutions of ATNSC to more closely match the exact solution in the regions of rapidly changing gradients.

Figure 6.4 displays the results of a second-order version of the ATNSC scheme applied to Eq 6.6 at $Re = 10000$. Second-order accuracy is arrived at through the use of

$$\Psi_x^n = (1/Re)u_{xx} - \frac{\Delta t}{Re}u_{xxx} + \frac{1}{Re^2}u_{xxxx} \tag{6.10}$$

which is consistent with Eq 5.31. A CFL restriction of 1 was used with no observed difficulty and the norms were between one and two orders of magnitude lower than either of the first-order schemes.

Results of a more severe test of the first-order version of ATNSC are shown in Figure 6.5. The first-order algorithm was applied to the viscous Burgers' equation with $Re = 100$ and $l = 25$. The lower Reynolds number represents an increase in significance of viscous forces over the previous case. The figure clearly shows the degradation of the solution near the extrema, as well as small oscillations present in the solution. The CFL number had to be reduced as spacing was reduced in order to maintain stability. In fact, the CFL numbers used were apparently on the edge of the stability limit.

Solutions using the second-order accurate version of ATNSC for $Re = 100$ are shown in Figure 6.6. The solution is crisp near the peaks and is free of oscillations. The norms are an order-of-magnitude lower than those of the first-order scheme. Finally, the second-order scheme was utilized with a CFL number of 1 for each cell

69

size. The results, shown in Figure 6.7, are indistinguishable from those of Figure 6.6 except that the increase in CFL number further decreased the norms.

Overall, all the first-order schemes perform rather well for the viscous Burgers' equation with periodic boundary conditions, smooth initial data, and high Reynolds number. However, the Lax-Wendroff solution can be expected to show the same type of oscillations as for Riemann's problem if smooth initial data is not specified. It should also be noted that the first-order TVD scheme performs best when the CFL restriction is as close to 1 as possible.

The situation is not so favorable for the first-order TVD scheme at lower Reynolds number. The first-order scheme exhibits decreased accuracy and severe stability restrictions. Thus the first-order scheme is wholly unsuited to the calculation of unsteady flows at low Reynolds numbers.

The behavior of the second-order TVD scheme is very encouraging. Accuracy is superb and the scheme is very robust where stability is concerned. CFL numbers as high as 1.1, in relation to Eq 6.8, were tested with no instability. The Lax-Wendroff time step limitation given by Eq 6.8 is obviously somewhat over restrictive in this case.
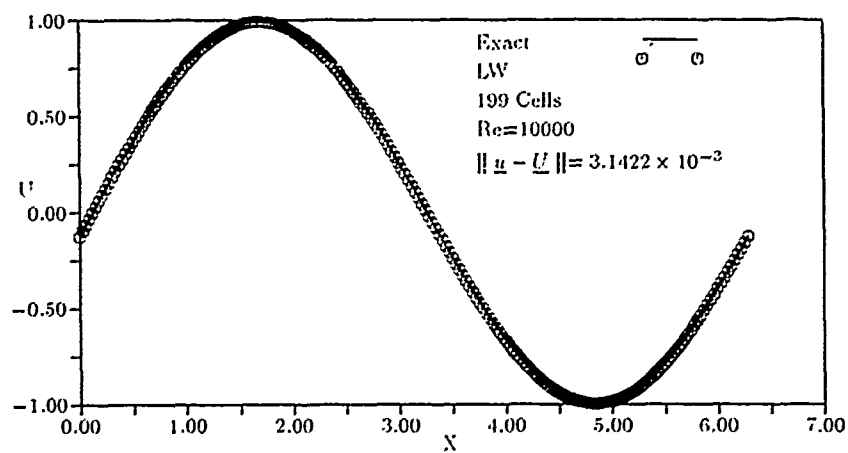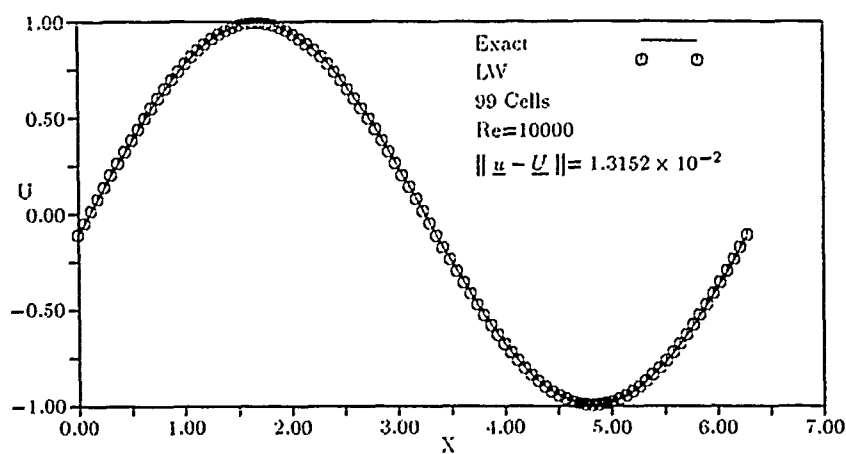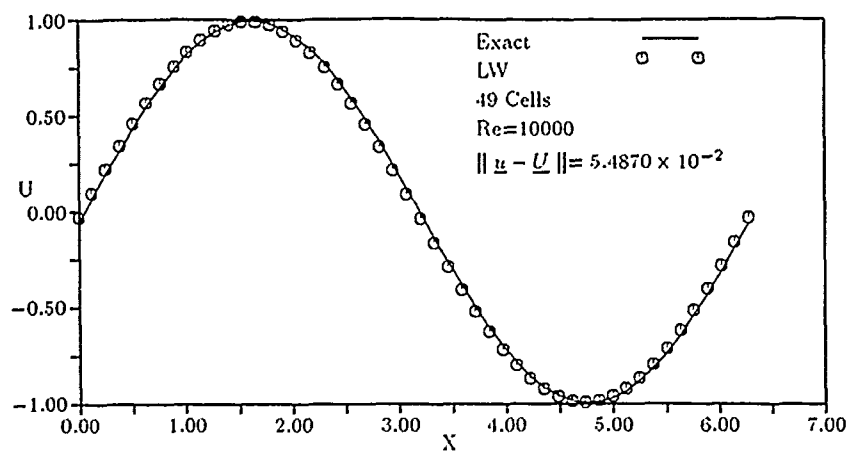
Figure 6.1. 1st-Order Lax-Wendroff Scheme Applied to Viscous Burgers' Equation. CFL=0.8

71
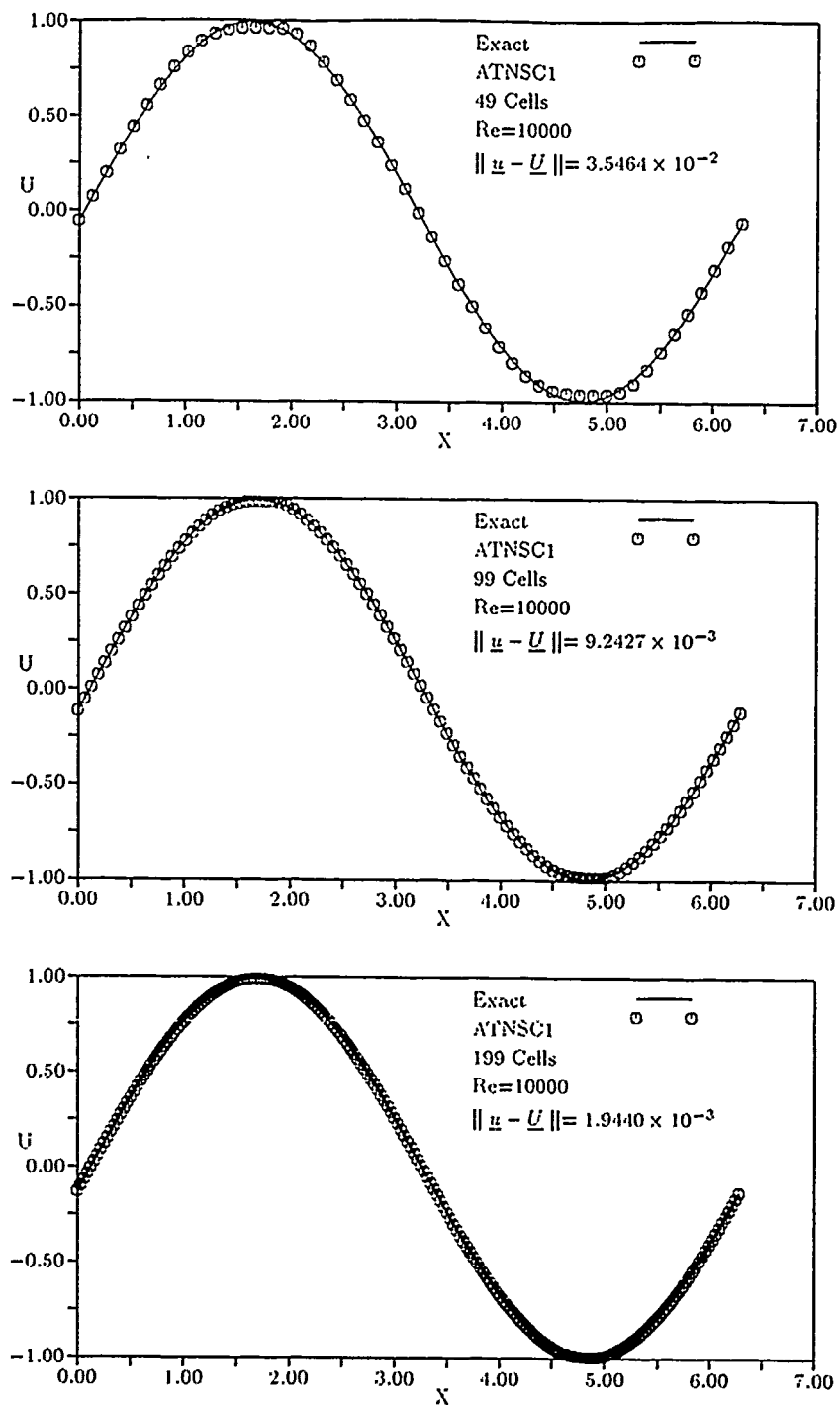
Figure 6.2. 1st-Order ATNSC Scheme Applied to Viscous Burgers' Equation.
CFL=0.8

72
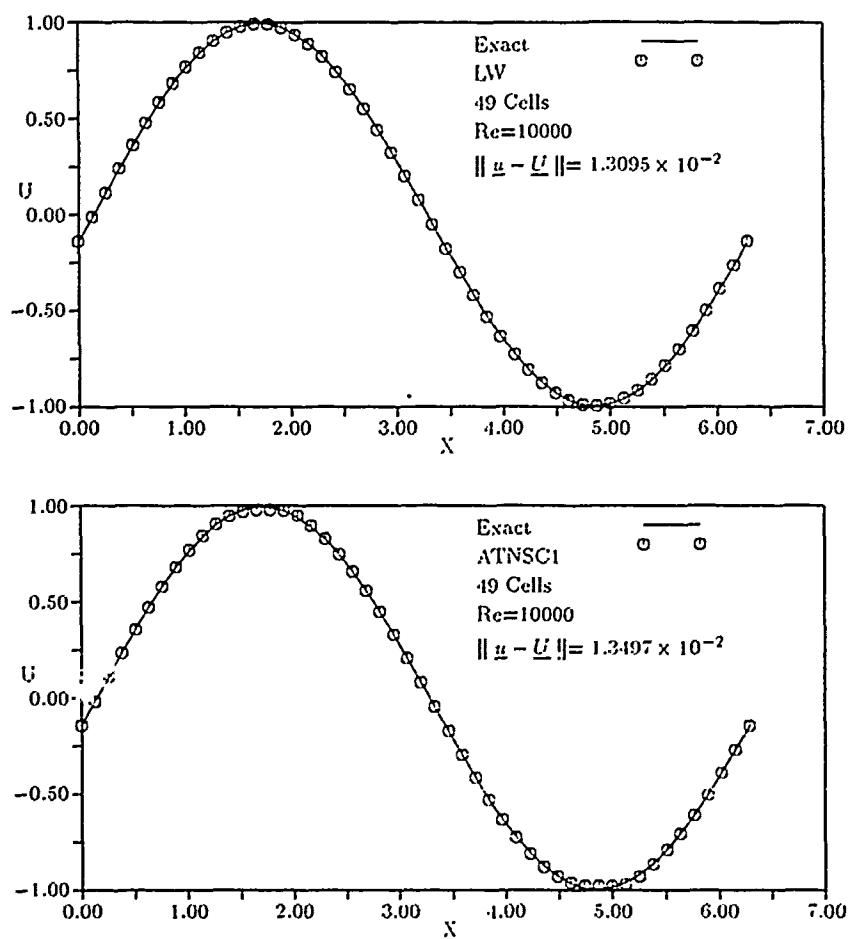
Figure 6.3. 1st-Order Lax-Wendroff and ATNSC Schemes Applied to Viscous Burgers' Equation, CFL=0.95
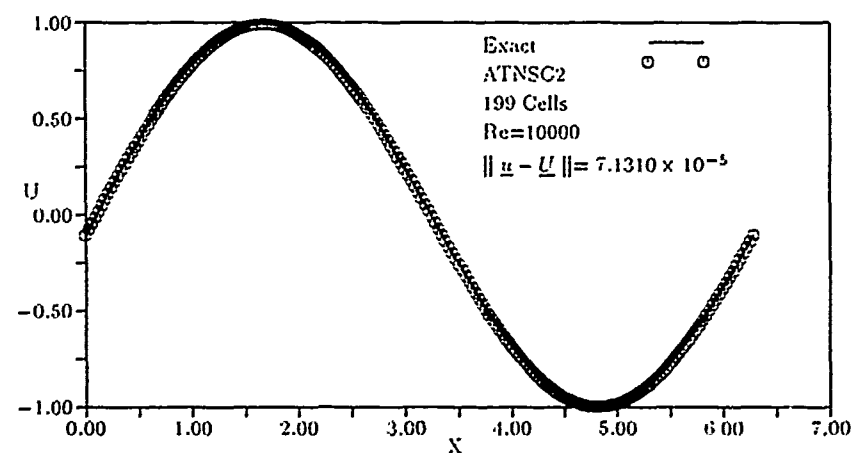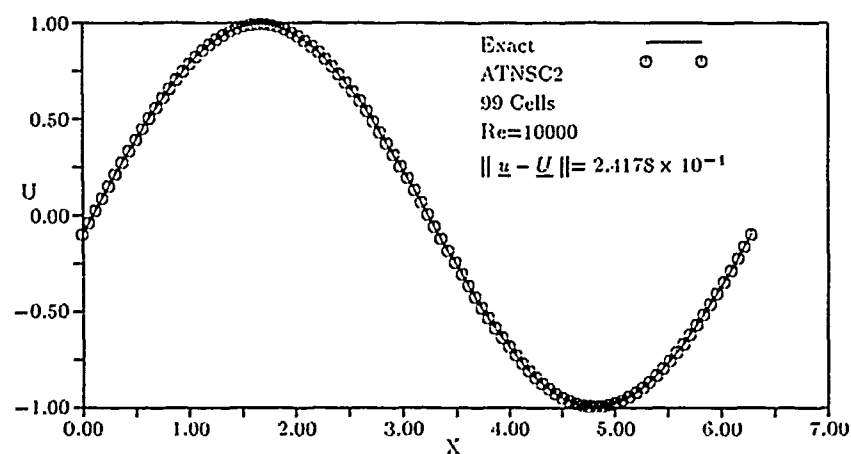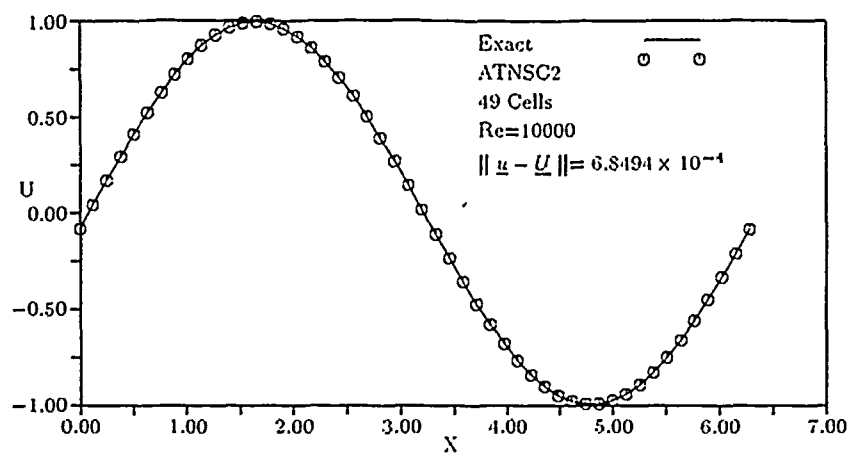
Figure 6.4. 2nd-Order ATNSC Scheme Applied to Viscous Burgers' Equation.
CFL=1.0
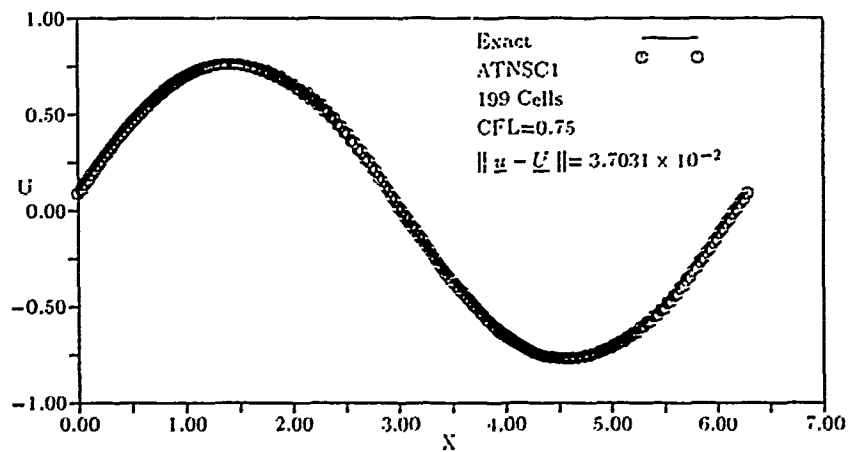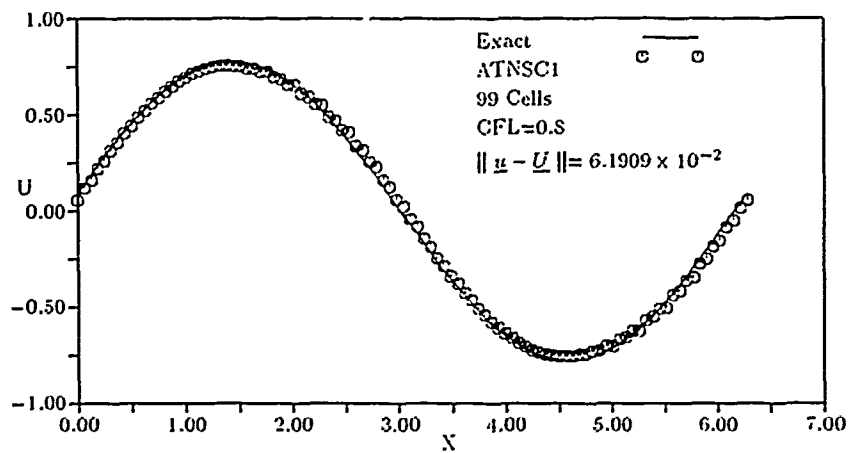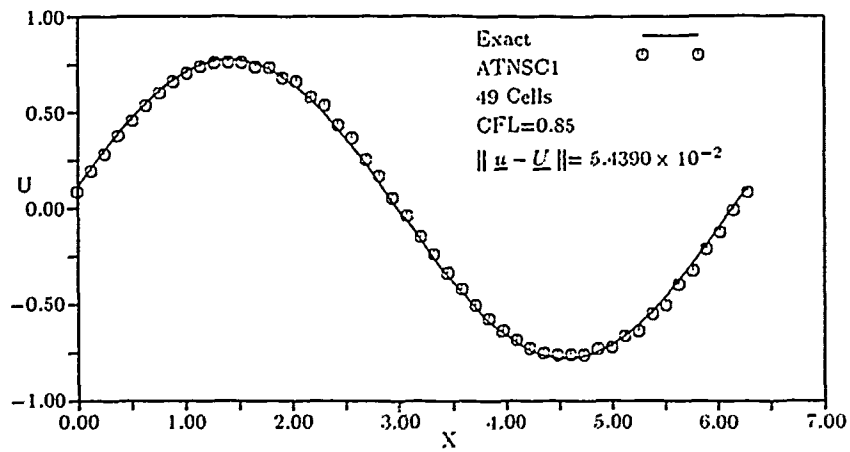
Figure 6.5. 1st-Order ATNSC Scheme Applied to Viscous Burgers' Equation. Re=100
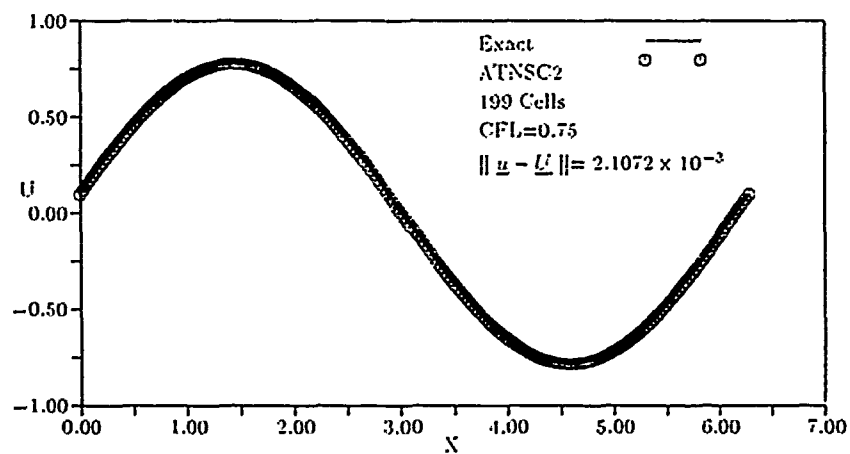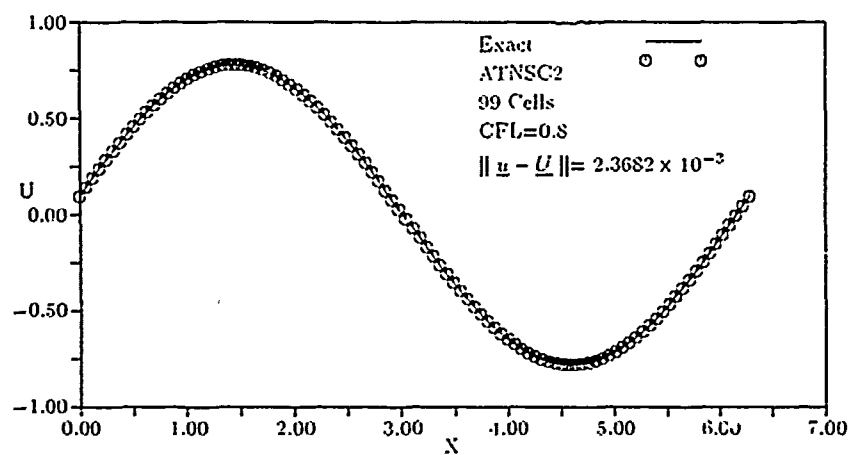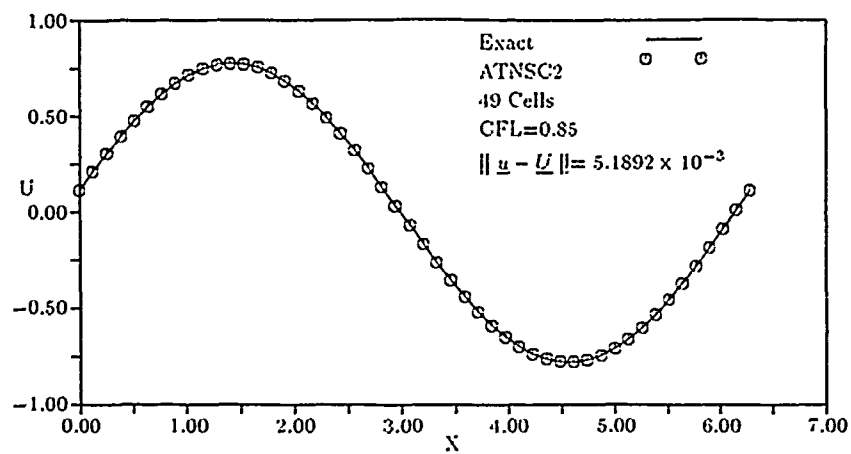
Figure 6.6. 2nd-Order ATNSC Scheme Applied to Viscous Burgers' Equation.
Re=100

76
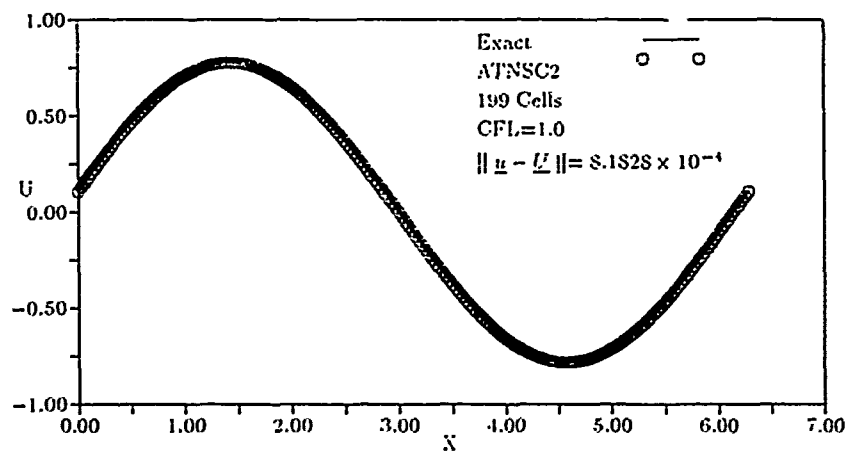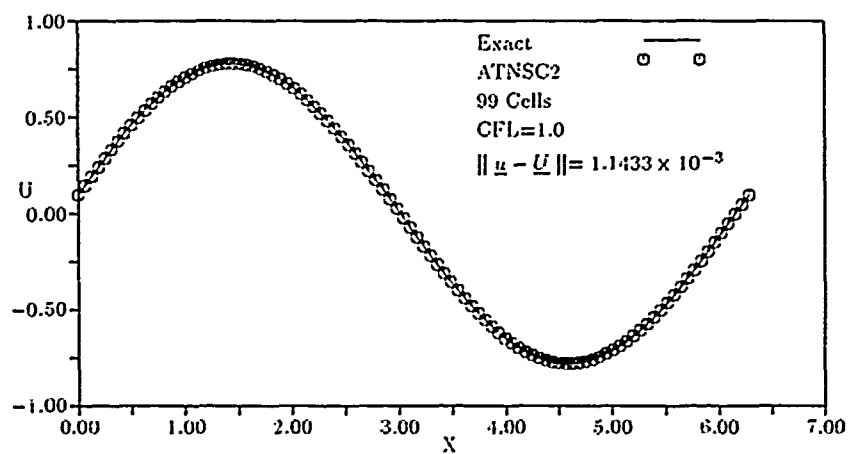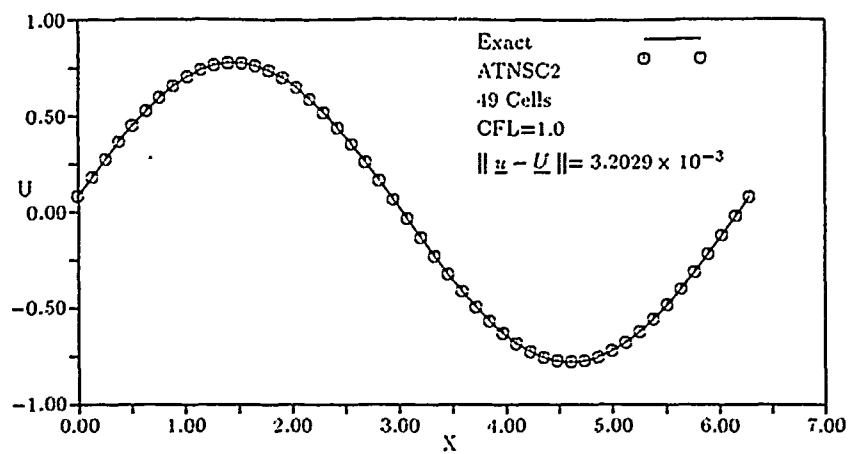
Figure 6.7. 2nd-Order ATNSC Scheme Applied to Viscous Burgers' Equation.
Re=100

6.2 Boundary Conditions for Viscous Flow

Boundary conditions for viscous flows are, in general, more straight forward than their inviscid counterparts described in Section 3.2. At the wall, the inviscid surface tangency condition, Eqs 3.11 and 3.10, is replace by the viscous no-slip requirement:

$$u = 0$$
$$v = 0 \tag{6.11}$$

Simplified wall temperature conitions representing either an adiabatic wall

$$T_{w_n} = 0 \tag{6.12}$$

or constant temperature wall

$$T_w = C \tag{6.13}$$

are used in the current study, depending on the flow of interest. With the wall mapped to a constant η coordinate, the pressure at the wall is obtained by solving the normal-momentum equation:

$$
\begin{aligned}
p_n \sqrt{\eta_x^2 + \eta_y^2} &= (\xi_x \eta_x + \xi_y \eta_y) p_\xi + \left(\eta_x^2 + \eta_y^2\right) p_\eta \\
&= (\xi_y v_\xi + \eta_y v_\eta) \{\eta_x (\xi_x \lambda_\xi + \eta_x \lambda_\eta) \\
&\quad + \eta_y \left[\xi_y (2\mu + \lambda)_\xi + \eta_y (2\mu + \lambda)_\eta\right]\} \\
&\quad + (\xi_y u_\xi + \eta_y u_\eta) \{\eta_x (\xi_y \mu_\xi + \eta_y \mu_\eta) + \eta_y (\xi_x \mu_\xi + \eta_x \mu_\eta)\} \\
&\quad + \mu \eta_x \left(\xi_y^2 u_{\xi\xi} + 2\xi_y \eta_y u_{\xi\eta} + \eta_y^2 u_{\eta\eta}\right) \\
&\quad + (2\mu + \lambda)\eta_y \left(\xi_y^2 v_{\xi\xi} + 2\xi_y \eta_y v_{\xi\eta} + \eta_y^2 v_{\eta\eta}\right)
\end{aligned}
\tag{6.14}
$$

Flow at the inlet and exit of the computational domain is assumed to be inviscid. Inflow and outflow relations from Section 3.2 are thus used to determine flow quantities at these boundaries. As stated in Section 3.2, for supersonic outflow all quantities must be extrapolated from the interior of the domain. In pract ce, this extrapolation is also performed in the subsonic boundary-layer embedded in the

supersonic outflow. For the cases to be considered herein, no adverse effects of this extrapolation are noted.

6.3 Shock-Boundary Layer Interaction

An indepth experiment in laminar shock-boundary-layer interaction was carried out by Hakkinen et al. [18] in 1959 at the Massachusetts Institute of Technology under the sponsorship of the National Advisory Committee for Aeronautics. Detailed measurements were made of pressure distribution, skin friction coefficient, and velocity profiles for a number of combinations of overall pressure ratio, p_f/p_∞, and shock Reynolds number, Re_{x_s}, at a freestream Mach number of 2.0 for a shock wave impinging upon a flat plate boundary-layer. The most recognizable of these in the CFD community is the case of Figure 6b of reference [18]. The overall pressure ratio for this case is 1.40 at a shock Reynolds number of 2.96×10^5, based on $x_s = 4.978\ cm$. It was pointed out by Degrez, Boccadoro, and Wendt [11] that this has been used as a test case by numerous researchers (Skoglund and Gray in 1969; MacCormack in 1971 and 1982; Hanin, Wolfshtein, and Landau in 1974; Beam and Warming in 1978; and Dawes [10] in 1983). Liou also used this as a test case as recently as 1989 [26].

The experimental pressure and skin friction profiles for this case are shown in Figure 6.8, and a sketch of the wave structure is shown in Figure 6.9. The friction coefficient, C_f, is defined as

$$C_f \equiv \frac{\tau_w}{q_\infty} \qquad (6.15)$$

where τ_w is the normal component of shear stress at the wall

$$\tau_w \equiv \mu V'_{t_n} \qquad (6.16)$$

and q_∞ is the dynamic pressure

$$q_\infty = \frac{1}{2}\rho_\infty V_\infty^2 \tag{6.17}$$

With the tangential velocity given by Eq 3.11, and the wall mapped to a $\eta = $ constant coordinate, τ_w can be written as

$$\tau_w = \mu\left(\eta_y u_\eta - \eta_x v_\eta\right) \tag{6.18}$$

No negative values of skin friction are shown because the total-head tube was not able to reliably indicate negative shear values. Locations where the experimental skin friction may have been negative are shown by downward pointing arrows in Figure 6.8. While the accuracy with which the pressure profile can be calculated has greatly improved since MacCormack's calculations [28], there has been essentially no progress in matching the skin friction profile. This includes the overall shape of the profile as well as the location of the separation and reattachment points. MacCormack's calculations failed to show the characteristic plateau in the pressure profile, and, while obtaining a fair prediction of the separation point, he predicted reattachment ahead of the experimental data. In addition, the friction coefficient after reattachment is approximately 20% lower than that suggested by the experimental data. Liou [26] obtained a fair matching to the pressure profile but failed at predicting the skin friction profile in the regions of adverse pressure gradient. In every case known to the author, even those that somehow managed to accurately predict separation and reattachment points, the ultimate skin friction level after reattachment remains 18% − 20% low. Liou goes so far as to state that this discrepancy in the skin friction level may be due to transition of the boundary-layer from laminar to turbulent immediately in the interaction region [26]. This is in direct contrast to the experimental velocity profiles of reference [18] and contrary to the observations of the experimenters [18].
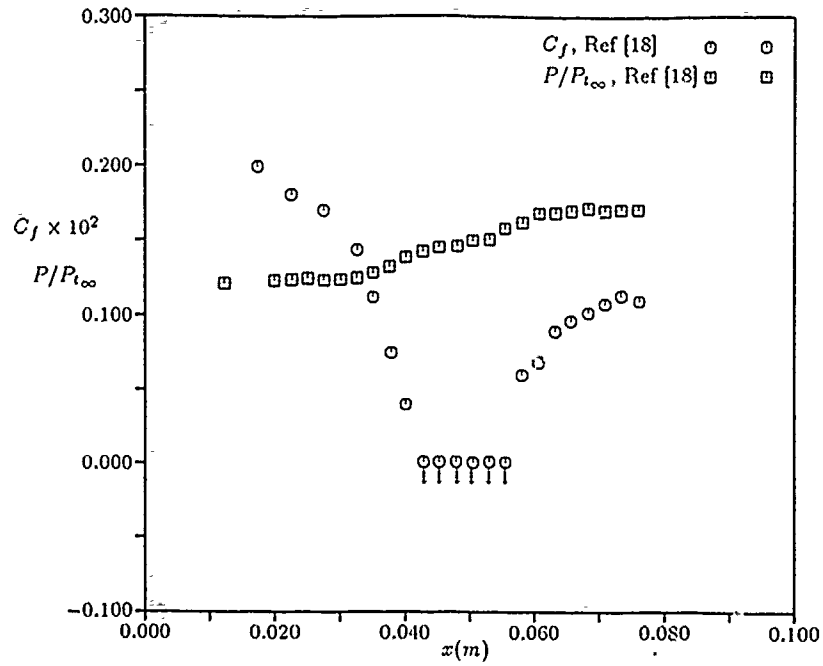
Figure 6.8. Experimental Pressure and Skin Friction Profiles
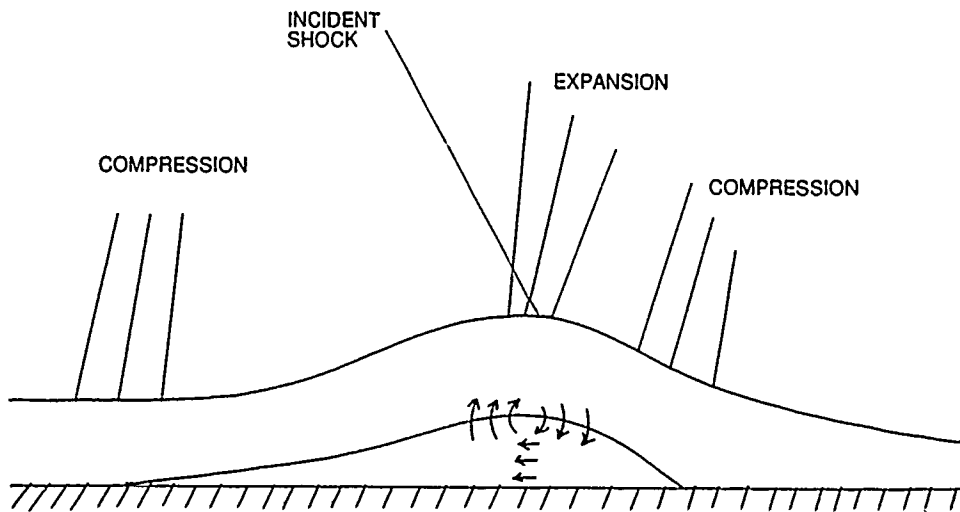
Figure 6.9. Flowfield Structure

81
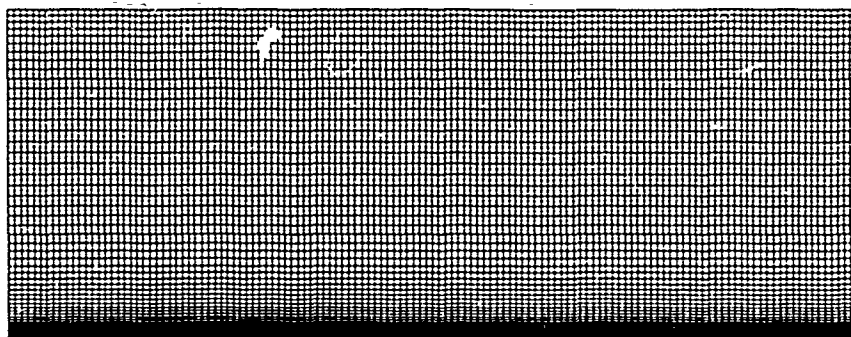
Figure 6.10. Grid Used in Shock-Boundary Layer Interaction Investigations

The grid used for the numerical investigations is shown in Figure 6.10, with 133 points in the axial direction and 60 points in the normal direction. Spacing is held constant in the axial direction at $\Delta x/x_{shock} = 0.013$ and ranges in the normal direction from an initial value at the wall of $\Delta y/x_{shock} = 6.78 \times 10^{-4}$ to a final value of $\Delta y/x_{shock} = 1.12 \times 10^{-2}$ at the upper edge. Grid densities are chosen comparable to those used by MacCormack [28], Dawes [10], and Liou [26] to provide a comparison based on similar grids.

6.3.1   ATNSC Solutions. The computational domain is initialized at the uniform freestream conditions to the left of the point along the upper boundary at which the shock is generated. Post-shock conditions are applied downstream of this point. An adiabatic wall condition is used to obtain the wall temperature along the plate and the nomal momentum equation is solved to obtain the wall pressure in combination with the no-slip velocity constraint at the wall.

Figures 6.11-6.22 show the results of applying the ATNSC algorithms to this test case. The data represented by the figures can be taken to be the solution pro-

vided by either ATNSC1 or ATNSC2, since at this Reynolds number both algorithms provided exactly the same results.

Figures 6.11 and 6.12 depict the solution obtained with $\epsilon = 0$ in the nonlinear fields and $\epsilon = 0.05$ in the linearly degenerate fields. Note that this is in contrast to the values of $\epsilon = O[0.1]$ for the nonlinear fields and $\epsilon = 0$ for the linearly degenerate fields typically utilized for the inviscid calculations of Part I. Values of ϵ up to 0.025 for the nonlinear fields were found to have no noticeable effect on the solution while the ϵ value used in the linearly degenerate fields significantly alter the solution, as will shortly become apparent. The pressure profile of Figure 6.11 clearly shows the pressure rise to separation, the constant pressure plateau within the separated region, and the pressure rise to reattachment as described in reference [18]. The most noticeable aspect of the pressure profile is the slightly lower value, as compared to the experimental data, within the separation region. The reason for this is unknown, although the trend was consistent throughout the invesigation. The skin friction profile of Figure 6.11 contains several regions of interest. First, there is a very slight oscillation in the friction coefficient leading up to the sharp drop just prior to separation. This was observed for values of $\epsilon_{2,4} > 0.025$, and in fact, skin friction was severly oscillatory at $\epsilon_{2,4} = O[0.1]$ which are not unusual values when $\epsilon_{2,4} \neq 0$ for inviscid calculations. The length of the separation region was underpredicted in that delayed separation and premature reattachment were observed. This again appears to be an artifact of the values of $\epsilon_{2,4}$ used, as will become apparent upon examination of subsequent figures. The skin friction profile beyond reattachment shows a rapid rise to the ultimate value, although the ultimate value shows much better agreement with the experimental data than that obtained through previous investigations known to the author. Figure 6.12 provides a visualization of the wave structure through 50 equally spaced pressure contours between the upstream and downstream pressures. The ATNSC algorithm provides high-resolution capturing of all the pertinent flow structures. These include the gen-

erated shock, the leading-edge shock and accompanying expasion, separation shock, expansion fan, and reattachment shock.

The values of $\epsilon_{2,4}$ were lowered to 0.025 for the solution depicted in Figures 6.13 and 6.14. The pressure profile of Figure 6.13 is identical to that of Figure 6.11 except for the extension of the constant pressure plateau slightly upstream and downstream. This is due to the increase in the length of the separation region apparent upon comparison of Figures 6.11 and 6.13. Calculated separation and reattachment points agree extremely well with the experimental data. Note also that there is no longer any oscillation in the friction coefficient in the upstream region and that the rise to the ultimate downstream friction value is more gradual. This is the first numerical solution known to the author that correctly predicts the separation and reattachment points as well as the correct downstream friction coefficient. Computed pressure contours for this particular case are presented in Figure 6.14. Wave structure is very similar to that of Figure 6.12 except for the enhanced structure in the interaction region, due to the lengthening of the separation region. A lengthed separation region also provides enhanced resolution of the expansion fan in that it is not so tightly packed between the shocks.

Values of ϵ necessary to produce an acceptable solution are, as alluded to previously, an order of magnitude smaller than the values that are often used for inviscid flow. Since the vast majority of viscous TVD research has been conducted for hypersonic flows, an answer was sought in the appropriate literature. Examination of references [24],[32], and [34] revealed that values of $0.05 \leq \epsilon \leq 0.25$ were commonly used for hypersonic flows in the range $4 \leq M_\infty \leq 25$ with ϵ as high as 0.5 in some instances. However, it was discovered that these researchers were using variable isotropic damping attributed to Yee [15] and anisotropic damping due to Martinelli [29]. In the normal direction, isotropic damping is applied to the nonlinear fields as

$$\epsilon^n = \epsilon \Delta t \left[|u \cdot \nabla \xi| + |u \cdot \nabla \eta| + \frac{c}{2}(k_\xi + k_\eta) \right] \qquad (6.19)$$

Figure 6.11. Pressure and Skin Friction Profiles ($\epsilon_1 = \epsilon_3 = 0, \epsilon_2 = \epsilon_4 = 0.05$)

Figure 6.12. Pressure Contours ($\epsilon_1 = \epsilon_3 = 0, \epsilon_2 = \epsilon_4 = 0.05$)

Figure 6.13. Pressure and Skin Friction Profiles ($\epsilon_1 = \epsilon_3 = 0$; $\epsilon_2 = \epsilon_4 = 0.025$)
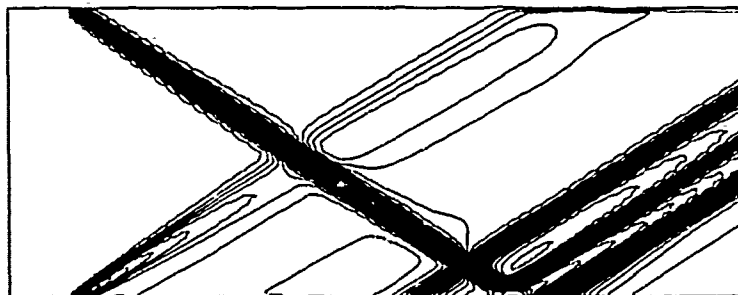
Figure 6.14. Pressure Contours ($\epsilon_1 = \epsilon_3 = 0$; $\epsilon_2 = \epsilon_4 = 0.025$)

and in the axial direction, anisotropic damping is applied to all fields as

$$\epsilon^\xi = \epsilon \Delta t \lambda^{(\xi)} \left[1 + \left(\frac{\lambda^{(\eta)}}{\lambda^{(\xi)}} \right)^{2/3} \right] \tag{6.20}$$

where $\lambda^{(k)} = |u \cdot \nabla k| + c |\nabla k|$.

These changes were incorporated into a version of the ATNSC code and a solution calculated again using $c = 0.0$ in the nonlinear fields and $\epsilon = 0.05$ in the linearly degenerate fields. This particular solution is depicted in Figures 6.15 and 6.16. Figure 6.15 shows that this solution is identical to that of Figure 6.11 except for a small change in the skin friction profile near the minimum value. Examination of Figure 6.16 reveals a sharper resolution of the wave structure than Figure 6.12, more in line with the structure of Figure 6.14.

Lowering the value of ϵ in the linearly degenerate fields to 0.025 resulted in the solution of Figures 6.17 and 6.18. At this lower value of c, the profiles and contours of Figures 6.17 and 6.18 appear identical to those of the constant damping case, Figures 6.13 and 6.14.

Based on this set of solutions, it appears that the change in skin friction profiles and wave structure with c is not a strong function of variable versus constant damping. Research was then conducted into whether anyone had observed the same phenomenon in a similar flow regime. Seider and Hänel [39] have recently observed similar phenomenon in regards to transonic airfoil drag prediction. They simulated the transonic flow about a RAE 2822 airfoil ($M_\infty = 0.73$, $\alpha = 2.79°$) using several TVD schemes applied to the thin layer Navier-Stokes equations, including a scheme based on Roe's approximate Riemann solver. They found that the Roe based scheme provided the best overall results, but that a certain sensitivity to the values of ϵ for the linearly degenerate fields existed for all their schemes. They used values of $c = 0$, 0.1, and 0.2 and found that $c = 0.2$ resulted in a 4% decrease in drag, while leaving lift unchanged. This is consistent with the changes in skin friction while pressure
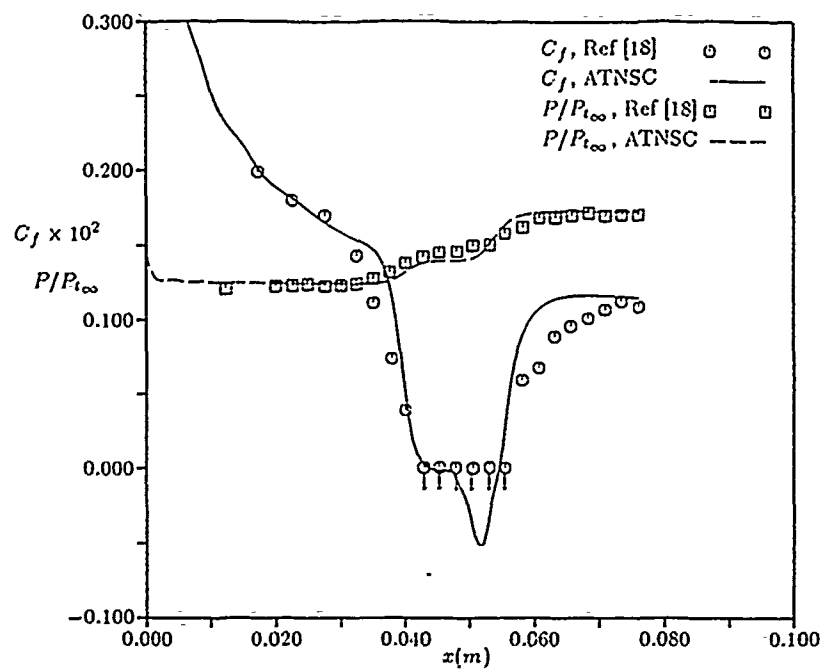
Figure 6.15. Pressure and Skin Friction Profiles ($\epsilon_1 = \epsilon_3 = 0, \epsilon_2 = \epsilon_4 = 0.05$)
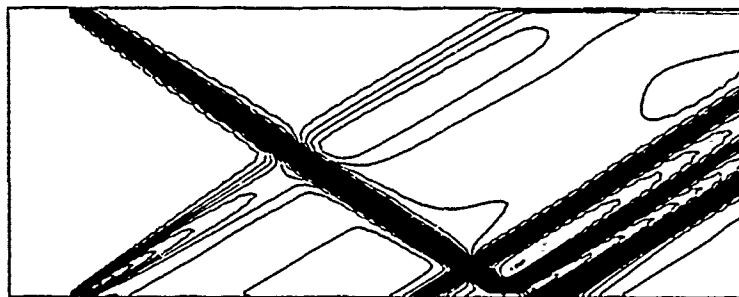
Figure 6.16. Pressure Contours ($\epsilon_1 = \epsilon_3 = 0, \epsilon_2 = \epsilon_4 = 0.05$)
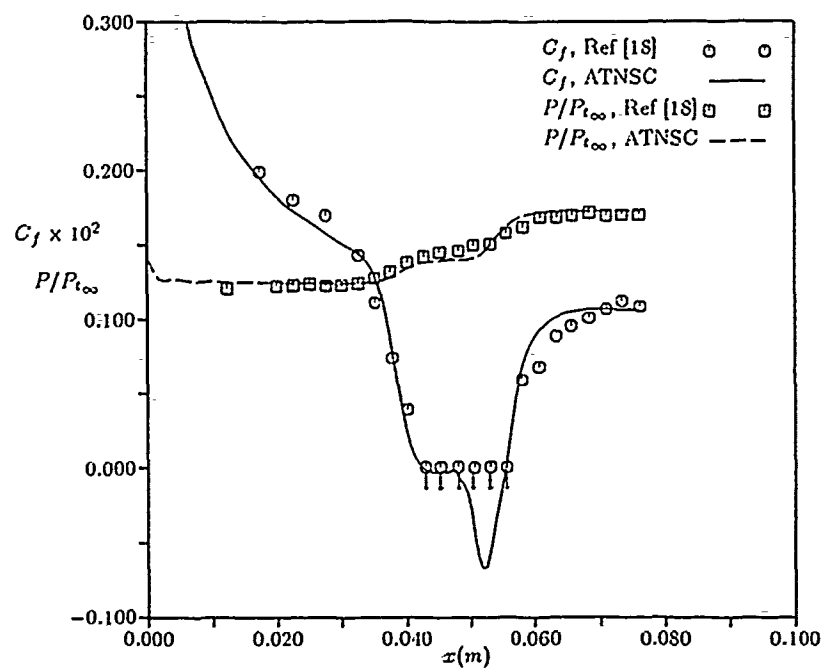
Figure 6.17. Pressure and Skin Friction Profiles ($\epsilon_1 = \epsilon_3 = 0, \epsilon_2 = \epsilon_4 = 0.025$)
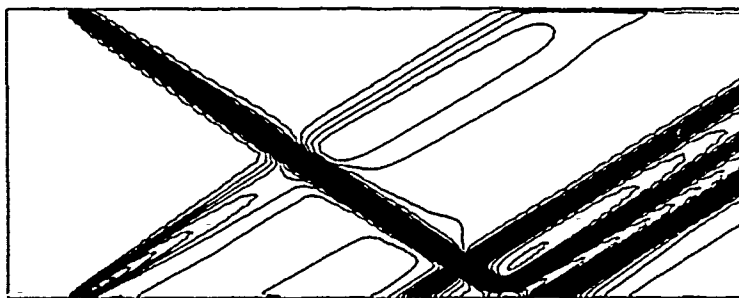
Figure 6.18. Pressure Contours ($\epsilon_1 = \epsilon_3 = 0, \epsilon_2 = \epsilon_4 = 0.025$)

remains constant as seen herein. They then examined a flat plate at $M_\infty = 0.5$ and $Re_l = 5000$ and found that skin friction in this case increased with increasing ϵ. Finally, they doubled the number of grid points in the boundary-layer, from 7 to 14, and found that this totally removed the ϵ dependence. It appears that this behavior is common to flows in the transonic and low supersonic regimes and the effect of ϵ must be analyzed whenever a solution is computed at these Mach numbers.

Three final solutions using ATNSC are presented showing the above mentioned behavior. First, the variable damping algorithm is used to arrive at the solution of Figures 6.19 and 6.20 using $\epsilon = 0.025$ for all fields. This solution is identical to that of Figures 6.13 and 6.14, thus supporting the assertion that the value of ϵ in the linearly degenerate fields is the primary influence. Halving ϵ led to the computed solution shown in Figures 6.21 and 6.22. Again, the pressure profile remains essentially the same as all other cases, but the skin friction levels have decreased slightly, resulting in premature separation and delayed reattachment. Finally, the number of grid points in the boundary-layer was doubled, from 10 to 20. Solutions are presented in Figure 6.23 for ϵ values of 0.0125, 0.025, and 0.035 using this new grid. The pressure profile remains unchanged except for a decrease in the length of the pressure plateau. Skin friction changes only slightly upstream of the interaction region, but drops to zero more rapidly than is the case in Figure 6.13. Separation and reattachment points are correctly predicted, and the rise to the final skin friction level more closely follows the experimental data than that of the previous solutions. The ϵ dependence has been removed, within the range $0.0125 \leq \epsilon \leq 0.035$, consistent with the observartions of Seider and Hänel [39].

6.3.2 Beam-Warming Solutions. The approximate-factorization algorithm of Beam and Warming, Eq 5.39 as implemented by Visbal [47], is applied to this test case as a comparison against the ATNSC algorithm. Figures 6.24 and 6.25 depict the Beam-Warming solutions using the nominal recommended value of the second and fourth-order damping coefficients [27]. A value of 0.25 is used for the second-order

90
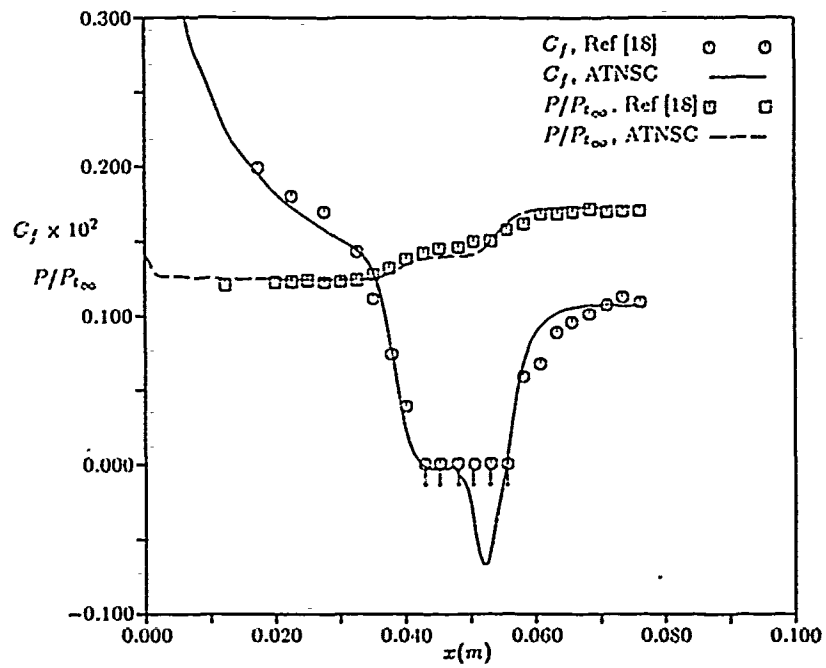
Figure 6.19. Pressure and Skin Friction Profiles ($\epsilon_1 = \epsilon_2 = \epsilon_3 = \epsilon_4 = 0.025$)
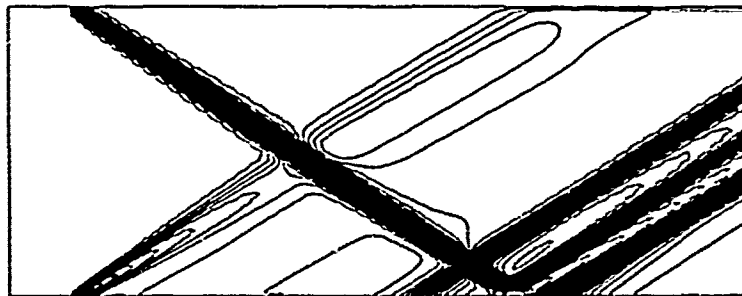
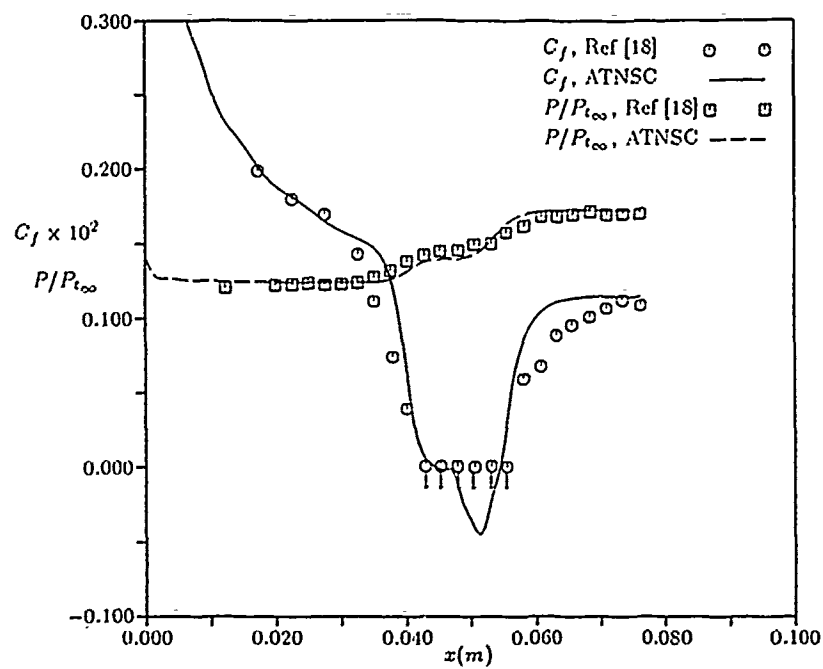Figure 6.20. Pressure Contours ($\epsilon_1 = \epsilon_2 = \epsilon_3 = \epsilon_4 = 0.025$)

91
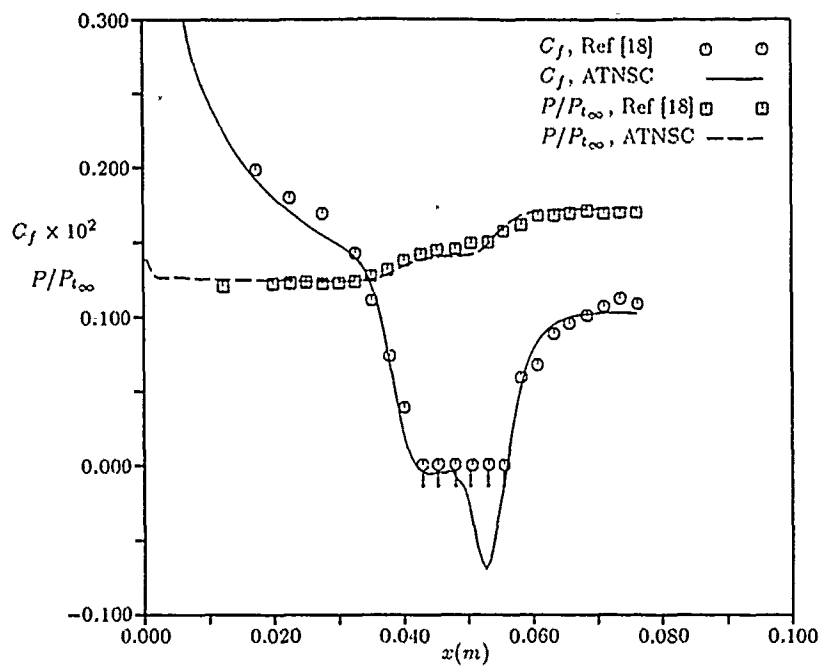
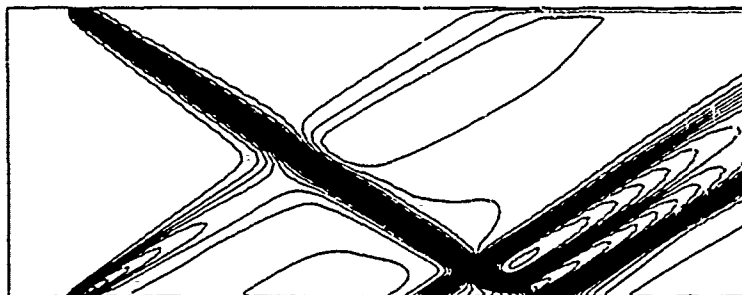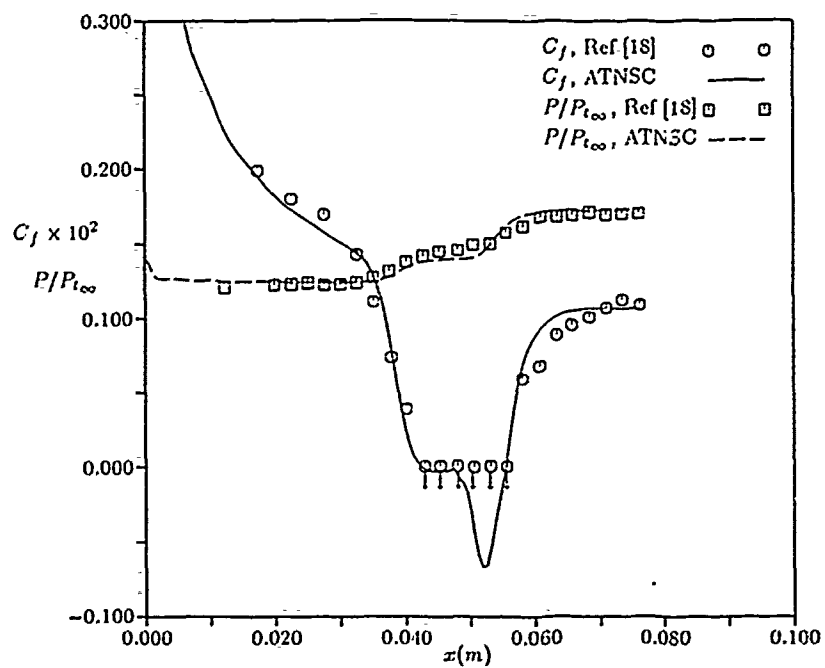Figure 6.21. Pressure and Skin Friction Profiles ($\epsilon_1 = \epsilon_2 = \epsilon_3 = \epsilon_4 = 0.0125$)
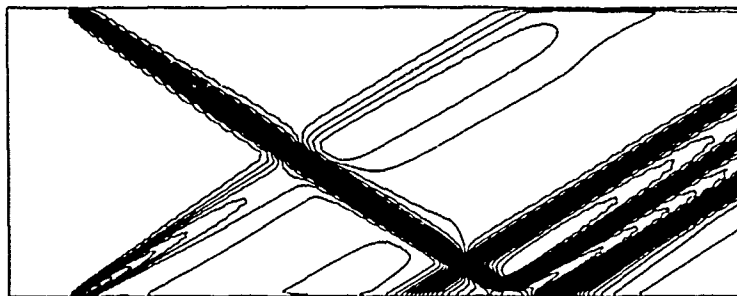
Figure 6.22. Pressure Contours ($\epsilon_1 = \epsilon_2 = \epsilon_3 = \epsilon_4 = 0.0125$)

92
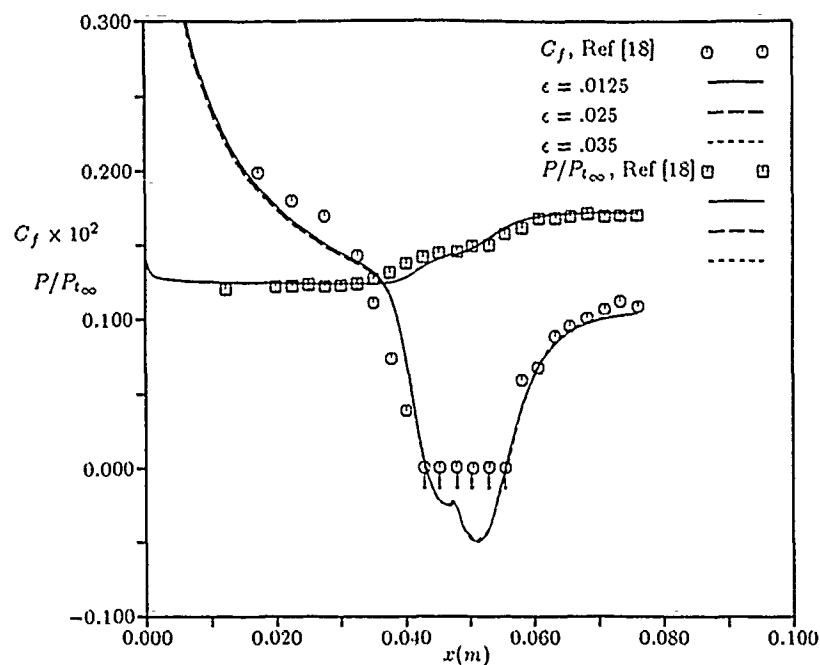
Figure 6.23. Pressure and Skin Friction Profiles (20 Points in the Boundary-Layer)

coefficients in both the axial and normal directions while a value of 0.02 is used for the fourth-order coefficient in the axial direction and 0.04 for the normal direction. The pressure profile of Figure 6.24 is very similar to the ATNSC profiles except for a slightly shortened length of the pressure plateau in the separation region. The skin friction profile is similar to the profiles appearing in the literature for various algorithms applied to this problem. Beam-Warning predicts early separation while the reattachment point is in good agreement with the experimental data. Most noticeable is the under-prediction of the skin friction level beyond reattachment, approximately 15% below the experimental value. Figure 6.25 depicts a significant decrease in resolution of the wave structure as compared to the ATNSC solutions. Shock waves, compression waves, and expansion waves are all smeared to a much greater extent than those obtained with TVD.

Figures 6.26 and 6.27 show the solution computed when the damping coefficients were double those of the previous solution. The pressure profile shows a further
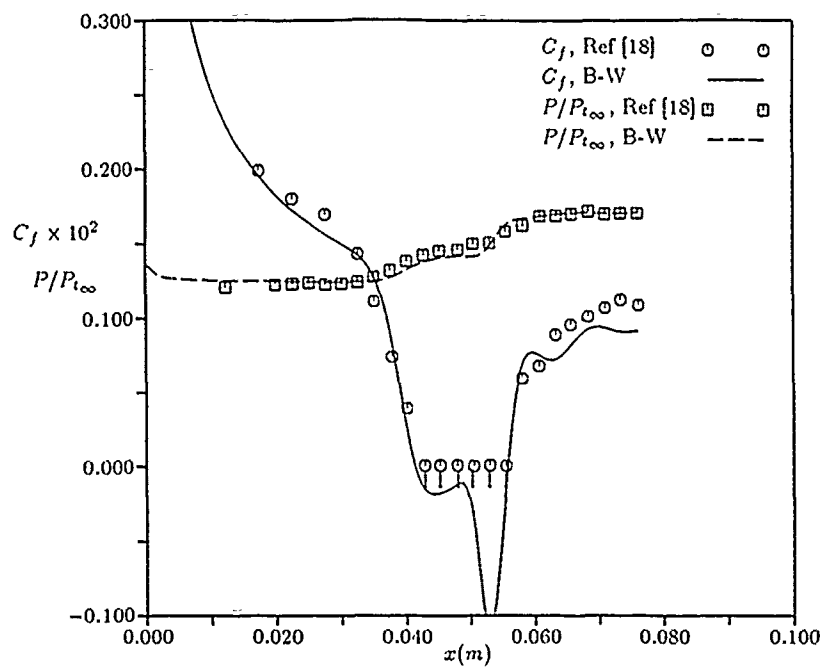
Figure 6.24. Pressure and Skin Friction Profiles
$(\omega_c^\xi = 0.02, \omega_c^\eta = 0.04, \omega_i^\xi = \omega_i^\eta = 0.25)$
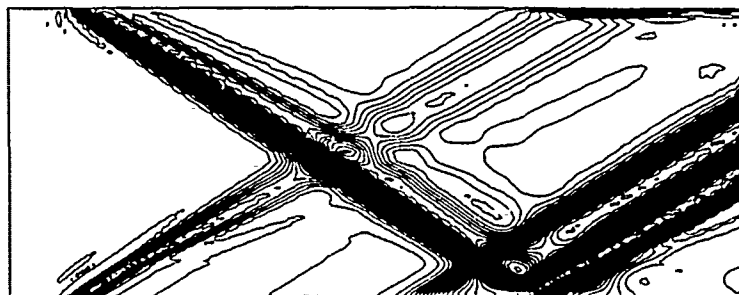
Figure 6.25. Pressure Contours $(\omega_c^\xi = 0.02, \omega_c^\eta = 0.04, \omega_i^\xi = \omega_i^\eta = 0.25)$

reduction in the length of the plateau within the separation region. Predicted separation and reattachment points are in good agreement with the experimental data, while the ultimate friction level is still below that of experiment. There is no oscillation of the skin friction profile in this highly damped case. The pressure contours of Figure 6.27 are more highly smeared than those of Figure 6.25, but the increased damping results in a reduction of the oscillatory effects upstream and downstream of the shocks, compressions, and expansions.

Finally, Figures 6.28 and 6.29 depict a solution using half the damping values of Figures 6.24 and 6.25. The profiles of Figure 6.28 show that the pressure plateau in the separation region has lengthened over that of Figure 6.26, more in line with Figure 6.24, but still is less in extent that that of the ATNSC solutions. Again, early separation is evident but reattachment is in line with the experimental data. Oscillations in the friction profile downstream of reattachment have reappeared, and the ultimate skin friction remains approximately 15% below the experimental value. Wave structure, Figure 6.29, is much less smeared than in Figure 6.27, but shows the same oscillatory effects as Figure 6.25.

The solutions obained using the ATNSC TVD algorithm clearly demonstrate that it is possible to obtain very accurate estimations of separation and reattachment points while at the same time maintaining high degrees of resolution of the wave structure. The Beam-Warming solutions are consistent with those in the literature for numerous algorithms. Only the TVD based ATNSC algorithm incorporates the necessary physical constraints to achieve high accuracy and resolution.

ATNSC solutions are obtained using a constant CFL number of 0.95, under the time step restriction of Eq 1.28. The solution is monitored until no change is observed in the skin friction profile, typically requiring 4000 time steps to achieve steady-state convergence. The data processing rate for ATNSC1 with constant damping is 1.6071×10^{-5} seconds per grid point per time level for the CRAY X-MP/216. Data processing rates for the other ATNSC versions are contained in Appendix C. Beam-

95
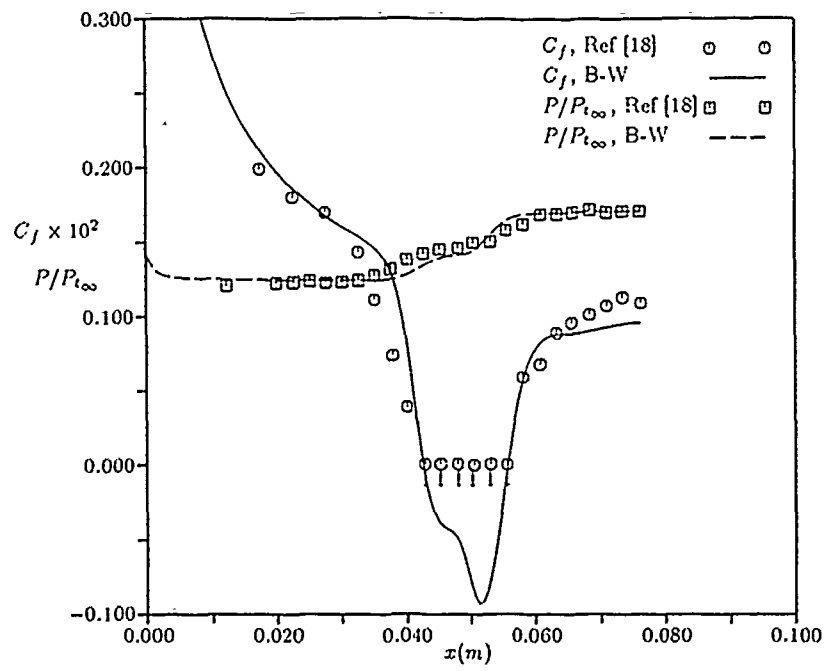
Figure 6.26. Pressure and Skin Friction Profiles
$(\omega_e^\xi = 0.04, \omega_e^\eta = 0.08, \omega_i^\xi = \omega_i^\eta = 0.50)$
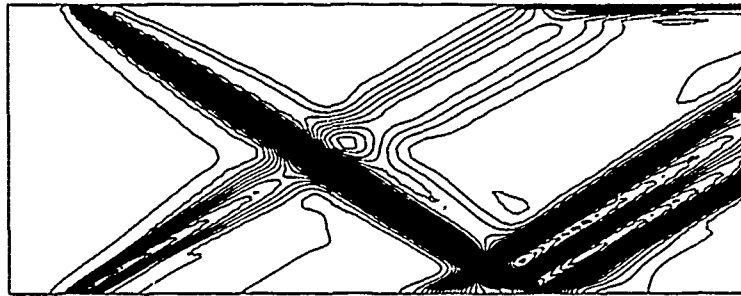
Figure 6.27. Pressure Contours $(\omega_e^\xi = 0.04, \omega_e^\eta = 0.08, \omega_i^\xi = \omega_i^\eta = 0.50)$

96
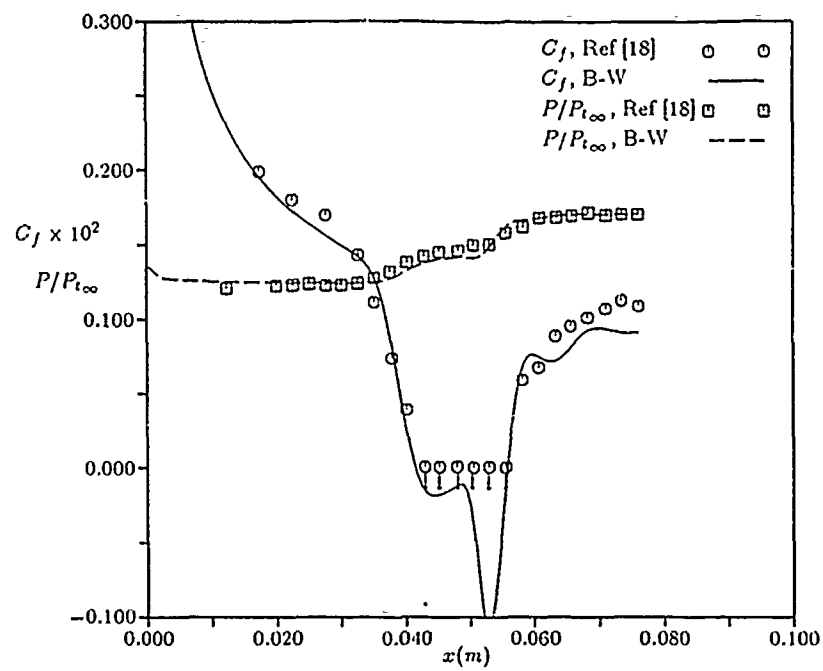
Figure 6.28. Pressure and Skin Friction Profiles
$(\omega_c^\xi = 0.01, \omega_c^\eta = 0.02, \omega_i^\xi = \omega_i^\eta = 0.125)$
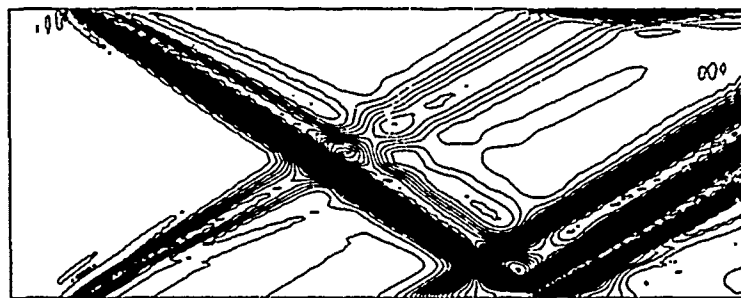
Figure 6.29. Pressure Contours $(\omega_c^\xi = 0.01. \omega_c^\eta = 0.02, \omega_i^\xi = \omega_i^\eta = 0.125)$

Warming solutions are obtained using a CFL number of 5.0, again monitoring until no change is observed in the skin friction profile. This typically requires 1000 iterations for Beam-Warming to achieve steady-state convergence. The Beam-Warming data processing rate is 1.9316×10^{-5} seconds per grid point per iteration for the CRAY X-MP/216.

6.4 Unsteady Shock-Induced Heat Transfer

6.4.1 Heat Transfer Theory of Mirels.

The numerical solutions to the unsteady, shock-induced heat transfer problem are compared herein against the theory of Mirels [30, 31] as implemented by Schlichting [37]. The heat flux at the wall can be written as

$$q = h_x \left(T_{aw} - T_w \right) \qquad (6.21)$$

where the adiabatic wall temperature, T_{aw}, is given by

$$T_{aw} = T_\infty \left(1 + r \frac{\gamma - 1}{2} M_\infty^2 \right) \qquad (6.22)$$

and the local convective heat transfer coefficient, h, is defined as

$$h_x = \frac{Nu_x k}{U_\infty l} \qquad (6.23)$$

For the laminar flow of a perfect gas with weak shocks, Mirels provides the following approximation for the recovery factor, r

$$r = Pr^a \qquad (6.24)$$

where

$$a = 0.39 - \frac{0.02}{1 - U_\infty / U_s} \qquad (6.25)$$

98

and U_s is the shock propagation speed. The local Nusselt number for an unsteady flow is defined as

$$Nu_x = 0.5 C_f Re\, Pr^\lambda \qquad (6.26)$$

where C_f is the local skin friction coefficient

$$C_f = \frac{1.128}{\sqrt{Re}} \left(1 - 0.346 \frac{U_\infty}{U_s}\right)^{1/2} \qquad (6.27)$$

Re is the Reynolds number

$$Re = \frac{\rho_w U_\infty^2 l}{\mu_w} \qquad (6.28)$$

and the subscript w refers to properties evaluated at the wall temperature. Time in Eqs 6.23 and 6.28 is referenced to the time of shock passage. Finally, the exponent of the Prandtl number in Eq 6.26 is

$$\lambda = 0.35 + \frac{0.15}{1 - U_\infty/U_s} \qquad (6.29)$$

The above relations are used to calculate the theoretical heat flux at the plate wall.

6.4.2 Numerical Heat Transfer Solutions.

The final test case for the ATNSC algorithm is the prediction of unsteady, laminar heat transfer due to a shock wave moving down a flat plate. The origin of this test case is the work of Smith [41] who used a shock tube to study the heat transfer to a sharp-edged flat plate, creating ratios of gas temperature to surface temperature typical of those in gas turbine engines. A schematic of Smith's experimental appartus is shown in Figure 6.30.

The case under consideration here is representative of data set A of Smith [41]. The governing parameters are the shock Mach number (M_s), pressure in the driven section (P_1), and temperature in the driven section (T_1). The wall temperature on the flat plate is held constant in the calculations at T_1. Using $M_s = 1.095$, $P_1 = 49102.800\ N/m^2$, and $T_1 = 297.128\ K$ results in a shock pressure ratio of 1.232.
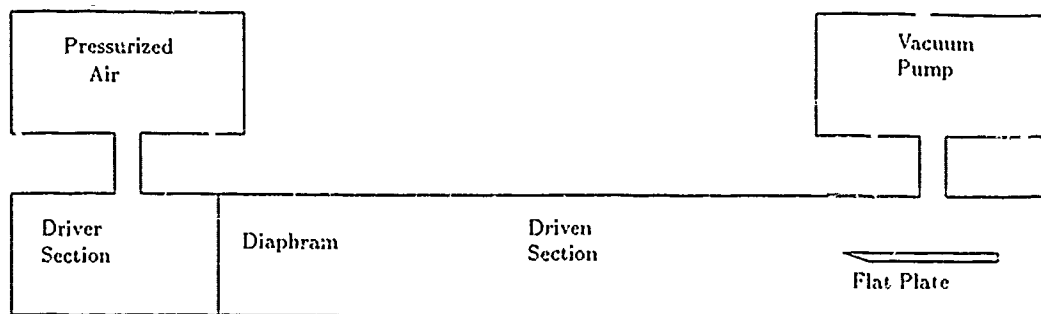
Figure 6.30. Flat Plate Mounted in Shock Tube

a temperature ratio of 1.062, a steady velocity behind the shock of 52.368 m/s, a steady Mach number behind the shock of 0.147, and a steady Reynolds number behind the shock of 92482. Shock Mach number, driven section pressure, and driven section temperature are consistent with data set A of reference [41]. Experimental measurements of the shock Mach number are only accurate within ±2%, and can significantly effect the level of agreement [41] between theory, experiment, and numerical solution. Thus, the numerical solutions and theoretical values used the nominal shock Mach number of 1.095 for comparison. A solution for $M_s = 1.117$, 2% above nominal, is presented as a final comparison.

Initial conditions for the computations consist of placing the shock just ahead of the plate at time zero by establishing pre-shock and post-shock conditions on either side of the point selected. The shock is then allowed to move freely as time progresses. With the temperature held at T_1 the normal momentum equation is solved to obtain the pressure at the wall, in combination with the no-slip constraint at the wall. The numerical solution is sampled at a point $5.080 \times 10^{-2} m$ downstream of the leading edge to obtain the heat flux at this point. This point was chosen consistent with the first sampling point of Smith in the shock tube experiment. The computations are carried out to a time of approximately one millisecond, the approximate time of transition to turbulent flow as noted by Smith [41]. Two different grids are used
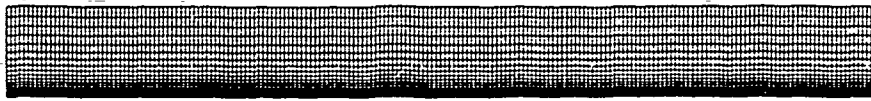
Figure 6.31. Initial Grid for Heat Flux Solutions

in this study, the first of which is shown in Figure 6.31. This grid consists of 201 points in the axial direction and 31 points in the normal direction. The grid spacing is held constant in the axial direction at $\Delta x = 2.540 \times 10^{-3} m$ and is stretched in the normal direction from an initial value of $\Delta y_i = 3.355 \times 10^{-5} m$ to a final value of $\Delta y_f = 5.594 \times 10^{-3} m$. Grid densities are based upon assuming a Blasius flat-plate boundary-layer thickness at the sampling location [49]:

$$\delta \approx \frac{5x}{\sqrt{Re_x}} \tag{6.30}$$

where x is the distance to the sampling location and Re_x is the Reynolds number based upon the velocity behind the moving shock wave. The initial spacing in the normal direction is chosen as $\Delta y_i \approx \delta/20$. The axial and final normal spacing are chosen to provide a reasonable aspect ratio throughout the domain.

Solutions presented can again be taken as the results obtained through utilizing either ATNSC1 or ATNSC2 since the steady Reynolds number is sufficiently large as to provide for the exact same solution from either algorithm. Figure 6.32 is the solution obtained when the c values were held the same as for the shock-boundary-layer interaction test case of the previous section. Namely, $c_1 = c_3 = 0.0$ and $c_2 = c_4 = 0.025$. The numerical solution is compared to the theory of Mirels [31] which is valid for weak shocks. Time is referenced to the time of the shock wave passing the sampling point. The peak heat flux is much less than theory or experiment, but it should be realized that the theoretical value goes to infinity at the

101

exact moment of shock passage. The numerical solution is initially less than theory, but soon turns so as to become greater that the theoretical flux. The numerical solution continues to be greater than the theoretical value as the shock continues to progress downstream. Agreement between the numerical solution and experiment is good beyond approximately 0.3 msec. Figure 6.33 gives the percent difference, Eq 3.17, between the theoretical value and the ATNSC solution as a function of time. The initial large difference is expected as theory predicts an infinite heat flux. The numerical solution continues to exhibit a larger percent difference as time goes on. A dramatic change in the slope of the heat flux profile at approximately 0.05 msec suggests there may be an anology to the behavior of the skin friction profile of the previous section with regards to ϵ.

Turning again to the work of Seider and Hänel [39], they observed the wall temperature on a flat plate approached the freestream temperature, rather than the recovery temperature, as ϵ was increased. They also found that this effect was negated when they increased the number of points in the boundary-layer from 7 to 14. While increasing the number of points in the boundary-layer is reasonable for steady state calculations, for the unsteady calculations of this test case there is no boundary-layer immediately at shock passing.

Figures 6.34 and 6.35 depict the ATNSC solution when ϵ is set to 0 for all fields. The peak heat flux has increased from the value of 0.94 BTU$/ft^2 \cdot s$ of Figure 6.32 to 1.24 BTU$/ft^2 \cdot s$. The heat flux profile is much smoother than Figure 6.34 and approaches the theoretical values very rapidly. Figure 6.35 shows that the calculated heat flux becomes greater than the theoretical value and then drops to a value 7% lower that theoretical, followed by a rise to a final level just 1% lower that the theoretical level. The early rise above theoretical levels followed by a drop below the theoretical level may perhaps be explained by examining Figure 6.34. The theoretical curve must approach infinity as time goes to zero. Following backwards along the curve. the rise in heat transfer must begin before the associated rise in

102
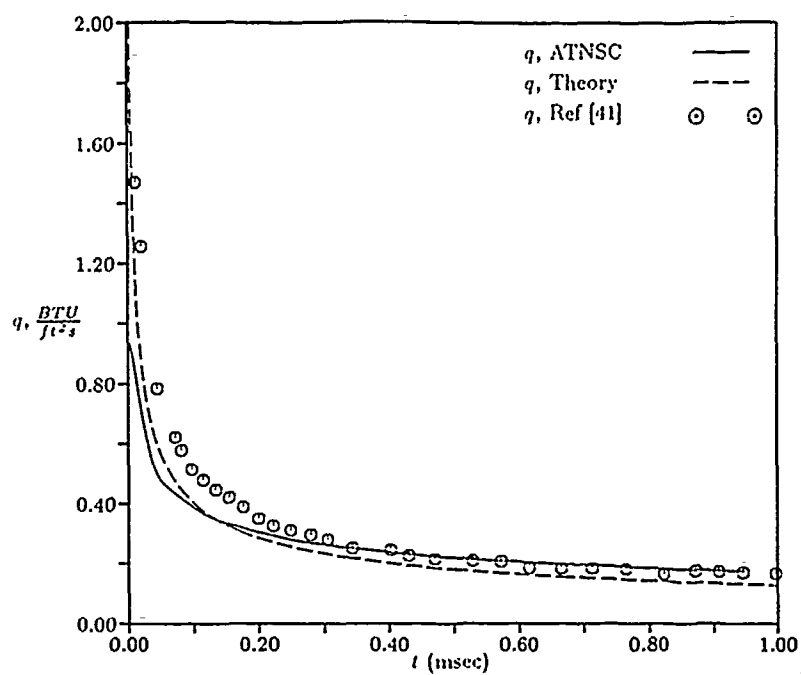
Figure 6.32. Heat Flux History ($\epsilon_1 = \epsilon_3 = 0, \epsilon_2 = \epsilon_4 = 0.025$)
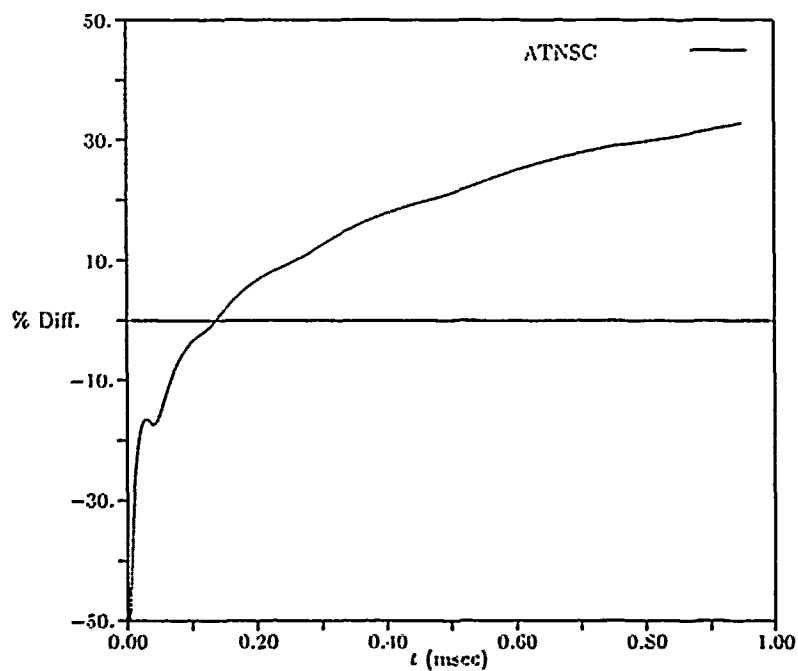
Figure 6.33. Percent Difference Between Theory and ATNSC Solution
($\epsilon_1 = \epsilon_3 = 0, \epsilon_2 = \epsilon_4 = 0.025$)

103

the numerical solution, or any physical solution, since neither approach infinity at time zero. Both the numerical and theoretical heat flux profiles are shifted below the experimental profile. Increasing the shock Mach number to the upper end of the experimental tolerance is suggested, and will be examined shortly.

Visbal's implementation of the Beam-Warming algorithm, Eq 5.39, is also used to obtain a solution to this test case. Trapezoidal time differencing is used to provide second-order accuracy in time.

Figures 6.36 and 6.37 represent the solution obtained using the nominal recommended value of the second and fourth-order damping coefficients as given in Section 6.3. Beam-Warming predicts a peak heat flux between that of Figures 6.34 and 6.32. Rather severe oscillations occur in the heat flux just after the shock passes the sampling point but eventually damp out to a final heat flux value 26% higher than the theorectical value. Beam-Warming heat flux values agree well with experiment after approximately 0.2 msec. This is surprising in light of the severe oscillations occuring prior to this time.

The values of the damping coefficients are now doubled, consistent with the shock-boundary-layer interaction case. and the solution of Figures 6.38 and 6.39 obtained. The peak heat flux has been reduced significantly and the oscillations damped somewhat, but the final heat flux value has increased to 33% above the theoretical value. Beam-Warming predictions are now higher than the experimental values after approximately 0.3 msec. Thus. as the oscillations are damped out. the overall heat flux prediction suffers.

The damping coefficients are finally reduced to half of their nominal value resulting in the solutions of Figures 6.40 and 6.41. The peak heat flux is approaching a value consistent with the results of Figure 6.34 but the oscillations have become particularly severe. In fact. reducing the damping much below this point causes the algorithm to become unstable. The lower damping of this solution provides the best Beam Warming prediction of the final heat flux value. but this is still 18% above the
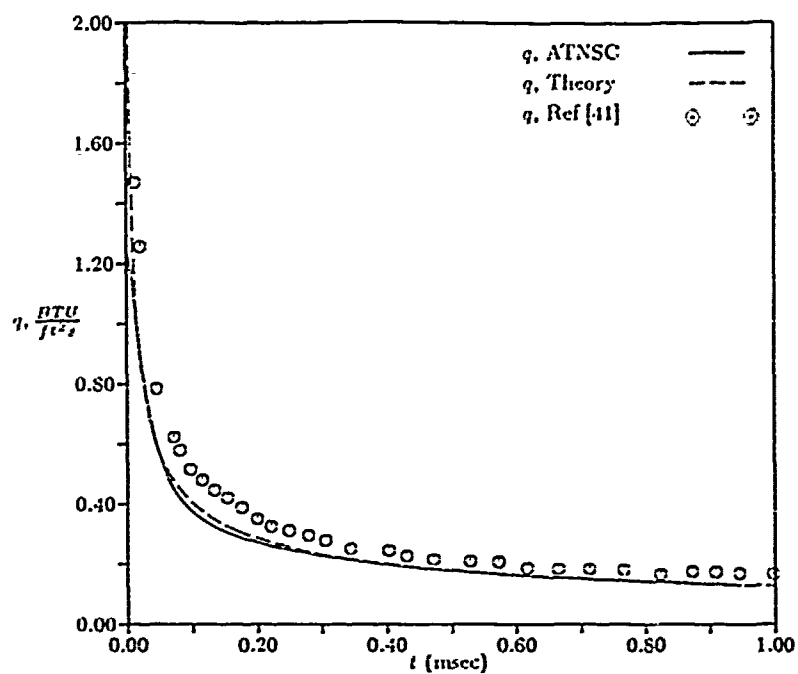
Figure 6.34. Heat Flux History ($\epsilon_1 = \epsilon_2 = \epsilon_3 = \epsilon_4 = 0$)
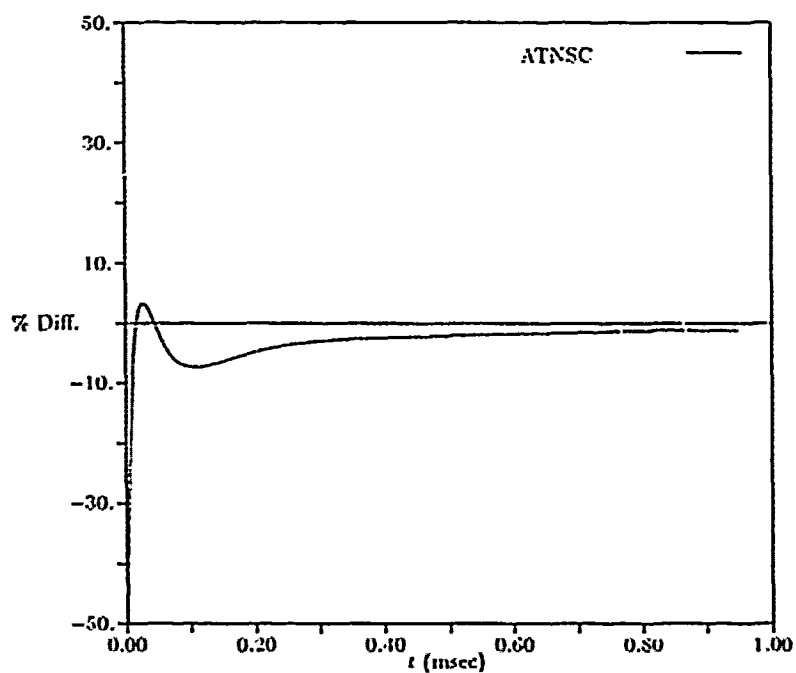
Figure 6.35. Percent Difference Between Theory and ATNSC Solution
($\epsilon_1 = \epsilon_2 = \epsilon_3 = \epsilon_4 = 0$)

105
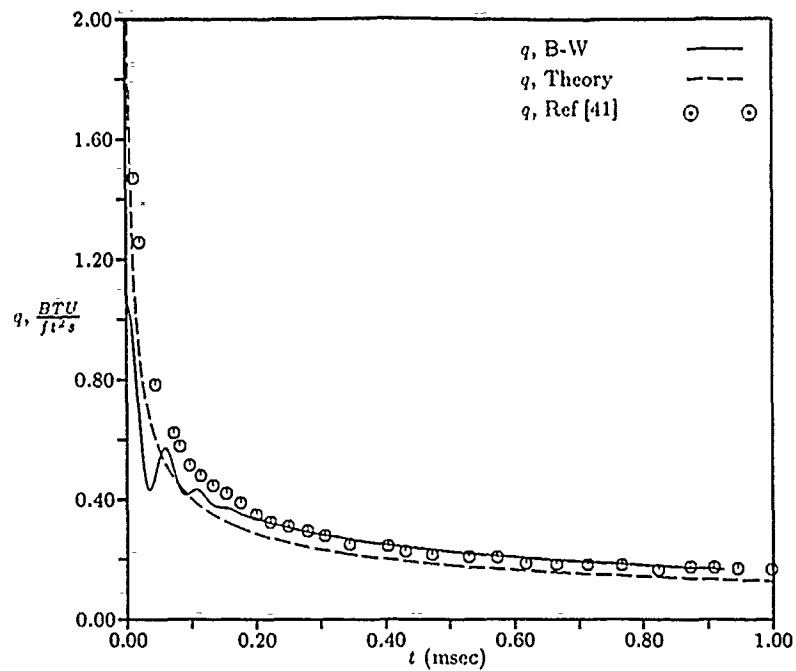
Figure 6.36. Heat Flux History ($\omega_e^\xi = 0.02, \omega_e^\eta = 0.04, \omega_i^\xi = \omega_i^\eta = 0.25$)
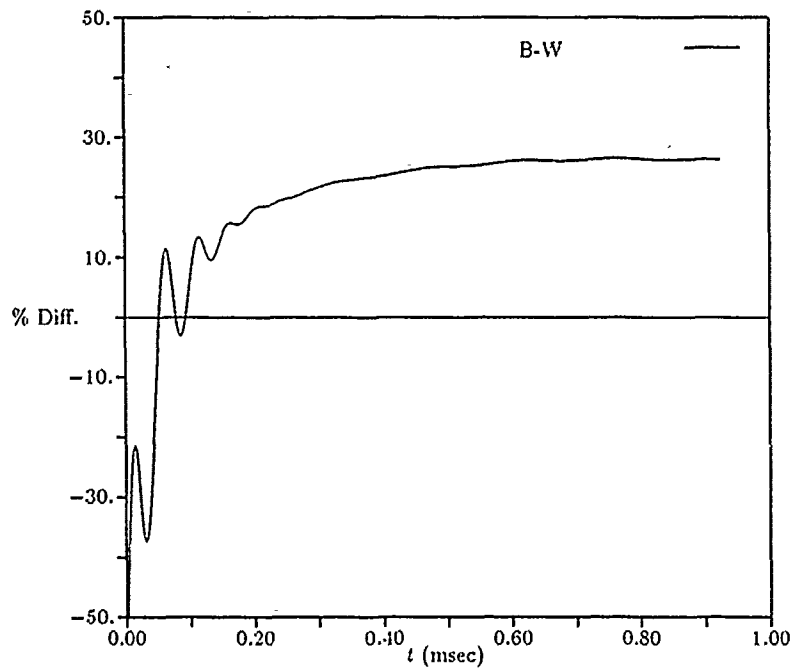
Figure 6.37. Percent Difference Between Theory and Beam-Warming Solution
($\omega_e^\xi = 0.02, \omega_e^\eta = 0.04, \omega_i^\xi = \omega_i^\eta = 0.25$)

106
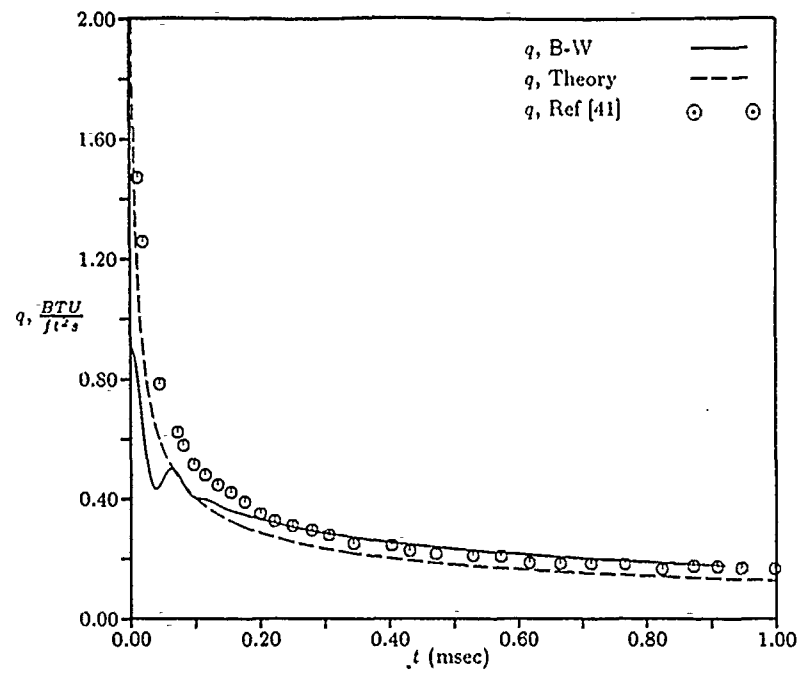
Figure 6.38. Heat Flux History ($\omega_e^\xi = 0.04, \omega_e^\eta = 0.08, \omega_i^\xi = \omega_i^\eta = 0.50$)
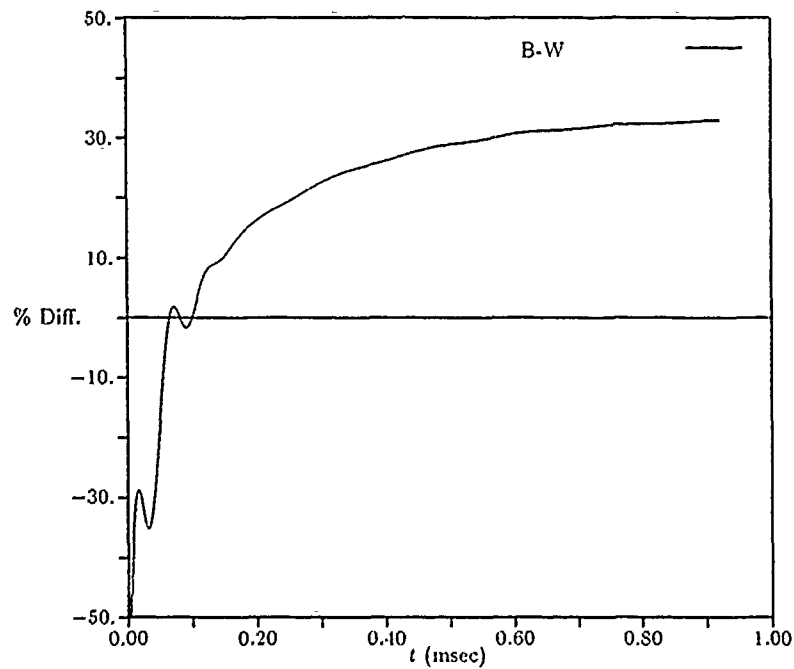
Figure 6.39. Percent Difference Between Theory and Beam-Warming Solution
($\omega_e^\xi = 0.04, \omega_e^\eta = 0.08, \omega_i^\xi = \omega_i^\eta = 0.50$)

107

theoretical value. Oscillations in the Beam-Warming solutions of Figures 6.36, 6.38, and 6.40 suggest a common frequency, independent of the damping applied. Further examination of the Beam-Warming solutions confirm this. Beam-Warming breaks the initial shock wave into a series of compressions and expansion shocks propagating downstream. As these nonphysical waves pass the sampling point, oscillations in the heat flux are observed. Varying the amount of damping applied affects the magnitude of the jumps across these waves, but not the frequency at which they are generated.

A new grid is now utilized in an attempt to see the effect on heat flux of decreasing Δx in the vicinity of the sampling point. This new grid is shown in Figure 6.42. The grid spacing varies in the axial direction from an initial value of $\Delta x = 5.066 \times 10^{-3}$ at the upstream boundary to $\Delta x = 1.252 \times 10^{-4}$ at the sampling point to $\Delta x = 2.026 \times 10^{-2}$ at the downstream boundary. The grid is stretched away from the wall with the same initial spacing as the grid of Figure 6.31 but with a final spacing of $\Delta y = 1.252 \times 10^{-2}$ at the upper boundary.

Figures 6.43 and 6.44 depict the result of utilizing ATNSC to arrive at a solution with $\epsilon = 0$ in all fields. Figure 6.43 shows that the predicted peak heat flux has increased 24% over that of Figure 6.34. The heat flux profile seems to have been stretched immediately at shock passage, remaining unchanged after approximately 0.1 msec, and is still shifted below the experimental profile. This is verified by comparison of Figure 6.44 and Figure 6.35.

The Beam-Warming algorithm is applied to this new grid using the nominal damping coefficients mentioned earlier. Results are shown in Figures 6.45 and 6.46. While the peak predicted heat flux has increased over that of Figure 6.36, it is just beginning to approached the level of the ATNSC prediction on the previous grid. At times greater than 0.3 msec, the solution is tending away form the good agreement with experimental data exhibited in Figure 6.36. Figure 6.46 shows a 8% increase in the difference from theory, as compared to Figure 6.37, for the final heat flux value.
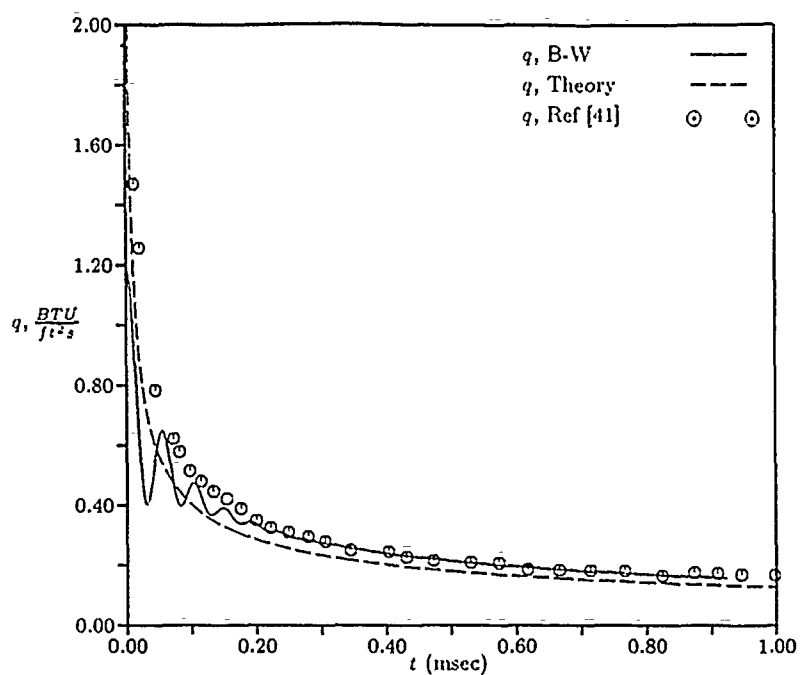
Figure 6.40. Heat Flux History ($\omega_e^\xi = 0.01, \omega_e^\eta = 0.02, \omega_i^\xi = \omega_i^\eta = 0.125$)
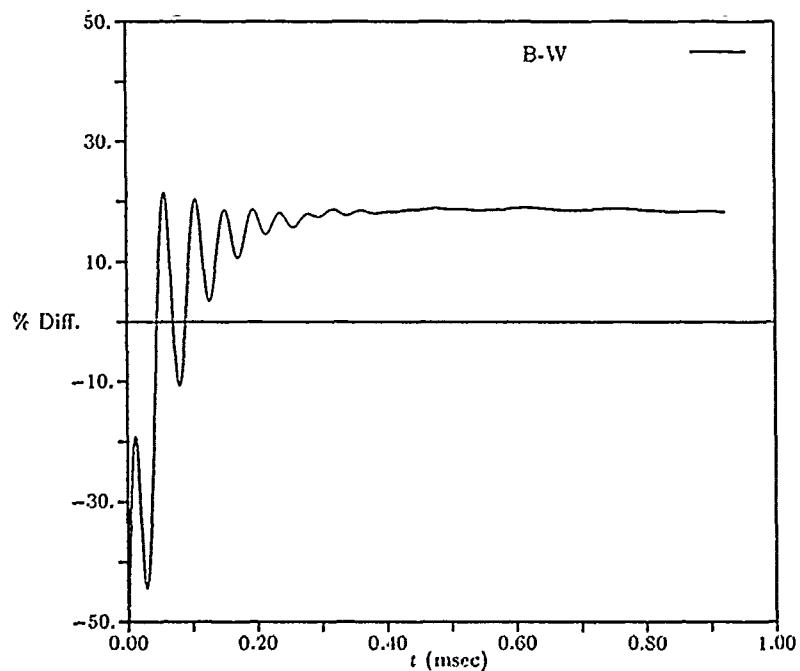
Figure 6.41. Percent Difference Between Theory and Beam-Warming Solution
($\omega_e^\xi = 0.01, \omega_e^\eta = 0.02, \omega_i^\xi = \omega_i^\eta = 0.125$)

109
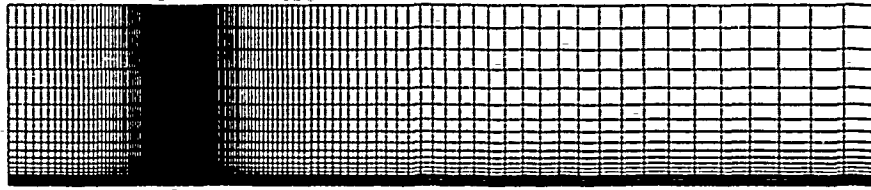
Figure 6.42. Second Grid for Heat Flux Solutions

Finally, solutions were computed with the ATNSC and Beam-Warming algorithms with $M_s = 1.117$ for comparison against each other and the experimental data. ATNSC calculations again used $\epsilon = 0$, while nominal values of the damping coefficients were used for the Beam-Warming solution. Figure 6.47 presents the time history for this case. Agreement between theory, experiment, and the ATNSC solution is excellent in this case, and suggests that the experimental shock Mach number was probably closer to 2% above the nominal value. Beam-Warming again underpredicts the peak heat flux, displays oscillations as compressions and expansion shocks pass the sampling location, and utimately overpredicts the heat flux level.

It is clear that a TVD based algorithm such as ATNSC is necessary to obtain acceptable solutions for the problem of unsteady shock-induced heat transfer. The solutions are free of any oscillations and come extremely close to the theoretical values of Mirels [30]. In contrast, the Beam-Warming algorithm yields solutions with oscillatory behavior, due to the generation of nonphysical waves, even at relatively high values of the damping coefficients. In no instance did the Beam-Warming algorithm yield an acceptable comparison with theoretical values, predicting heat flux values $18 - 34\%$ higher than theory.

All ATNSC solutions are undertaken at a CFL of 0.95, with the time step restriction of Eq 1.28. This results in approximately 7000 sweeps to arrive at a time

110
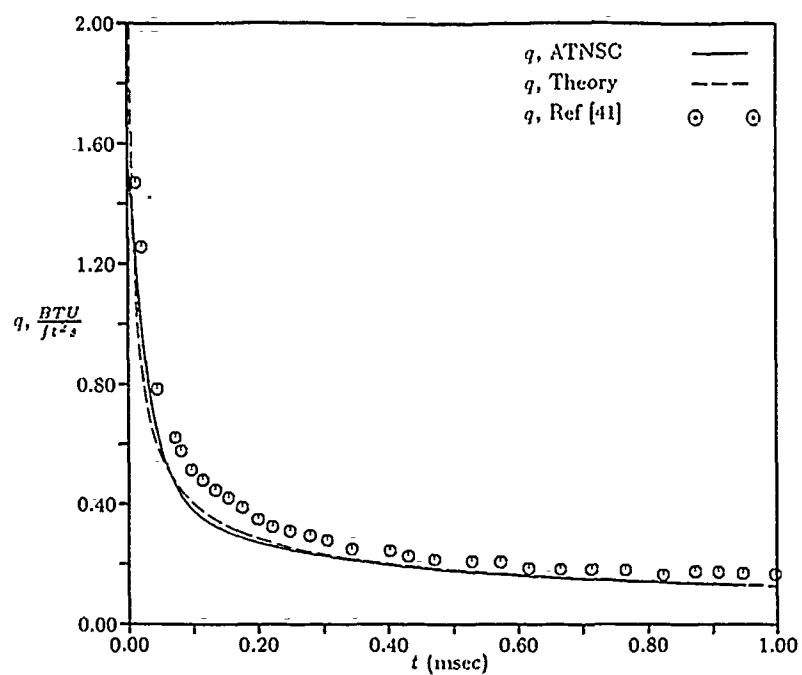
Figure 6.43. Heat Flux History ($\epsilon_1 = \epsilon_2 = \epsilon_3 = \epsilon_4 = 0$)
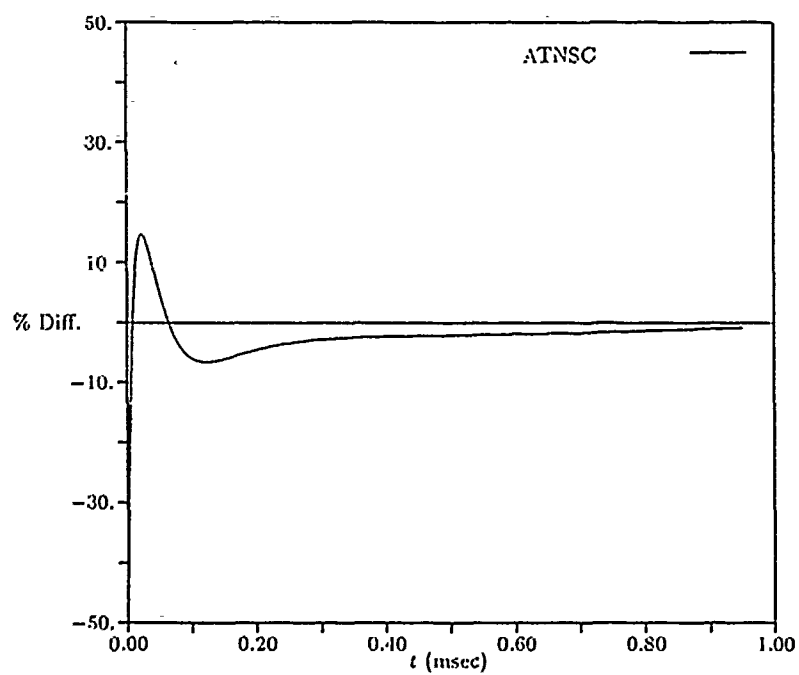
Figure 6.44. Percent Difference Between Theory and ATNSC Solution
($\epsilon_1 = \epsilon_2 = \epsilon_3 = \epsilon_4 = 0$)

111
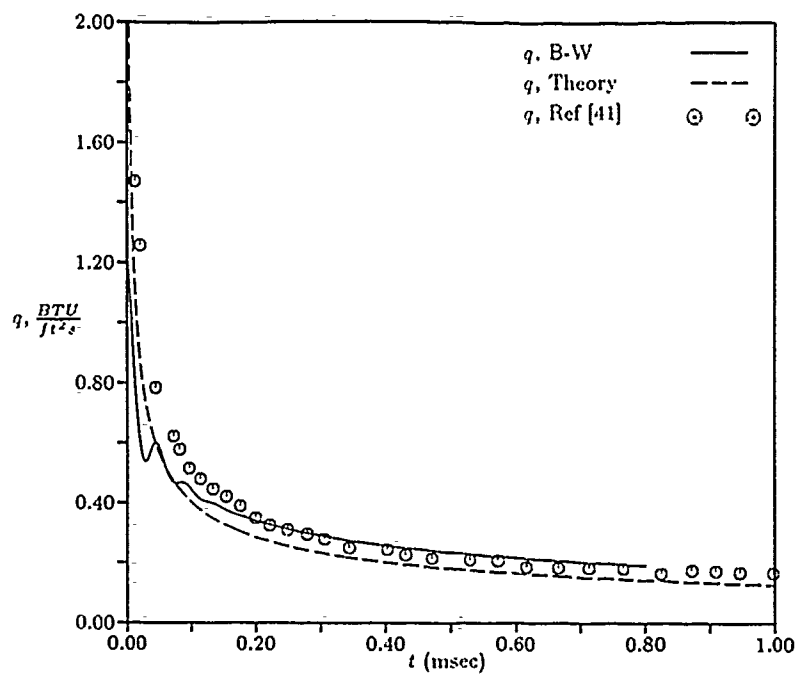
Figure 6.45. Heat Flux History ($\omega_e^\xi = 0.02, \omega_e^\eta = 0.04, \omega_i^\xi = \omega_i^\eta = 0.25$)
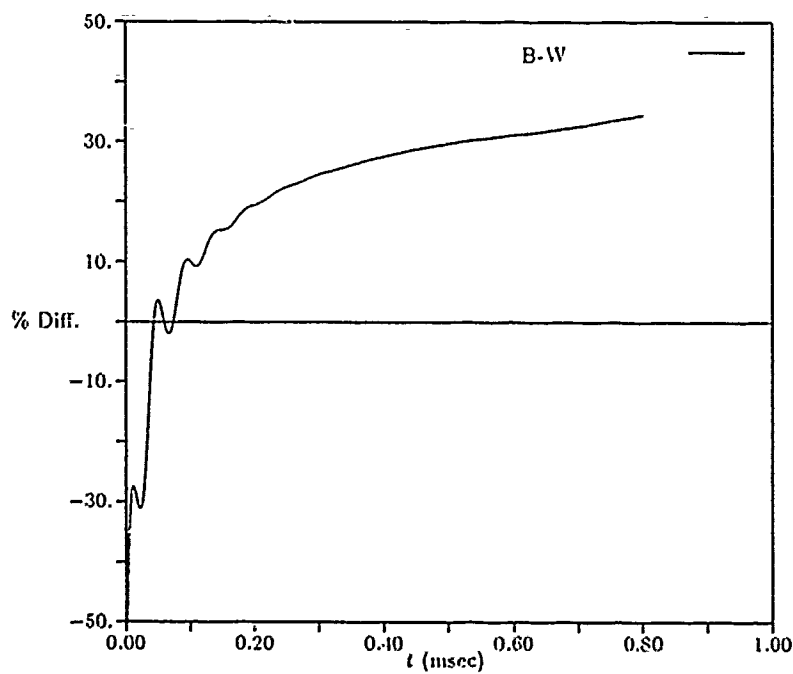
Figure 6.46. Percent Difference Between Theory and Beam-Warming Solution
($\omega_e^\xi = 0.02, \omega_e^\eta = 0.04, \omega_i^\xi = \omega_i^\eta = 0.25$)
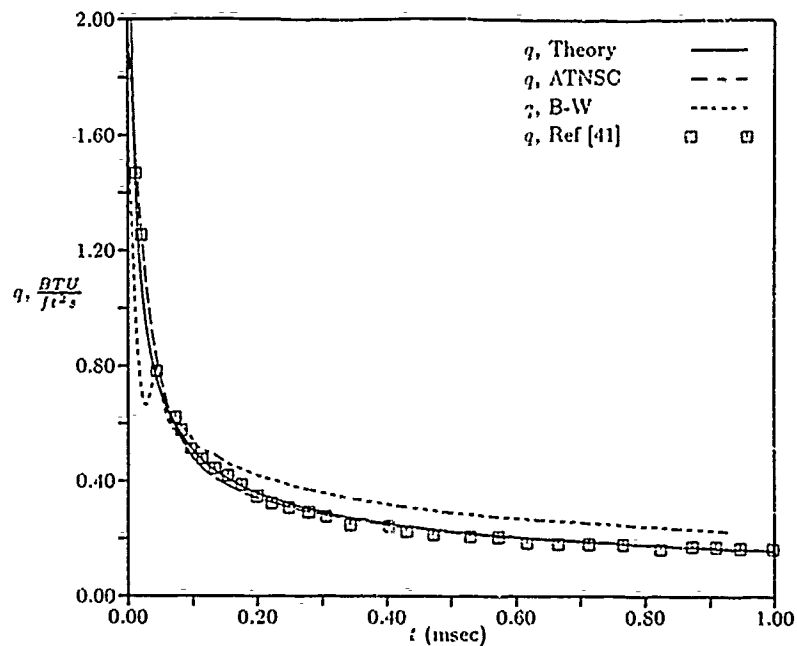
Figure 6.47. Heat Flux History ($M_s = 1.117$)

of 1.0 msec for the first grid, and approximately 14000 sweeps for the second grid. The Beam-Warming solutions utilize a constant time step which was chosen from the smallest time step taken by the ATNSC algorithm.

6.5 Conclusions

TVD methodolgy has been applied to problems not previously examined using TVD schemes. Prior research concentrated mainly on supersonic and hypersonic flows, both inviscid and viscous, and was almost solely directed toward obtaining steady-state solutions. The current effort has extended the TVD methodology to inviscid transonic cascade flows, viscous flows with shock-induced laminar boundary layer separation, and unsteady laminar flows with signifcant shock-induced heat transfer. Additionally, an algorithm was developed herein that shows promise for application to low Reynolds number situations.

Transonic cascade flows are currently of great interest to gas turbine engine

designers and researchers [2, 14, 13]. Analysis of these flows is a severe test of an algorithm because of the wide Mach number range, typically $0.3 \leq M \leq 1.3$, and the fact that the flow is confined in a passage where wave systems tend to reflect back into the domain. Results presented in Section 3.4 show that not only do the TVD schemes of Sections 2.2.2 and 2.2.3 yield steady-state results in excellent agreement with experiment, but that the transient behavior is also modeled correctly. Correct modeling of this transient behavior is an important achievement, since previous efforts have been unsuccessful in this regard [38, 15].

Laminar shock-boundary-layer interaction has been studied by numerous researchers using highly regarded algorithms such as the MacCormack [28], Dawes [10], Beam-Warming [11], and Newton [26] methods. While acceptable predictions of the pressure profile in the boundary-layer have been computed, researchers have remained unable to accurately compute the skin friction profile. The ATNSC algorithms finally provide the means to accurately compute pressure profiles, separation and reattachment locations, and skin friction profiles in excellent agreement with the available experimental data. Results given in Section 6.3 are testament to this. In addition to the success in solving this complex problem, the current effort extends the knowledge of how TVD entropy correction affects the boundary-layer velocity profile.

Unsteady shock-induced heat transfer has been studied theoretically [30, 31], experimentally [14, 41], and has recently become of interest computationally. The increased interest is due to the enhanced system performance available through accurate knowlege of the heat transfer [6]. However, it is not uncommon for computed heat flux values to be an order of magnitude different from experimental values [17]. The ATNSC algorithms represent a significant advancement in the state-of-the-art for computing shock-induced heat transfer. Solutions computed with the ATNSC schemes, presented in Section 6.4.2, are far superior to the nonphysical Beam-Warming solutions and agree well with both theory and experiment. Addi

tionally, the ATNSC1 data processing rate is 16% faster than that for Beam-Warming using the same time step.

Results of applying the ATNSC2 scheme to the viscous Burgers' equation suggest that the scheme may be beneficial to investigators studying low Reynolds number flows. The scheme is extremely stable and exhibits superb accuracy for this model problem. Conventional wisdom states that TVD schemes are not recommended for problems containing no discontinuities, since they degrade to first- order accuracy near points of extrema [45]. Behavior of the ATNSC2 scheme suggests that TVD algorithms warrant a closer examination for application to shock-free flows.

The research described herein represents a significant contribution to the field of computational fluid dynamics. Suggestions for extending the research efforts are presented in the following section.

6.6 Further Research

Further research needs to be conducted in several areas. The main question in terms of the inviscid investigations relates to the effect of grid cell skewness on entropy production. Isolating this investigation to the inviscid case will enable any insights to be directly implemented into a viscous algorithm, were it would be difficult to distinguish between spurious entropy production and normal viscous dissipation.

Two areas should be addressed for the viscous algorithms. First is the effect of the second-order accurate algorithm at low Reynolds numbers. The Reynolds numbers of interest herein, except for Burgers' equation, were on the order of 10^5 and no distinguishable difference between the ATNSC1 and ATNSC2 algorithms was observed. However, the low Reynolds number test provided by Burgers' equation dramatically showed the enhanced performance of the second-order algorithm over its first-order counterpart. Although no low Reynolds number flows containing shocks comes to mind, except for the high altitude transistion regime were the continuum assumption fails to hold, further investigation into the applicability of the second-

order algorithm is certainly warranted. Further analysis of the truncation error cancelling terms in ATNSC2 should be performed. If some of the terms are negligible for certain flow situations, a dramatic increase in computational efficiency may be possible.

Second, performance of the ATNSC algorithms with a turbulence model included should be investigated. At higher overall pressure ratios than the one considered in Section 6.3, the boundary-layer tends to transition to turbulent upon reattachment, resulting in higher skin friction levels. As previously mentioned. non-TVD algorithms under- predict the laminar skin friction level beyond reattachment. Preliminary investigations show that implementation of a Baldwin-Lomax turbulence model [3] tends to overpredict the skin friction in the turbulent region. This initially leads the author to believe that turbulence models, developed in the context of non-TVD algorithms, may compensate for a non-TVD scheme's tendency to under-predict skin friction.

Overall, the TVD based viscous algorithms perform exceptionally well on the test cases herein. Emphasis must be placed on applying these algorithms to even more rigorous test cases so as to gain an even greater understanding of their weaknesses as well as their strengths.

Appendix A. *Viscous Jacobians*

$$A_1 = \frac{\partial F_v}{\partial U} = \begin{bmatrix} A_1(1,1) & A_1(1,2) & A_1(1,3) & A_1(1,4) \\ A_1(2,1) & A_1(2,2) & A_1(2,3) & A_1(2,4) \\ A_1(3,1) & A_1(3,2) & A_1(3,3) & A_1(3,4) \\ A_1(4,1) & A_1(4,2) & A_1(4,3) & A_1(4,4) \end{bmatrix} \qquad (A.1)$$

$A_1(1,1) = 0$

$A_1(2,1) = \frac{\partial}{\partial x}\left(\frac{m}{\rho}\right)\frac{\partial}{\partial \rho}(2\mu+\lambda) + \frac{\partial}{\partial y}\left(\frac{n}{\rho}\right)\frac{\partial \lambda}{\partial \rho} - (2\mu+\lambda)\frac{\partial}{\partial x}\left(\frac{m}{\rho^2}\right) - \lambda\frac{\partial}{\partial y}\left(\frac{n}{\rho^2}\right)$

$A_1(3,1) = \frac{\partial \mu}{\partial \rho}\left[\frac{\partial}{\partial x}\left(\frac{n}{\rho}\right) + \frac{\partial}{\partial y}\left(\frac{m}{\rho}\right)\right] - \mu\left[\frac{\partial}{\partial x}\left(\frac{n}{\rho^2}\right) + \frac{\partial}{\partial y}\left(\frac{m}{\rho^2}\right)\right]$

$A_1(4,1) = \frac{m}{\rho}A_1(2,1) - \frac{m}{\rho^2}\left[(2\mu+\lambda)\frac{\partial}{\partial x}\left(\frac{m}{\rho}\right) + \lambda\frac{\partial}{\partial y}\left(\frac{n}{\rho}\right)\right]$

$+1/C_v\left\{\frac{\partial k}{\partial \rho}\left[\frac{\partial}{\partial x}\left(\frac{e}{\rho}\right) - \frac{1}{2}\frac{\partial}{\partial x}\left(\frac{m^2+n^2}{\rho^2}\right)\right] - k\left[\frac{\partial}{\partial x}\left(\frac{e}{\rho^2}\right) - \frac{\partial}{\partial x}\left(\frac{m^2+n^2}{\rho^3}\right)\right]\right\}$

$+\frac{n}{\rho}\left(\frac{\partial \mu}{\partial \rho} - \frac{\mu}{\rho}\right)\left[\frac{\partial}{\partial x}\left(\frac{n}{\rho}\right) + \frac{\partial}{\partial y}\left(\frac{m}{\rho}\right)\right] - \frac{n}{\rho}\mu\left[\frac{\partial}{\partial x}\left(\frac{n}{\rho^2}\right) + \frac{\partial}{\partial y}\left(\frac{m}{\rho^2}\right)\right]$

$A_1(1,2) = 0$

$A_1(2,2) = \frac{\partial}{\partial x}\left(\frac{m}{\rho}\right)\frac{\partial}{\partial m}(2\mu+\lambda) + \frac{\partial}{\partial y}\left(\frac{n}{\rho}\right)\frac{\partial \lambda}{\partial m} + (2\mu+\lambda)\frac{\partial}{\partial x}\left(\frac{1}{\rho}\right)$

$A_1(3,2) = \frac{\partial \mu}{\partial m}\left[\frac{\partial}{\partial x}\left(\frac{n}{\rho}\right) + \frac{\partial}{\partial y}\left(\frac{m}{\rho}\right)\right] + \mu\frac{\partial}{\partial y}\left(\frac{1}{\rho}\right)$

$A_1(4,2) = \frac{m}{\rho}A_1(2,2) + \frac{1}{\rho}\left[(2\mu+\lambda)\frac{\partial}{\partial x}\left(\frac{m}{\rho}\right) + \lambda\frac{\partial}{\partial y}\left(\frac{n}{\rho}\right)\right]$

$+1/C_v\left\{\frac{\partial k}{\partial m}\left[\frac{\partial}{\partial x}\left(\frac{e}{\rho}\right) - \frac{1}{2}\frac{\partial}{\partial x}\left(\frac{m^2+n^2}{\rho^2}\right)\right] - k\frac{\partial}{\partial x}\left(\frac{m}{\rho^2}\right)\right\}$

$+\frac{n}{\rho}\left\{\frac{\partial \mu}{\partial m}\left[\frac{\partial}{\partial x}\left(\frac{n}{\rho}\right) + \frac{\partial}{\partial y}\left(\frac{m}{\rho}\right)\right] + \mu\frac{\partial}{\partial y}\left(\frac{1}{\rho}\right)\right\}$

$A_1(1,3) = 0$

$A_1(2,3) = \frac{\partial}{\partial x}\left(\frac{m}{\rho}\right)\frac{\partial}{\partial n}(2\mu+\lambda) + \frac{\partial}{\partial y}\left(\frac{n}{\rho}\right)\frac{\partial \lambda}{\partial n} + \lambda\frac{\partial}{\partial y}\left(\frac{1}{\rho}\right)$

$A_1(3,3) = \frac{\partial \mu}{\partial n}\left[\frac{\partial}{\partial x}\left(\frac{n}{\rho}\right) + \frac{\partial}{\partial y}\left(\frac{m}{\rho}\right)\right] + \mu\frac{\partial}{\partial x}\left(\frac{1}{\rho}\right)$

$$A_1(4,3) = \frac{m}{\rho} A_1(2,3) + \frac{\mu}{\rho}\left[\frac{\partial}{\partial x}\left(\frac{n}{\rho}\right) + \frac{\partial}{\partial y}\left(\frac{m}{\rho}\right)\right]$$

$$+1/C_v\left\{\frac{\partial k}{\partial n}\left[\frac{\partial}{\partial x}\left(\frac{e}{\rho}\right) - \frac{1}{2}\frac{\partial}{\partial x}\left(\frac{m^2+n^2}{\rho^2}\right)\right] - k\frac{\partial}{\partial x}\left(\frac{n}{\rho^2}\right)\right\}$$

$$+\frac{n}{\rho}\left\{\frac{\partial \mu}{\partial n}\left[\frac{\partial}{\partial x}\left(\frac{n}{\rho}\right) + \frac{\partial}{\partial y}\left(\frac{m}{\rho}\right)\right] + \mu\frac{\partial}{\partial x}\left(\frac{1}{\rho}\right)\right\}$$

$$A_1(1,4) = 0$$

$$A_1(2,4) = \frac{\partial}{\partial x}\left(\frac{m}{\rho}\right)\frac{\partial}{\partial e}(2\mu + \lambda) + \frac{\partial}{\partial y}\left(\frac{n}{\rho}\right)\frac{\partial \lambda}{\partial e}$$

$$A_1(3,4) = \frac{\partial \mu}{\partial e}\left[\frac{\partial}{\partial x}\left(\frac{n}{\rho}\right) + \frac{\partial}{\partial y}\left(\frac{m}{\rho}\right)\right]$$

$$A_1(4,4) = \frac{m}{\rho} A_1(2,4) + \frac{n}{\rho}\frac{\partial \mu}{\partial e}\left[\frac{\partial}{\partial x}\left(\frac{n}{\rho}\right) + \frac{\partial}{\partial y}\left(\frac{m}{\rho}\right)\right]$$

$$+1/C_v\left\{\frac{\partial k}{\partial e}\left[\frac{\partial}{\partial x}\left(\frac{e}{\rho}\right) - \frac{1}{2}\frac{\partial}{\partial x}\left(\frac{m^2+n^2}{\rho^2}\right)\right] + k\frac{\partial}{\partial x}\left(\frac{1}{\rho}\right)\right\}$$

$$A_2 = \frac{\partial F_v}{\partial U_x} \tag{A.2}$$

is given by

$$\begin{bmatrix} 0 & 0 & 0 & 0 \\ -(2\mu + \lambda)\frac{m}{\rho^2} & \frac{2\mu+\lambda}{\rho} & 0 & 0 \\ -\mu\frac{n}{\rho^2} & 0 & \frac{\mu}{\rho} & 0 \\ -\left(2\mu + \lambda - \frac{k}{C_v}\right)\frac{m^2}{\rho^3} - \left(\mu - \frac{k}{C_v}\right)\frac{n^2}{\rho^3} - \frac{k}{C_v}\frac{e}{\rho^2} & \left(2\mu + \lambda - \frac{k}{C_v}\right)\frac{m}{\rho^3} & \left(\mu - \frac{k}{C_v}\right)\frac{n}{\rho^3} & \frac{k}{C_v \rho} \end{bmatrix}$$

$$A_3 = \frac{\partial F_v}{\partial U_y} = \begin{bmatrix} 0 & 0 & 0 & 0 \\ -\lambda\frac{n}{\rho^2} & 0 & \frac{\lambda}{\rho} & 0 \\ -\mu\frac{m}{\rho^2} & \frac{\mu}{\rho} & 0 & 0 \\ -(\mu + \lambda)\frac{mn}{\rho^3} & \mu\frac{n}{\rho^3} & \lambda\frac{m}{\rho^2} & 0 \end{bmatrix} \tag{A.3}$$

$$B_1 = \frac{\partial G_v}{\partial U} = \begin{bmatrix} B_1(1,1) & B_1(1,2) & B_1(1,3) & B_1(1,4) \\ B_1(2,1) & B_1(2,2) & B_1(2,3) & B_1(2,4) \\ B_1(3,1) & B_1(3,2) & B_1(3,3) & B_1(3,4) \\ B_1(4,1) & B_1(4,2) & B_1(4,3) & B_1(4,4) \end{bmatrix} \tag{A.4}$$

$B_1(1,1) = 0$

$B_1(2,1) = \frac{\partial \mu}{\partial \rho} \left[\frac{\partial}{\partial x} \left(\frac{n}{\rho} \right) + \frac{\partial}{\partial y} \left(\frac{m}{\rho} \right) \right] - \mu \left[\frac{\partial}{\partial x} \left(\frac{n}{\rho^2} \right) + \frac{\partial}{\partial y} \left(\frac{m}{\rho^2} \right) \right]$

$B_1(3,1) = \frac{\partial}{\partial x} \left(\frac{m}{\rho} \right) \frac{\partial \lambda}{\partial \rho} + \frac{\partial}{\partial y} \left(\frac{n}{\rho} \right) \frac{\partial}{\partial \rho} (2\mu + \lambda) - \lambda \frac{\partial}{\partial x} \left(\frac{m}{\rho^2} \right) - (2\mu + \lambda) \frac{\partial}{\partial y} \left(\frac{n}{\rho^2} \right)$

$B_1(4,1) = \frac{n}{\rho} B_1(3,1) - \frac{n}{\rho^2} \left[(2\mu + \lambda) \frac{\partial}{\partial y} \left(\frac{n}{\rho} \right) + \lambda \frac{\partial}{\partial x} \left(\frac{m}{\rho} \right) \right]$

$\qquad + 1/C_v \left\{ \frac{\partial k}{\partial \rho} \left[\frac{\partial}{\partial y} \left(\frac{e}{\rho} \right) - \frac{1}{2} \frac{\partial}{\partial y} \left(\frac{m^2 + n^2}{\rho^2} \right) \right] - k \left[\frac{\partial}{\partial y} \left(\frac{e}{\rho^2} \right) - \frac{\partial}{\partial y} \left(\frac{m^2 + n^2}{\rho^3} \right) \right] \right\}$

$\qquad + \frac{m}{\rho} \left(\frac{\partial \mu}{\partial \rho} - \frac{\mu}{\rho} \right) \left[\frac{\partial}{\partial x} \left(\frac{n}{\rho} \right) + \frac{\partial}{\partial y} \left(\frac{m}{\rho} \right) \right] - \frac{m}{\rho} \mu \left[\frac{\partial}{\partial x} \left(\frac{n}{\rho^2} \right) + \frac{\partial}{\partial y} \left(\frac{m}{\rho^2} \right) \right]$

$B_1(1,2) = 0$

$B_1(2,2) = \frac{\partial \mu}{\partial m} \left[\frac{\partial}{\partial x} \left(\frac{n}{\rho} \right) + \frac{\partial}{\partial y} \left(\frac{m}{\rho} \right) \right] + \mu \frac{\partial}{\partial y} \left(\frac{1}{\rho} \right)$

$B_1(3,2) = \frac{\partial}{\partial y} \left(\frac{n}{\rho} \right) \frac{\partial}{\partial m} (2\mu + \lambda) + \frac{\partial}{\partial x} \left(\frac{m}{\rho} \right) \frac{\partial \lambda}{\partial m} + \lambda \frac{\partial}{\partial x} \left(\frac{1}{\rho} \right)$

$B_1(4,2) = \frac{n}{\rho} B_1(3,2) + \left(\frac{\mu}{\rho} + \frac{m}{\rho} \frac{\partial \mu}{\partial m} \right) \left[\frac{\partial}{\partial x} \left(\frac{n}{\rho} \right) + \frac{\partial}{\partial y} \left(\frac{m}{\rho} \right) \right]$

$\qquad + 1/C_v \left\{ \frac{\partial k}{\partial m} \left[\frac{\partial}{\partial y} \left(\frac{e}{\rho} \right) - \frac{1}{2} \frac{\partial}{\partial y} \left(\frac{m^2 + n^2}{\rho^2} \right) \right] - k \frac{\partial}{\partial y} \left(\frac{m}{\rho^2} \right) \right\} + \mu \frac{m}{\rho} \frac{\partial}{\partial y} \left(\frac{1}{\rho} \right)$

$B_1(1,3) = 0$

$B_1(2,3) = \frac{\partial \mu}{\partial n} \left[\frac{\partial}{\partial x} \left(\frac{n}{\rho} \right) + \frac{\partial}{\partial y} \left(\frac{m}{\rho} \right) \right] + \mu \frac{\partial}{\partial x} \left(\frac{1}{\rho} \right)$

$B_1(3,3) = \frac{\partial}{\partial y} \left(\frac{n}{\rho} \right) \frac{\partial}{\partial n} (2\mu + \lambda) + \frac{\partial}{\partial x} \left(\frac{m}{\rho} \right) \frac{\partial \lambda}{\partial n} + (2\mu + \lambda) \frac{\partial}{\partial y} \left(\frac{1}{\rho} \right)$

$B_1(4,3) = \frac{n}{\rho} B_1(3,3) + \frac{1}{\rho} \left[(2\mu + \lambda) \frac{\partial}{\partial y} \left(\frac{n}{\rho} \right) + \lambda \frac{\partial}{\partial x} \left(\frac{m}{\rho} \right) \right]$

$\qquad + 1/C_v \left\{ \frac{\partial k}{\partial n} \left[\frac{\partial}{\partial y} \left(\frac{e}{\rho} \right) - \frac{1}{2} \frac{\partial}{\partial y} \left(\frac{m^2 + n^2}{\rho^2} \right) \right] - k \frac{\partial}{\partial y} \left(\frac{n}{\rho^2} \right) \right\}$

$\qquad + \frac{m}{\rho} \left\{ \frac{\partial \mu}{\partial n} \left[\frac{\partial}{\partial x} \left(\frac{n}{\rho} \right) + \frac{\partial}{\partial y} \left(\frac{m}{\rho} \right) \right] + \mu \frac{\partial}{\partial x} \left(\frac{1}{\rho} \right) \right\}$

$B_1(1,4) = 0$

$B_1(2,4) = \frac{\partial \mu}{\partial e} \left[\frac{\partial}{\partial x} \left(\frac{n}{\rho} \right) + \frac{\partial}{\partial y} \left(\frac{m}{\rho} \right) \right]$

$$B_1(3,4) = \frac{\partial}{\partial y}\left(\frac{n}{\rho}\right)\frac{\partial}{\partial e}(2\mu+\lambda) + \frac{\partial}{\partial x}\left(\frac{m}{\rho}\right)\frac{\partial\lambda}{\partial e}$$

$$B_1(4,4) = \frac{m}{\rho}B_1(3,4) + \frac{m}{\rho}\frac{\partial\mu}{\partial e}\left[\frac{\partial}{\partial x}\left(\frac{n}{\rho}\right) + \frac{\partial}{\partial y}\left(\frac{m}{\rho}\right)\right]$$

$$+1/C_v\left\{\frac{\partial k}{\partial e}\left[\frac{\partial}{\partial y}\left(\frac{e}{\rho}\right) - \frac{1}{2}\frac{\partial}{\partial y}\left(\frac{m^2+n^2}{\rho^2}\right)\right] + k\frac{\partial}{\partial y}\left(\frac{1}{\rho}\right)\right\}$$

$$B_2 = \frac{\partial G_v}{\partial U_y} \qquad\qquad (A.5)$$

is given by

$$\begin{bmatrix} 0 & 0 & 0 & 0 \\ -\mu\frac{m}{\rho^2} & \frac{\mu}{\rho} & 0 & 0 \\ -(2\mu+\lambda)\frac{n}{\rho^2} & 0 & \frac{2\mu+\lambda}{\rho} & 0 \\ -\left(2\mu+\lambda-\frac{k}{C_v}\right)\frac{n^2}{\rho^3} - \left(\mu-\frac{k}{C_v}\right)\frac{m^2}{\rho^3} - \frac{k}{C_v}\frac{e}{\rho^2} & \left(\mu-\frac{k}{C_v}\right)\frac{m}{\rho^2} & \left(2\mu+\lambda-\frac{k}{C_v}\right)\frac{n}{\rho^2} & \frac{k}{C_v\rho} \end{bmatrix}$$

$$B_3 = \frac{\partial G_v}{\partial U_x} = \begin{bmatrix} 0 & 0 & 0 & 0 \\ -\mu\frac{n}{\rho^2} & 0 & \frac{\mu}{\rho} & 0 \\ -\lambda\frac{m}{\rho^2} & \frac{\lambda}{\rho} & 0 & 0 \\ -(\mu+\lambda)\frac{mn}{\rho^3} & \lambda\frac{n}{\rho^2} & \mu\frac{m}{\rho^2} & 0 \end{bmatrix} \qquad (A.6)$$

Appendix B. *ATEC Routines and FLOWTRACE Results*

B.1 Description of ATEC Routines

For clarity, the routines are described in the order they would generally be called, independent of the sweep direction.

ATEC	- main program
GEOMETRY	- computes cell centers based on corner values
TFORM	- computes the metric transformation terms
INITIAL	- enforces the initial conditions
STORE	- stores the dependent variables at the current time level
FLUXF	- computes the ξ direction flux
FLUXG	- computes the η direction flux
ROEAVGZ	- computes Roe averaged quantities along constant η lines
ROEAVGE	- computes Roe averaged quantities along constant ξ lines
EVALUEZ	- computes the ξ eigenvalues
EVALUEE	- computes the η eigenvalues
TMSTEP	- computes the allowable time step
ALPHAZ	- computes the difference of characteristic variables in the ξ direction
ALPHAE	- computes the difference of characteristic variables in the η direction
GCALCZ	- computes the flux limiters for the ξ direction flux
GCALCE	- computes the flux limiters for the η direction flux
BETATVDZ	- computes artificial dissipation for ξ sweep
BETATVDE	- computes artificial dissipation for η sweep
EVECTORZ	- computes the eigenvectors for the ξ eigenvalues
EVECTORE	- computes the eigenvectors for the η eigenvalues
ARTCOMPZ	- computes the final artificial dissipation for the ξ direction sweep
ARTCOMPE	- computes the final artificial dissipation for the η direction sweep

FSOLVE   - solves for the drpendent variables during the ξ sweep

GSOLVE   - solves for the dependent variables during the η sweep

BNDBLD   - enforces the blade or wall surface boundary conditions

BNDEX   - enforces the exit plane boundary conditions

BNDPER   - enforces the periodic boundary conditions

BNDIN   - enforces the inlet plane boundary conditions

NORM   - computes the L_2 and L_∞ norms

OUTPUT   - outputs the solution vector

B.2 ATEC-FV (Finite-Volume Formulation)

The data processing rate for the finite-volume formulation is 1.2274×10^{-5} seconds per grid point per time level for the CRAY X-MP/216, utiiling a 177×20 grid. FLOWTRACE results are for 1000 iterations (2000 time levels).

```
FLOWTRACE RESULTS OF ROUTINES
 SORTED BY TIME USED (DESCENDING)
 (CPU Times are Shown in Seconds)
```

Routine Name	Tot Time	# Calls	Avg Time	Percentage	Accum%
BETATVDE	1.40E+01	352000	3.98E-05	16.10	16.10
BETATVDZ	1.15E+01	57000	2.02E-04	13.23	29.33
GSOLVE	6.99E+00	352000	1.99E-05	8.04	37.37
ATEC	6.55E+00	1	6.55E+00	7.54	44.91
ROEAVGE	5.55E+00	3000	1.85E-03	6.39	51.30
ROEAVGZ	5.30E+00	3000	1.77E-03	6.10	57.40
FSOLVE	4.86E+00	57000	8.52E-05	5.59	62.99
EVECTORE	3.52E+00	352000	1.00E-05	4.05	67.04
ALPHAZ	3.28E+00	3000	1.10E-03	3.78	70.82
GCALCZ	3.16E+00	3000	1.05E-03	3.63	74.45
ARTCOMPE	3.01E+00	352000	8.55E-06	3.46	77.91
EVECTORZ	2.38E+00	57000	4.18E-05	2.74	80.65
FLUXG	2.37E+00	5000	4.74E-04	2.72	83.37
ARTCOMPZ	2.32E+00	57000	4.06E-05	2.66	86.04
ALPHAE	2.29E+00	2000	1.14E-03	2.63	88.67
FLUXF	2.27E+00	5000	4.54E-04	2.61	91.28
GCALCE	2.15E+00	2000	1.07E-03	2.47	93.75
NORM	1.06E+00	400	2.65E-03	1.22	94.97

TMSTEP	1.03E+00	1000	1.03E-03	1.19	96.15
OUTPUT	7.18E-01	1	7.18E-01	0.83	96.98
EVALUEE	6.50E-01	3000	2.17E-04	0.75	97.73
EVALUEZ	6.18E-01	3000	2.06E-04	0.71	98.44
BNDBLD	4.66E-01	5000	9.32E-05	0.54	98.97
BNDEX	3.91E-01	5000	7.82E-05	0.45	99.42
BNDPER	3.35E-01	5000	6.70E-05	0.39	99.81
BNDIN	1.46E-01	5000	2.92E-05	0.17	99.98
STORE	1.61E-02	100	1.61E-04	0.02	100.00
TFORM	3.25E-03	1	3.25E-03	0.00	100.00
GEOMETRY	2.75E-04	1	2.75E-04	0.00	100.00
INITIAL	1.83E-04	1	1.83E-04	0.00	100.00

===

Totals	8.69E+01	1689505

FLOWTRACE RESULTS OF ROUTINES

SORTED BY 'IN-LINE' FACTOR (DESCENDING)

(CPU Times are Shown in Seconds)

(Factors Greater Than 1 Could Indicate Candidates for In-Lining)

Routine Name	Tot Time	# Calls	Avg Time	Percentage	"In-Line" Factor
ARTCOMPE	3.01E+00	352000	8.55E-06	3.46	349.66
EVECTORE	3.52E+00	352000	1.00E-05	4.05	298.90
GSOLVE	6.99E+00	352000	1.99E-05	8.04	150.58
BETATVDE	1.40E+01	352000	3.98E-05	16.10	75.20
ARTCOMPZ	2.32E+00	57000	4.06E-05	2.66	11.92
EVECTORZ	2.38E+00	57000	4.18E-05	2.74	11.59

FSOLVE	4.86E+00	57000 8.52E-05	5.59	5.68
BETATVDZ	1.15E+01	57000 2.02E-04	13.23	2.40
BNDIN	1.46E-01	5000 2.92E-05	0.17	1.45

==

BNDPER	3.35E-01	5000 6.70E-05	0.39	0.63
BNDEX	3.91E-01	5000 7.82E-05	0.45	0.54
BNDBLD	4.66E-01	5000 9.32E-05	0.54	0.46
EVALUEZ	6.18E-01	3000 2.06E-04	0.71	0.12
EVALUEE	6.50E-01	3000 2.17E-04	0.75	0.12
FLUXF	2.27E+00	5000 4.54E-04	2.61	0.09
FLUXG	2.37E+00	5000 4.74E-04	2.72	0.09
GCALCZ	3.16E+00	3000 1.05E-03	3.63	0.02
ALPHAZ	3.28E+00	3000 1.10E-03	3.78	0.02
GCALCE	2.15E+00	2000 1.07E-03	2.47	0.02
ALPHAE	2.29E+00	2000 1.14E-03	2.63	0.01
ROEAVGZ	5.30E+00	3000 1.77E-03	6.10	0.01
ROEAVGE	5.55E+00	3000 1.85E-03	6.39	0.01
ATEC	6.55E+00	1 6.55E+00	7.54	0.00
NORM	1.06E+00	400 2.65E-03	1.22	0.00
TMSTEP	1.03E+00	1000 1.03E-03	1.19	0.01
OUTPUT	7.18E-01	1 7.18E-01	0.83	0.00
STORE	1.61E-02	100 1.61E-04	0.02	0.01
TFORM	3.25E-03	1 3.25E-03	0.00	0.00
GEOMETRY	2.75E-04	1 2.75E-04	0.00	0.00
INITIAL	1.83E-04	1 1.83E-04	0.00	0.00

==

Totals	8.69E+01	1689505

B.3 ATEC-FD (Chain-Rule Formulation)

The data processing rate for the chain-rule formulation is 1.2415×10^{-5} seconds per grid point per time level for the CRAY X-MP/216, utiiling a 177×20 grid. FLOWTRACE results are for 1000 iterations (2000 time levels).

```
FLOWTRACE RESULTS OF ROUTINES
 SORTED BY TIME USED (DESCENDING)
 (CPU Times are Shown in Seconds)
```

Routine Name	Tot Time	# Calls	Avg Time	Percentage	Accum%
BETATVDE	1.37E+01	352000	3.88E-05	15.56	15.56
BETATVDZ	1.13E+01	57000	1.97E-04	12.81	28.37
GSOLVE	8.01E+00	352000	2.28E-05	9.12	37.49
ATEC	6.58E+00	1	6.58E+00	7.49	44.99
FSOLVE	5.59E+00	57000	9.80E-05	6.36	51.34
ROEAVGE	5.54E+00	3000	1.85E-03	6.30	57.64
ROEAVGZ	5.29E+00	3000	1.76E-03	6.02	63.67
EVECTORE	3.54E+00	352000	1.01E-05	4.03	67.70
ALPHAZ	3.25E+00	3000	1.08E-03	3.69	71.39
GCALCZ	3.15E+00	3000	1.05E-03	3.58	74.97
ARTCOMPE	2.99E+00	352000	8.49E-06	3.40	78.37
FLUXG	2.36E+00	5000	4.72E-04	2.69	81.06
EVECTORZ	2.34E+00	57000	4.11E-05	2.67	83.73
ARTCOMPZ	2.26E+00	57000	3.97E-05	2.57	86.30
FLUXF	2.26E+00	5000	4.52E-04	2.57	88.88
ALPHAE	2.26E+00	2000	1.13E-03	2.57	91.45
GCALCE	2.14E+00	2000	1.07E-03	2.44	93.89
NORM	1.03E+00	400	2.57E-03	1.17	95.06

TMSTEP	1.03E+00	1000	1.03E-03	1.17	96.23
OUTPUT	7.13E-01	1	7.13E-01	0.81	97.04
EVALUEE	6.33E-01	3000	2.11E-04	0.72	97.76
EVALUEZ	6.15E-01	3000	2.05E-04	0.70	98.46
BNDBLD	4.63E-01	5000	9.26E-05	0.53	98.99
BNDEX	3.91E-01	5000	7.82E-05	0.44	99.43
BNDPER	3.34E-01	5000	6.68E-05	0.38	99.81
BNDIN	1.46E-01	5000	2.92E-05	0.17	99.98
STORE	1.56E-02	100	1.56E-04	0.02	100.00
TFORM	1.87E-03	1	1.87E-03	0.00	100.00
GEOMETRY	2.79E-04	1	2.79E-04	0.00	100.00
INITIAL	2.05E-04	1	2.05E-04	0.00	100.00

==

Totals	8.79E+01	1689505

FLOWTRACE RESULTS OF ROUTINES

SORTED BY 'IN-LINE' FACTOR (DESCENDING)

(CPU Times are Shown in Seconds)

(Factors Greater Than 1 Could Indicate Candidates for In-Lining)

Routine Name	Tot Time	# Calls	Avg Time	Percentage	"In-Line" Factor
ARTCOMPE	2.99E+00	352000	8.49E-06	3.40	352.44
EVECTORE	3.54E+00	352000	1.01E-05	4.03	297.04
GSOLVE	8.01E+00	352000	2.28E-05	9.12	131.35
BETATVDE	1.37E+01	352000	3.88E-05	15.56	76.98
ARTCOMPZ	2.26E+00	57000	3.97E-05	2.57	12.20
EVECTORZ	2.34E+00	57000	4.11E-05	2.67	11.77

FSOLVE	5.59E+00	57000 9.80E-05	6.36	4.94
BETATVDZ	1.13E+01	57000 1.97E-04	12.81	2.45
BNDIN	1.46E-01	5000 2.92E-05	0.17	1.46
======	======	======	======	======
BNDPER	3.34E-01	5000 6.68E-05	0.38	0.64
BNDEX	3.91E-01	5000 7.82E-05	0.44	0.54
BNDBLD	4.63E-01	5000 9.26E-05	0.53	0.46
EVALUEZ	6.15E-01	3000 2.05E-04	0.70	0.12
EVALUEE	6.33E-01	3000 2.11E-04	0.72	0.12
FLUXF	2.26E+00	5000 4.52E-04	2.57	0.09
FLUXG	2.36E+00	5000 4.72E-04	2.69	0.09
GCALCZ	3.15E+00	3000 1.05E-03	3.58	0.02
ALPHAZ	3.25E+00	3000 1.08E-03	3.69	0.02
GCALCE	2.14E+00	2000 1.07E-03	2.44	0.02
ALPHAE	2.26E+00	2000 1.13E-03	2.57	0.02
ROEAVGZ	5.29E+00	3000 1.76E-03	6.02	0.01
ROEAVGE	5.54E+00	3000 1.85E-03	6.30	0.01
ATECFD	6.58E+00	1 6.58E+00	7.49	0.00
NORM	1.03E+00	400 2.57E-03	1.17	0.00
TMSTEP	1.03E+00	1000 1.03E-03	1.17	0.01
OUTPUT	7.13E-01	1 7.13E-01	0.81	0.00
STORE	1.56E-02	100 1.56E-04	0.02	0.01
TFORM	1.87E-03	1 1.87E-03	0.00	0.00
GEOMETRY	2.79E-04	1 2.79E-04	0.00	0.00
INITIAL	2.05E-04	1 2.05E-04	0.00	0.00
======	======	======	======	======
Totals	8.79E+01	1689505		

Appendix C. *ATNSC Routines and FLOWTRACE Results*

C.1 Description of ATNSC1 and ATNSC2 Routines

For clarity, the routines are described in the order they would generally be called, independent of the sweep direction.

ATNSC1 (ATNSC2)   - main program

GEOMETRY   - computes cell centers based on corner values

TFORM   - computes the metric transformation terms

INITIAL   - enforces the initial conditions

STORE   - stores the dependent variables at the current time level

EULFLUX   - computes the inviscid flux terms

VISFLUX   - computes the viscous flux terms

ROEAVGZ   - computes Roe averaged quantities along constant η lines

ROEAVGE   - computes Roe averaged quantities along constant ξ lines

EVALUEZ   - computes the ξ eigenvalues

EVALUEE   - computes the η eigenvalues

TMSTEP   - computes the allowable time step

ALPHAZ   - computes the difference of characteristic variables in the ξ direction

ALPHAE   - computes the difference of characteristic variables in the η direction

GCALCZ   - computes the flux limiters for the ξ direction flux

GCALCE   - computes the flux limiters for the η direction flux

JACOBIAN   - computes the viscous Jacobians (ATNSC2 only)

PSIZETA   - computes the final viscous flux in the ξ direction

PSIETA   - computes the final viscous flux in the η direction

BETATVDZ   - computes artificial dissipation for ξ sweep

BETATVDE   - computes artificial dissipation for η sweep

EVECTORZ   - computes the eigenvectors for the ξ eigenvalues

EVECTORE	- computes the eigenvectors for the η eigenvalues
ARTCOMPZ	- computes the final artificial dissipation for the ξ direction sweep
ARTCOMPE	- computes the final artificial dissipation for the η direction sweep
FSOLVE	- solves for the drpendent variables during the ξ sweep
GSOLVE	- solves for the dependent variables during the η sweep
BNDBLD	- enforces the blade or wall surface boundary conditions
BNDEX	- enforces the exit plane boundary conditions
BNDPER	- enforces the periodic boundary conditions
BNDIN	- enforces the inlet plane boundary conditions
NORM	- computes the L_2 and L_∞ norms
OUTPUT	- outputs the solution vector

C.2 ATNSC1 (Constant Damping)

The data processing rate for the constant ϵ case is 1.6071×10^{-5} seconds per grid point per time level for the CRAY X-MP/216, utiiling a 133×60 grid. FLOWTRACE results are for 200 iterations (400 time levels).

```
FLOWTRACE RESULTS OF ROUTINES
 SORTED BY TIME USED (DESCENDING)
 (CPU Times are Shown in Seconds)
```

Routine Name	Tot Time	# Calls	Avg Time	Percentage	Accum%
VISFLUX	7.66E+00	1000	7.66E-03	14.92	14.92
FSOLVE	6.13E+00	34800	1.76E-04	11.94	26.86
BETATVDZ	4.69E+00	34800	1.35E-04	9.13	35.99
GSOLVE	4.40E+00	52400	8.40E-05	8.57	44.56
BETATVDE	4.25E+00	52400	8.11E-05	8.28	52.84
ROEAVGE	2.67E+00	600	4.45E-03	5.20	58.04
ROEAVGZ	2.66E+00	600	4.44E-03	5.19	63.23
ATNSC1	1.92E+00	1	1.92E+00	3.74	66.97
ALPHAZ	1.61E+00	600	2.68E-03	3.13	70.09
EULFLUX	1.59E+00	1000	1.59E-03	3.11	73.20
GCALCZ	1.53E+00	600	2.55E-03	2.98	76.18
OUTPUT	1.49E+00	1	1.49E+00	2.90	79.08
PSIZETA	1.20E+00	600	2.00E-03	2.34	81.42
EVECTORZ	1.19E+00	34800	3.41E-05	2.31	83.73
ARTCOMPZ	1.18E+00	34800	3.38E-05	2.29	86.02
ALPHAE	1.08E+00	400	2.71E-03	2.11	88.13
TMSTEP	1.08E+00	200	5.38E-03	2.09	90.22
GCALCE	1.02E+00	400	2.55E-03	1.99	92.21

EVECTORE	9.69E-01	52400	1.85E-05	1.89	94.10
ARTCOMPE	8.09E-01	52400	1.54E-05	1.58	95.67
PSIETA	8.05E-01	400	2.01E-03	1.57	97.24
NORM	5.01E-01	80	6.26E-03	0.98	98.22
EVALUEZ	3.24E-01	600	5.39E-04	0.63	98.85
EVALUEE	3.23E-01	600	5.39E-04	0.63	99.48
BNDBLD	1.97E-01	1000	1.97E-04	0.38	99.86
BNDEX	4.17E-02	1000	4.17E-05	0.08	99.94
BNDIN	1.32E-02	1000	1.32E-05	0.03	99.97
STORE	7.56E-03	20	3.78E-04	0.01	99.98
INITIAL	5.34E-03	1	5.34E-03	0.01	99.99
TFORM	4.42E-03	1	4.42E-03	0.01	100.00

===

Totals	5.13E+01	359504

FLOWTRACE RESULTS OF ROUTINES

SORTED BY 'IN-LINE' FACTOR (DESCENDING)

(CPU Times are Shown in Seconds)

(Factors Greater Than 1 Could Indicate Candidates for In-Lining)

Routine Name	Tot Time	# Calls	Avg Time	Percentage	"In-Line" Factor
ARTCOMPE	8.09E-01	52400	1.54E-05	1.58	28.84
EVECTORE	9.69E-01	52400	1.85E-05	1.89	24.08
ARTCOMPZ	1.18E+00	34800	3.38E-05	2.29	8.74
EVECTORZ	1.19E+00	34800	3.41E-05	2.31	8.68
BETATVDE	4.25E+00	52400	8.11E-05	8.28	5.49
GSOLVE	4.40E+00	52400	8.40E-05	8.57	5.30

BETATVDZ	4.69E+00	34800 1.35E-04	9.13	2.19
FSOLVE	6.13E+00	34800 1.76E-04	11.94	1.68
==				
BNDIN	1.32E-02	1000 1.32E-05	0.03	0.64
BNDEX	4.17E-02	1000 4.17E-05	0.08	0.20
BNDBLD	1.97E-01	1000 1.97E-04	0.38	0.04
VISFLUX	7.66E+00	1000 7.66E-03	14.92	0.00
ROEAVGE	2.67E+00	600 4.45E-03	5.20	0.00
ROEAVGZ	2.66E+00	600 4.44E-03	5.19	0.00
ATNSC1	1.92E+00	1 1.92E+00	3.74	0.00
ALPHAZ	1.61E+00	600 2.68E-03	3.13	0.00
EULFLUX	1.59E+00	1000 1.59E-03	3.11	0.01
GCALCZ	1.53E+00	600 2.55E-03	2.98	0.00
OUTPUT	1.49E+00	1 1.49E+00	2.90	0.00
PSIZETA	1.20E+00	600 2.00E-03	2.34	0.00
ALPHAE	1.08E+00	400 2.71E-03	2.11	0.00
TMSTEP	1.08E+00	200 5.38E-03	2.09	0.00
GCALCE	1.02E+00	400 2.55E-03	1.99	0.00
PSIETA	8.05E-01	400 2.01E-03	1.57	0.00
NORM	5.01E-01	80 6.26E-03	0.98	0.00
EVALUEZ	3.24E-01	600 5.39E-04	0.63	0.01
EVALUEE	3.23E-01	600 5.39E-04	0.63	0.01
STORE	7.56E-03	20 3.78E-04	0.01	0.00
INITIAL	5.34E-03	1 5.34E-03	0.01	0.00
TFORM	4.42E-03	1 4.42E-03	0.01	0.00
==				
Totals	5.13E+01	359504		

C.3 ATNSC1 (Anisotropic and Isotropic Damping)

The data processing rate for the variable ϵ case is 2.0457×10^{-5} seconds per grid point per time level for the CRAY X-MP/216, utiiling a 133×60 grid. FLOWTRA e results are for 200 iterations (400 time levels).

```
FLOWTRACE RESULTS OF ROUTINES
  SORTED BY TIME USED (DESCENDING)
  (CPU Times are Shown in Seconds)
```

Routine Name	Tot Time	# Calls	Avg Time	Percentage	Accum%
BETATVDZ	1.58E+01	34800	4.54E-04	24.22	24.22
VISFLUX	7.63E+00	1000	7.63E-03	11.70	35.91
BETATVDE	6.77E+00	52400	1.29E-04	10.37	46.28
FSOLVE	6.13E+00	34800	1.76E-04	9.39	55.67
GSOLVE	4.58E+00	52400	8.74E-05	7.02	62.69
ROEAVGE	2.66E+00	600	4.43E-03	4.07	66.77
ROEAVGZ	2.65E+00	600	4.42E-03	4.06	70.83
ATNSC1	1.98E+00	1	1.98E+00	3.03	73.86
ALPHAZ	1.60E+00	600	2.66E-03	2.45	76.30
EULFLUX	1.58E+00	1000	1.58E-03	2.43	78.73
OUTPUT	1.58E+00	1	1.58E+00	2.42	81.15
GCALCZ	1.53E+00	600	2.55E-03	2.34	83.49
PSIZETA	1.22E+00	600	2.04E-03	1.88	85.37
EVECTORZ	1.18E+00	34800	3.40E-05	1.81	87.18
ARTCOMPZ	1.16E+00	34800	3.34E-05	1.78	88.96
TMSTEP	1.08E+00	200	5.40E-03	1.65	90.61
ALPHAE	1.07E+00	400	2.68E-03	1.65	92.26
GCALCE	1.02E+00	400	2.55E-03	1.56	93.82

EVECTORE	9.87E-01	52400	1.88E-05	1.51	95.34
PSIETA	8.16E-01	400	2.04E-03	1.25	96.59
ARTCOMPE	8.01E-01	52400	1.53E-05	1.23	97.81
NORM	5.16E-01	84	6.15E-03	0.79	98.60
EVALUEZ	3.21E-01	600	5.35E-04	0.49	99.10
EVALUEE	3.20E-01	600	5.33E-04	0.49	99.59
BNDBLD	1.96E-01	1000	1.96E-04	0.30	99.89
BNDEX	4.26E-02	1000	4.26E-05	0.07	99.95
BNDIN	1.42E-02	1000	1.42E-05	0.02	99.97
STORE	7.79E-03	20	3.90E-04	0.01	99.99
INITIAL	5.37E-03	1	5.37E-03	0.01	99.99
TFORM	4.35E-03	1	4.35E-03	0.01	100.00

===

Totals	6.53E+01	359508

FLOWTRACE RESULTS OF ROUTINES

SORTED BY 'IN-LINE' FACTOR (DESCENDING)

(CPU Times are Shown in Seconds)

(Factors Greater Than 1 Could Indicate Candidates for In-Lining)

Routine Name	Tot Time	# Calls	Avg Time	Percentage	"In-Line" Factor
ARTCOMPE	8.01E-01	52400	1.53E-05	1.23	29.11
EVECTORE	9.87E-01	52400	1.88E-05	1.51	23.64
ARTCOMPZ	1.16E+00	34800	3.34E-05	1.78	8.86
EVECTORZ	1.18E+00	34800	3.40E-05	1.81	8.71
GSOLVE	4.58E+00	52400	8.74E-05	7.02	5.09
BETATVDE	6.77E+00	52400	1.29E-04	10.37	3.45

FSOLVE	6.13E+00	34800 1.76E-04	9.39	1.68

===

BETATVDZ	1.58E+01	34800 4.54E-04	24.22	0.65
BNDIN	1.42E-02	1000 1.42E-05	0.02	0.60
BNDEX	4.26E-02	1000 4.26E-05	0.07	0.20
BNDBLD	1.96E-01	1000 1.96E-04	0.30	0.04
VISFLUX	7.63E+00	1000 7.63E-03	11.70	0.00
ROEAVGE	2.66E+00	600 4.43E-03	4.07	0.00
ROEAVGZ	2.65E+00	600 4.42E-03	4.06	0.00
ATNSC1	1.98E+00	1 1.98E+00	3.03	0.00
ALPHAZ	1.60E+00	600 2.66E-03	2.45	0.00
EULFLUX	1.58E+00	1000 1.58E-03	2.43	0.01
OUTPUT	1.58E+00	1 1.58E+00	2.42	0.00
GCALCZ	1.53E+00	600 2.55E-03	2.34	0.00
PSIZETA	1.22E+00	600 2.04E-03	1.88	0.00
TMSTEP	1.08E+00	200 5.40E-03	1.65	0.00
ALPHAE	1.07E+00	400 2.68E-03	1.65	0.00
GCALCE	1.02E+00	400 2.55E-03	1.56	0.00
PSIETA	8.16E-01	400 2.04E-03	1.25	0.00
NORM	5.16E-01	84 6.15E-03	0.79	0.00
EVALUEZ	3.21E-01	600 5.35E-04	0.49	0.01
EVALUEE	3.20E-01	600 5.33E-04	0.49	0.01
STORE	7.79E-03	20 3.90E-04	0.01	0.00
INITIAL	5.37E-03	1 5.37E-03	0.01	0.00
TFORM	4.35E-03	1 4.35E-03	0.01	0.00

===

Totals	6.53E+01	359508

C.4 ATNSC2 (No Jacobian Update Between Operators)

The data processing rate when the viscous Jacobians are updated only after a complete sequence of operator sweeps is 7.6128×10^{-5} seconds per grid point per time level. This is for the CRAY X-MP/216, utiiling a 133×60 grid. FLOWTRACE results are for 200 iterations (400 time levels).

```
   FLOWTRACE RESULTS OF ROUTINES
    SORTED BY TIME USED (DESCENDING)
     (CPU Times are Shown in Seconds)
```

Routine Name	Tot Time	# Calls	Avg Time	Percentage	Accum%
JACOBIAN	1.61E+02	200	8.05E-01	66.26	66.26
PSIZETA	2.01E+01	600	3.35E-02	8.26	74.53
PSIETA	1.34E+01	400	3.36E-02	5.53	80.05
VISFLUX	7.52E+00	1000	7.52E-03	3.10	83.15
FSOLVE	6.03E+00	34800	1.73E-04	2.48	85.63
BETATVDZ	4.69E+00	34800	1.35E-04	1.93	87.56
GSOLVE	4.34E+00	52400	8.28E-05	1.79	89.34
BETATVDE	3.89E+00	52400	7.43E-05	1.60	90.95
ROEAVGE	2.66E+00	600	4.43E-03	1.09	92.04
ROEAVGZ	2.65E+00	600	4.41E-03	1.09	93.13
ATNSC2	1.92E+00	1	1.92E+00	0.79	93.92
ALPHAZ	1.58E+00	600	2.63E-03	0.65	94.57
EULFLUX	1.57E+00	1000	1.57E-03	0.65	95.21
OUTPUT	1.54E+00	1	1.54E+00	0.63	95.85
GCALCZ	1.52E+00	600	2.54E-03	0.63	96.47
EVECTORZ	1.16E+00	34800	3.34E-05	0.48	96.95
ARTCOMPZ	1.14E+00	34800	3.27E-05	0.47	97.42

TMSTEP	1.07E+00	200 5.36E-03	0.44	97.86
ALPHAE	1.06E+00	400 2.66E-03	0.44	98.30
GCALCE	1.02E+00	400 2.54E-03	0.42	98.72
EVECTORE	9.42E-01	52400 1.80E-05	0.39	99.10
ARTCOMPE	7.77E-01	52400 1.48E-05	0.32	99.42
NORM	5.00E-01	80 6.26E-03	0.21	99.63
EVALUEZ	3.14E-01	600 5.23E-04	0.13	99.76
EVALUEE	3.11E-01	600 5.19E-04	0.13	99.89
BNDBLD	2.03E-01	1000 2.03E-04	0.08	99.97
BNDEX	4.14E-02	1000 4.14E-05	0.02	99.99
BNDIN	1.31E-02	1000 1.31E-05	0.01	99.99
STORE	7.45E-03	20 3.73E-04	0.00	100.00
INITIAL	5.40E-03	1 5.40E-03	0.00	100.00
TFORM	4.22E-03	1 4.22E-03	0.00	100.00

===

Totals   2.43E+02   359704

FLOWTRACE RESULTS OF ROUTINES

SORTED BY 'IN-LINE' FACTOR (DESCENDING)

(CPU Times are Shown in Seconds)

(Factors Greater Than 1 Could Indicate Candidates for In-Lining)

Routine Name	Tot Time	# Calls	Avg Time	Percentage	"In-Line" Factor
ARTCOMPE	7.77E-01	52400	1.48E-05	0.32	30.03
EVECTORE	9.42E-01	52400	1.80E-05	0.39	24.76
ARTCOMPZ	1.14E+00	34800	3.27E-05	0.47	9.05
EVECTORZ	1.16E+00	34800	3.34E-05	0.48	8.86
BETATVDE	3.89E+00	52400	7.43E-05	1.60	5.99
GSOLVE	4.34E+00	52400	8.28E-05	1.79	5.38
BETATVDZ	4.69E+00	34800	1.35E-04	1.93	2.19
FSOLVE	6.03E+00	34800	1.73E-04	2.48	1.71
==					
BNDIN	1.31E-02	1000	1.31E-05	0.01	0.65
BNDEX	4.14E-02	1000	4.14E-05	0.02	0.21
BNDBLD	2.03E-01	1000	2.03E-04	0.08	0.04
JACOBIAN	1.61E+02	200	8.05E-01	66.26	0.00
PSIZETA	2.01E+01	600	3.35E-02	8.26	0.00
PSIETA	1.34E+01	400	3.36E-02	5.53	0.00
VISFLUX	7.52E+00	1000	7.52E-03	3.10	0.00
ROEAVGE	2.66E+00	600	4.43E-03	1.09	0.00
ROEAVGZ	2.65E+00	600	4.41E-03	1.09	0.00
ATNSC2	1.92E+00	1	1.92E+00	0.79	0.00
ALPHAZ	1.58E+00	600	2.63E-03	0.65	0.00
EULFLUX	1.57E+00	1000	1.57E-03	0.65	0.01

OUTPUT	1.54E+00	1	1.54E+00	0.63	0.00
GCALCZ	1.52E+00	600	2.54E-03	0.63	0.00
TMSTEP	1.07E+00	200	5.36E-03	0.44	0.00
ALPHAE	1.06E+00	400	2.66E-03	0.44	0.00
GCALCE	1.02E+00	400	2.54E-03	0.42	0.00
NORM	5.00E-01	80	6.26E-03	0.21	0.00
EVALUEZ	3.14E-01	600	5.23E-04	0.13	0.01
EVALUEE	3.11E-01	600	5.19E-04	0.13	0.01
STORE	7.45E-03	20	3.73E-04	0.00	0.00
INITIAL	5.40E-03	1	5.40E-03	0.00	0.00
TFORM	4.22E-03	1	4.22E-03	0.00	0.00

==

Totals	2.43E+02	359704

C.5 ATNSC2 (Jacobian Update After Each Operator Sweep)

The data processing rate when the viscous Jacobians are updated after each operator sweep is 1.9988×10^{-4} seconds per grid point per time level. This is for the CRAY X-MP/216, utiiling a 133×60 grid. FLOWTRACE results are for 200 iterations (400 time levels).

```
FLOWTRACE RESULTS OF ROUTINES
  SORTED BY TIME USED (DESCENDING)
   (CPU Times are Shown in Seconds)
```

Routine Name	Tot Time	# Calls	Avg Time	Percentage	Accum%
PSIZETA	2.41E+02	600	4.01E-01	37.77	37.77
JACOBIAN	1.86E+02	1000	1.86E-01	29.15	66.93
PSIETA	1.62E+02	400	4.04E-01	25.37	92.30
VISFLUX	7.54E+00	1000	7.54E-03	1.18	93.48
FSOLVE	6.09E+00	34800	1.75E-04	0.95	94.44
BETATVDZ	4.69E+00	34800	1.35E-04	0.74	95.17
GSOLVE	4.56E+00	52400	8.69E-05	0.71	95.89
BETATVDE	4.16E+00	52400	7.93E-05	0.65	96.54
ROEAVGE	2.65E+00	600	4.42E-03	0.42	96.95
ROEAVGZ	2.65E+00	600	4.41E-03	0.41	97.37
ATNSC2	1.93E+00	1	1.93E+00	0.30	97.67
ALPHAZ	1.58E+00	600	2.63E-03	0.25	97.92
EULFLUX	1.57E+00	1000	1.57E-03	0.25	98.17
OUTPUT	1.55E+00	1	1.55E+00	0.24	98.41
GCALCZ	1.53E+00	600	2.55E-03	0.24	98.65
EVECTORZ	1.16E+00	34800	3.33E-05	0.18	98.83
ARTCOMPZ	1.14E+00	34800	3.29E-05	0.18	99.01

TMSTEP	1.06E+00	200 5.32E-03	0.17	99.18
ALPHAE	1.06E+00	400 2.66E-03	0.17	99.34
GCALCE	1.02E+00	400 2.54E-03	0.16	99.50
EVECTORE	9.79E-01	52400 1.87E-05	0.15	99.66
ARTCOMPE	7.85E-01	52400 1.50E-05	0.12	99.78
NORM	5.03E-01	80 6.29E-03	0.08	99.86
EVALUEZ	3.14E-01	600 5.24E-04	0.05	99.91
EVALUEE	3.13E-01	600 5.22E-04	0.05	99.96
BNDBLD	2.03E-01	1000 2.03E-04	0.03	99.99
BNDEX	4.24E-02	1000 4.24E-05	0.01	100.00
BNDIN	1.42E-02	1000 1.42E-05	0.00	100.00
STORE	7.44E-03	20 3.72E-04	0.00	100.00
INITIAL	5.35E-03	1 5.35E-03	0.00	100.00
TFORM	4.32E-03	1 4.32E-03	0.00	100.00

===

Totals   6.38E+02   360504

FLOWTRACE RESULTS OF ROUTINES

SORTED BY 'IN-LINE' FACTOR (DESCENDING)

(CPU Times,are Shown in Seconds)

(Factors Greater Than 1 Could Indicate Candidates for In-Lining)

Routine Name	Tot Time	# Calls	Avg Time	Percentage	"In-Line" Factor
ARTCOMPE	7.85E-01	52400	1.50E-05	0.12	29.73
EVECTORE	9.79E-01	52400	1.87E-05	0.15	23.82
ARTCOMPZ	1.14E+00	34800	3.29E-05	0.18	8.99
EVECTORZ	1.16E+00	34800	3.33E-05	0.18	8.87
BETATVDE	4.16E+00	52400	7.93E-05	0.65	5.61
GSOLVE	4.56E+00	52400	8.69E-05	0.71	5.12
BETATVDZ	4.69E+00	34800	1.35E-04	0.74	2.19
FSOLVE	6.09E+00	34800	1.75E-04	0.95	1.69
============	========	========	========	===========	============
BNDIN	1.42E-02	1000	1.42E-05	0.00	0.60
BNDEX	4.24E-02	1000	4.24E-05	0.01	0.20
BNDBLD	2.03E-01	1000	2.03E-04	0.03	0.04
PSIZETA	2.41E+02	600	4.01E-01	37.77	0.00
JACOBIAN	1.86E+02	1000	1.86E-01	29.15	0.00
PSIETA	1.62E+02	400	4.04E-01	25.37	0.00
VISFLUX	7.54E+00	1000	7.54E-03	1.18	0.00
ROEAVGE	2.65E+00	600	4.42E-03	0.42	0.00
ROEAVGZ	2.65E+00	600	4.41E-03	0.41	0.00
ATNSC2	1.93E+00	1	1.93E+00	0.30	0.00
ALPHAZ	1.58E+00	600	2.63E-03	0.25	0.00
EULFLUX	1.57E+00	1000	1.57E-03	0.25	0.01

OUTPUT	1.55E+00	1	1.55E+00	0.24	0.00
GCALCZ	1.53E+00	600	2.55E-03	0.24	0.00
TMSTEP	1.06E+00	200	5.32E-03	0.17	0.00
ALPHAE	1.06E+00	400	2.66E-03	0.17	0.00
GCALCE	1.02E+00	400	2.54E-03	0.16	0.00
NORM	5.03E-01	80	6.29E-03	0.08	0.00
EVALUEZ	3.14E-01	600	5.24E-04	0.05	0.01
EVALUEE	3.13E-01	600	5.22E-04	0.05	0.01
STORE	7.44E-03	20	3.72E-04	0.00	0.00
INITIAL	5.35E-03	1	5.35E-03	0.00	0.00
TFORM	4.32E-03	1	4.32E-03	0.00	0.00

==

Totals   6.38E+02   360504

Bibliography

1. Anderson, Dale A., John C. Tannehill, and Richard H. Pletcher. *Computational Fluid Mechanics and Heat Transfer*. Series in Computational Methods in Mechanics and Thermal Sciences. New York: Hemisphere Publishing Corporation, 1984.

2. Air Force Wright Aeronautical Laboratory. *IHPTET, Integrated High Performance Turbine Engine Technology Initiative*. AFWAL/POT Brochure.

3. Baldwin, B. S. and H. Lomax. "Thin Layer Approximation and Algebraic Model for Separated Turbulent Flows," *AIAA 16th Aerospace Sciences Meeting*. AIAA-78-257. (January 1978).

4. Gray, Robert. Air Force Aero-Propulsion and Power Laboratory.

5. Boyle, R. J. "Navier-Stokes Analysis of Turbine Blade Heat Transfer." *Gas Turbine and Aeroengine Conference*. ASME Paper No. 90-GT-42. (June 1990).

6. Brahney, James H. "Propulsion Systems for the '90s." *Aerospace Engineering*, August 1990.

7. Chakravarthy, S.R., K-Y Szema, U.C. Goldberg, J.J. Gorski, and S. Osher. "Application of a New Class of High Accuracy TVD Schemes to the Navier-Stokes Equations," *AIAA 23rd Aerospace Sciences Meeting*. AIAA-85-0165. (January 1985).

8. Chapman, D. R., D. M. Kuehn and H. K. Larson. *Investigation of Separated Flows in Supersonic and Subsonic Streams with Emphasis on the Effect of Transition*. NACA Technical Report 1356 (1958).

9. Courant, R. and K. O. Friedrichs. *Supersonic Flow and Shock Waves*. Applied Mathematical Sciences, Volume 21. New York: Springer-Verlag. 1976.

10. Dawes, W.N. " Efficient Implicit Algorithm for the equations of 2-D Viscous Compressible Flow: Application to Shock- Boundary Layer Interaction." *Journal of Heat & Fluid Flow*, Volume 4. Number 1:17-26 (March 1983).

11. Degrez, G., C.H. Boccadoro and J.F. Wendt. "The Interaction of an Oblique Shock Wave with a Laminar Boundary Layer Revisited. An Experimental and Numerical Study," *Journal of Fluid Mechanics*, Volume 177:247-263 (1987).

12. Denton, J. D. "An Improved Time Marching Method for Turbomachinery Flow Calculation." ASME Paper No. 82-GT-239. *Journal of Engineering for Power*. Vol. 105, July 1983.

13. Dix, Donald M. and James S. Petty. "Aircraft Engine Technology gets a second wind," *Aerospace America*, July 1990.

14. Doorly, D. J. and M. L. G. Oldfield. " Simulation of Shock Wave Passing on a Turbine Rotor," *Journal of Engineering for Gas Turbines and Power*, Volume 107: 998-1006 (October 1985).

15. Driver, Mark A. *Development of a Shock Capturing Code for Use as a Tool in Designing High-Work Low Aspect Ratio Turbines*. MS Thesis, AFIT/GAE/AA/88D-10. School of Engineering, Air Force Institute of Technology (AU), Wright-Patterson AFB OH, December 1988 (AD-A202 706).

16. Driver, Mark A., and Robert E. Gray. "Application of Simple Wave Theory to the Radiative Boundary Conditions Required for an Internal Flow Euler Solver," *AIAA/ASME/SAE/ASEE 25th Joint Propulsion Conference*. AIAA-89-2577. (July 1989).

17. Gray, Robert. Air Force Aero-Propulsion and Power Laboratory. Private communications. HQ WL, Wright-Patterson AFB Ohio, 1990.

18. Hakkinen, R. J., I. Greber, L. Trilling and S. S. Abarbanel. *The Interaction of an Oblique Shock Wave with a Laminar Boundary Layer*. NASA Memorandum 2-18-59W. Washington DC: (March 1959).

19. Harten, Amiram. *The Method of Artificial Compression: I. Shocks and Contact Discontinuities*. AEC Research & Development Report COO-3077-50, Courant Institute. New York University. June 1974

20. Harten, Amiram. "The Artificial Compression Method for Computation of Shocks and Contact Discontinuities. I. Single Conservation Laws." *Communications on Pure and Applied Mathematics*. Volume XXX: 611-638 (1977).

21. Harten, Amiram. "The Artificial Compression Method for Computation of Shocks and Contact Discontinuities. III. Self- Ajusting Hybrid Schemes." *Mathematics of Computation*. Volume 32: 363-389 (1978).

22. Harten. Ami. "High Resolution Schemes for Hyperbolic Conservation Laws." *Journal of Computational Physics*. Volume 49: 357-393 (1983).

23. Harten, A., J.M. Hyman and P.D. Lax. "On Finite- Difference Approximations and Entropy Conditions for Shocks." *Communications on Pure and Applied Mathematics*. Volume XXIX: 297-322 (1976).

24. Josyula, Eswar, Datta Gaitonde and Joseph Shang. "Nonequilibrium Hypersonic Flow Solutions Using the Roe Flux- Difference Split Scheme," *AIAA 22nd Fluid Dynamics, Plasma Dynamics & Lasers Conference*. AIAA-91-1700. (June 1991).

25. Lin, Herng and Ching-Chang Chieng. "Comparisons of TVD Schemes for Turbulent Transonic Projectile Aerodynamics Computations," *AIAA 29th Aerospace Sciences Meeting.* AIAA-91-0171. (January 1991).

26. Liou, Meng-Seng. " A Newton/Upwind Method and Numerical Study of Shock Wave/Boundary Layer Interactions," *International Journal for Numerical Methods in Fluids,* Volume 9:747-761 (1989).

27. Lutton, Mark. Air Force Institute of Technology, Department of Aeronautics and Astronautics. Private communications. AFIT, Wright-Patterson AFB Ohio, 1990.

28. MacCormack, Robert W. "Numerical Solution of the Interaction of a Shock Wave With ι Laminar Boundary Layer," *Lecture Notes in Physics,* Volume 8:151-163 (1971).

29. Martinelli, L. *Calculations of Viscous Flows with a Multigrid Method.* Phd Thesis. Princeton University (1987).

30. Mirels, Harold. *Laminar Boundary Layer Behind Shock Advancing into Stationary Fluid.* NACA Technical Note 3401. Cleveland Ohio: Lewis Flight Propulsion Laboratory, March 1955.

31. Mirels, Harold. *Laminar Boundary Layer Behind Shock or Thin Expansion Wave Moving into Stationary Fluid.* NACA Technical Note 3712. Cleveland Ohio: Lewis Flight Propulsion Laboratory, May 1956.

32. Müller, B. " Simple Improvements of an Upwind TVD Scheme for Hypersonic Flow," AIAA-89-1977-CP. (1989).

33. Pulliam, Thomas H. and Joseph L. Steger. "Recent Improvements in Efficiency, Accuracy, and Convergence for Implicit Approximate Factorization Algorithms," *AIAA 23rd Aerospace Sciences Meeting.* AIAA-85-0360. (January 1985).

34. Riedelbauch, S. and G. Brenner. " Numerical Simulation of Laminar Hypersonic Flow Past Blunt Bodies Including High Temperature Effects," *AIAA 21st Fluid Dynamics. Plasma Dynamics and Lasers Conference.* AIAA-90-1492. (June 1990).

35. Roache, Patrick J. *Computational Fluid Dynamics.* Albuquerque: Hermosa Publishers, 1972.

36. Roe. P. L. "Approximate Riemann Solvers. Parameter Vectors, and Difference Schemes," *Journal of Computational Physics.* Volume 43: 357-372 (1981).

37. Schlichting, Hermann. *Boundary-Layer Theory* (Seventh Edition). New York: McGraw-Hill Book Company, 1979.

38. Scott, J. N. and W. L. Hankey, Jr. "Boundary Conditions for Navier-Stokes Solutions of Unsteady Flow in a Compressor Rotor," *Three Dimensional Flow Phenomena in Fluid Machinery*. 141-151. New York: Fluid Engineering Division of the ASME, November 1985.

39. Seider, G. and D. Hänel. "Numerical Influence of Upwind TVD Schemes on Transonic Airfoil Drag Prediction," *AIAA 29th Aerospace Sciences Meeting*. AIAA-91-0184.(January 1991).

40. Shang, J. S. " Numerical Simulation of Wing-Fuselage Aerodynamic Interaction," *AIAA Journal*,Volume 22, Number 10: 1345-1353 (October 1984).

41. Smith, B.J. *Investigation of Heat Transfer to a Sharp Edged Flat Plate Using a Shock Tube*. MS Thesis, AFIT/GAE/AA/86D-16. School of Engineering, Air Force Institute of Technology (AU). Wright-Patterson AFB OH, December 1986.

42. Stabe, Roy G., Warren J. Whitney, and Thomas P. Moffit. *Performance of a High-Work Low Aspect Ratio Turbine Tested with a Realistic Inlet Radial Temperature Profile*. NASA Technical Memorandum 83655. Cleveland Ohio: Lewis Research Center, June 1984.

43. Yee, H. C. and A. Harten. " Implicit Total Variation Diminishing (TVD) Schemes for Steady-State Calculations." AIAA-83-1902.

44. Yee, H. C. and P. Kutler. *Application of Second- Order-Accurate Total Variation Diminishing (TVD) Schemes to the Euler Equations in General Geometrics*. NASA Technical Memorandum 85815. Moffett Field California: Ames Research Center. August 1983.

45. Yee. H. C. *A Class of High-Resolution Explicit and Implicit Shock-Capturing Methods*. NASA Technical Memorandum 101088. Moffett Field California: Ames Research Center, February 1989.

46. Yee, H. C., R. F. Warming, and A. Harten. "Implicit Total Variation Diminishing (TVD) Schemes for Steady-State Calculations," *Journal of Computational Physics*. Volume 57: 327-360 (1985)

47. Visbal, Miguel R. *Calculation of Viscous Transonic Flows About a Supercritical Airfoil*. AFWAL-TR-86-3013. Wright-Patterson AFB Ohio: Flight Dynamics Laboratory, July 1986.

48. Wang, J.C.T. and G.F. Widhopf. "A High-Resolution TVD Finite Volume Scheme for the Euler Equations in Conservation Form," *AIAA 25th Aerospace Sciences Meeting*. AIAA-87-0538. (January 1987).

49. White, Frank M. *Viscous Fluid Flow*. New York: McGraw-Hill. 1974.

REPORT DOCUMENTATION PAGE

Public reporting burden for this collection of information is estimated to average 1 hour per response, including the time for reviewing instructions, searching existing data sources, gathering and maintaining the data needed, and completing and reviewing the collection of information. Send comments regarding this burden estimate or any other aspect of this collection of information, including suggestions for reducing this burden, to Washington Headquarters Services, Directorate for Information Operations and Reports, 215 Jefferson Davis Highway, Suite 1204, Arlington, VA 22202-4302, and to the Office of Management and Budget, Paperwork Reduction Project (0704-0188), Washington, DC 20503

1. AGENCY USE ONLY (Leave blank)	2. REPORT DATE December 1991	3. REPORT TYPE AND DATES COVERED Doctoral Dissertation

4. TITLE AND SUBTITLE	5. FUNDING NUMBERS
High-Resolution TVD Schemes for the Analysis of I. Inviscid Supersonic and Transonic Flows II. Viscous Flows with Shock-Induced Separation and Heat Transfer	

6. AUTHOR(S)

Mark A. Driver, Capt, USAF

7. PERFORMING ORGANIZATION NAME(S) AND ADDRESS(ES)	8. PERFORMING ORGANIZATION REPORT NUMBER
Air Force Institute of Technology, WPAFB OH 45433-6583	AFIT/DS/AA/91-2

9. SPONSORING MONITORING AGENCY NAME(S) AND ADDRESS(ES)	10. SPONSORING MONITORING AGENCY REPORT NUMBER

11. SUPPLEMENTARY NOTES

Approved for public release; distribution unlimited

12a. DISTRIBUTION / AVAILABILITY STATEMENT	12b. DISTRIBUTION CODE

13. ABSTRACT (Maximum 200 words)

Application of Total Variation Diminishing (TVD) schemes to both inviscid and viscous flows is considered. The mathematical and physical basis of TVD schemes is discussed. First and second-order accurate TVD schemes, and a second-order accurate Lax-Wendroff scheme, are used to compute solutions to the Riemann problem in order to investigate the capability of each to resolve shocks, rarefactions, and contact surfaces. Solutions are computed for inviscid supersonic and transonic cascade flow problems. TVD schemes are shown to be superior to the Lax-Wendroff family of schemes for both transient and steady-state computations.

TVD methodology is extended to the solution of viscous flow problems. Solutions are computed to the problems of laminar shock-boundary-layer interaction and unsteady, laminar, shock-induced heat transfer using the new algorithms. Extremely accurate comparison with experiment is arrived at for the shock-boundary-layer interaction case. Accurate comparisons with both theory and experiment is evident for the unsteady, shock-induced heat transfer problem. These solutions are contrasted against solutions computed with the Beam-Warming algorithm, and the TVD solutions are shown to be vastly superior.

14. SUBJECT TERMS	15. NUMBER OF PAGES
Numerical Methods and Procedures, Computational Fluid Dynamics, Inviscid Flow, Viscous Flow, Laminar Flow, Heat Transfer, Unsteady Flow, Steady Flow, Cascades, Supersonic Flow, Transonic Flow, Shock Waves, Shock Tubes, Reynolds Number	166
	16. PRICE CODE

17. SECURITY CLASSIFICATION OF REPORT	18. SECURITY CLASSIFICATION OF THIS PAGE	19. SECURITY CLASSIFICATION OF ABSTRACT	20. LIMITATION OF ABSTRACT
Unclassified	Unclassified	Unclassifed	UL

NSN 7540-01-280-5500